Alma Mater Studiorum - Università di Bologna

DOTTORATO DI RICERCA IN

MECCANICA E SCIENZE AVANZATE DELL'INGEGNERIA

Ciclo 34

Settore Concorsuale: 09/A3 - PROGETTAZIONE INDUSTRIALE, COSTRUZIONI MECCANICHE E METALLURGIA

Settore Scientifico Disciplinare: ING-IND/14 - PROGETTAZIONE MECCANICA E COSTRUZIONE DI MACCHINE

THEORETICAL AND EXPERIMENTAL STUDY OF NOVEL HYBRID COMPOSITE AND METAL-COMPOSITES INTERFACES

Presentata da: Luca Raimondi

Coordinatore Dottorato

Marco Carricato

Supervisore

Andrea Zucchelli

Esame finale anno 2022

ABSTRACT

The growing demand for lightweight solutions in every field of engineering is driving the industry to seek new technological solutions to exploit the full potential of different materials. The combination of dissimilar materials with distinct property ranges embodies a transparent allocation of component functions while allowing an optimal mix of their characteristics. From both technological and design perspectives, the interaction between dissimilar materials can lead to severe defects that compromise a multi-material hybrid component's performance and its structural integrity. This thesis aims to develop methodologies for designing, manufacturing, and monitoring of hybrid metal-composite joints and hybrid composite components. In Chapter 1, a methodology for designing and manufacturing hybrid aluminum/composite co-cured tubes is assessed. In Chapter 2, a full-field methodology for fiber misalignment detection and stiffness prediction for hybrid, long fiber reinforced composite systems is shown and demonstrated. Chapter 3 reports the development of a novel technology for joining short fiber systems and metals in a one-step co-curing process using lattice structures. Chapter 4 is dedicated to a novel analytical framework for the design optimization of two lattice architectures.

La crescente domanda di soluzioni alleggerite in ogni campo dell'ingegneria, sta spingendo l'industria a cercare nuove soluzioni tecnologiche per sfruttare il pieno potenziale dei diversi materiali. La combinazione di materiali diversi con gamme di proprietà specifiche racchiude in sé una trasparente ripartizione delle funzioni fra componenti, consentendo al contempo un connubio ottimale delle loro caratteristiche. Sia dal punto di vista della progettazione che del processo, l'interazione tra materiali differenti può portare a gravi difetti che compromettono le prestazioni di un componente, anche nell'integrità strutturale. Questa tesi mira a sviluppare metodologie per la produzione, la progettazione ed il controllo di componenti ibridi metallo-composito e compositi ibridi. Nel Capitolo 1, viene esposta una metodologia per la progettazione e la produzione di tubi ibridi in alluminio/composito co-curati. Nel Capitolo 2, viene mostrata e dimostrata una metodologia full-field per il rilevamento del disallineamento delle fibre e la

previsione della rigidezza per sistemi fibrorinforzati a fibra lunga. Il capitolo 3 riporta lo sviluppo di una nuova tecnologia per l'unione compositi a fibra corta e metallo in processo di co-curing, utilizzando lattice structures. Il capitolo 4 è dedicato a un nuovo quadro analitico per l'ottimizzazione del design di due tipologie di lattice structure.

SUMMARY

LIST OF FIGURES

INTRODUCTION

The growing demand for lightweight solutions in every field of engineering is driving the industry to seek new technological solutions to exploit the full potential of different materials [1]. Polymer matrix composites (FRPs) are widely appreciated for their high specific strength and young modulus values. Due to their inherent orthotropic behavior, these materials allow for design scaling at the material level. Conversely, although their specific shock-absorbing capacity is generally high, they tend to fail in fragile ways with little or no advance warning. Considering the polymeric nature of the matrix, they are also challenging to use in operating environments where high temperatures are expected. Metals are still being appreciated for their high resistance properties, even in extreme working environments. Thanks to the yielding phenomenon, they are generally able to store a considerable amount of plastic energy before their ultimate failure.

The combination of dissimilar materials with distinct property ranges embodies a clear allocation of component functions while allowing an optimal blend of their characteristics. There are two well established overarching techniques for joining metal and composite structures: (i) adhesive bonding and (ii) mechanical fastening. Several authors already reviewed researches that have been carried out on these two topics over the last 3 decades [2–10]. As a rule of thumb, adhesive bonding offers the most lightweight potential. However, they are often relegated to secondary structures due to their tendency to fail with scarce or no advice.

A distinction is made between traditional adhesive bonding of cured components and the bonding of cured components with wet laminates ("co-bonding" or "co-curing ") [11]. Mechanical fastening is commonplace but requires the composite part to be machined, often causing delamination. Complex stress distribution around the hole is generated in the composite part, and any attempt to mitigate failure deals in the oversizing of the part itself [12]. A promising solution is to hybridize the technologies above to form a hybrid bonding-fastening joint. A hybrid bonding-fastening joint can be obtained employing bolts [13], rivets [13–15], or pins. Although the interlocking mechanism appears to be similar, hybrid joint obtained using bolts and rivets differs

from hybrid joint obtained using pins for size and arrangement of the through-the-thickness reinforcing element. Contrary to hybrid bolted joints – which generally use only 1–3 rows of bolts/rivets – hybrid pinned joints use a substantial number of small-diameter pins. Several technologies were developed over the last decade to manufacture such protrusion over a metallic adherend.

Electron beam [16], a technology developed since 2004 by The Welding Institute (TWI), has been successfully employed to produce the so-called Comeld™ joint [17–19], reported in Figure 0.1.

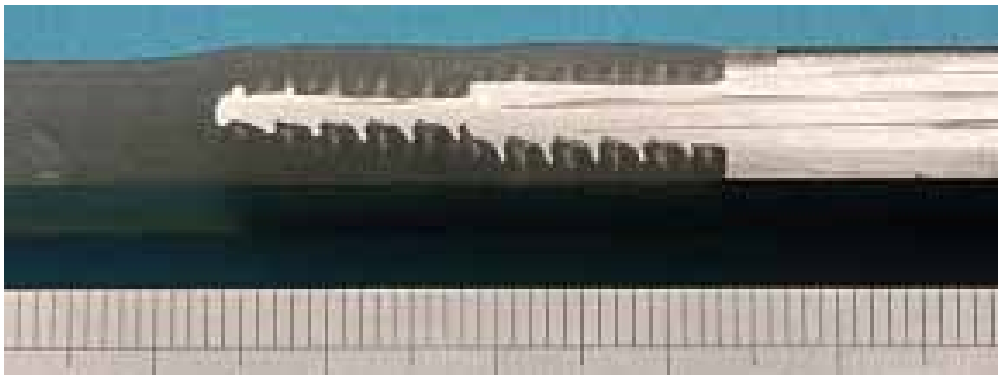

Figure 0.1: Comeld Joint

According to Wang and others [20], several protrusion geometries can be produced by tuning process parameters. The technology is relatively fast (it takes around 10 [s] to form a protrusion with a height of 1.5 mm) and quite versatile (protrusion size ranges from 10 μm to 20 mm). Studies performed to assess an optimal protrusion geometry showed that the angle and height of protrusions are the main parameters affecting the static performance of Comeld™ joints [21,22].

The arc-welding-process, "cold-metal transfer" [23,24] was used to produce pins having a diameter of 0.8 [mm] and a height of 3 [mm] by Ucsnik and others [25] (see Figure 0.2). Only two pin geometries were feasible and the grow rate was limited.

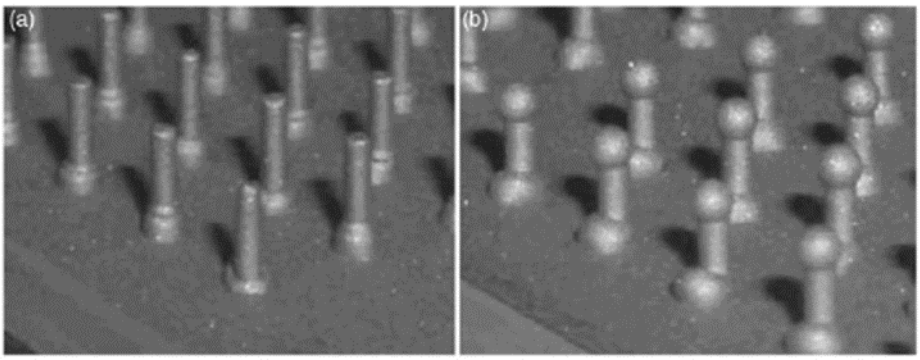

Figure 0.2: Pins produced by cold metal transfer [25]. a) cylindrical pins b) ball-head pins

Capacitor Discharge Stud Welding was used to manufacture pins by Graham [26] as visible in Figure 0.3. Pin dimensions and feasible geometries were comparable to the ones produced through cold-metal transfer.

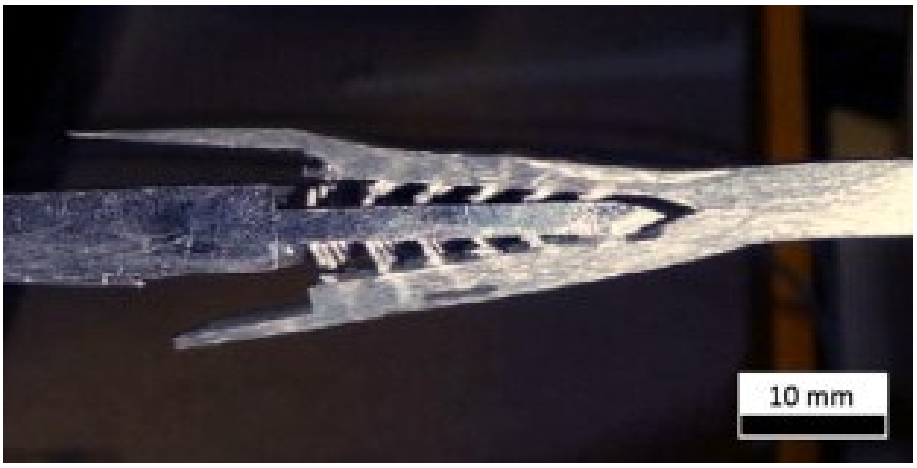

Figure 0.3: Pins obtained using Capacitor Discharge Stud Welding [26]

Sheet Pins are pins that are produced by stamping a specific pattern on a metal sheet and then rotating the reinforcing elements perpendicular to the substrate, up and down [27]. The geometry of the sheet pins is limited to a 2-dimensional complexity and the maximum number of pins is also limited per unit area by the thickness of the adherents. According to Heimbs [28], sheet Pins are much more flexible, cheap, and simple in handling than other 3D reinforcement pins.

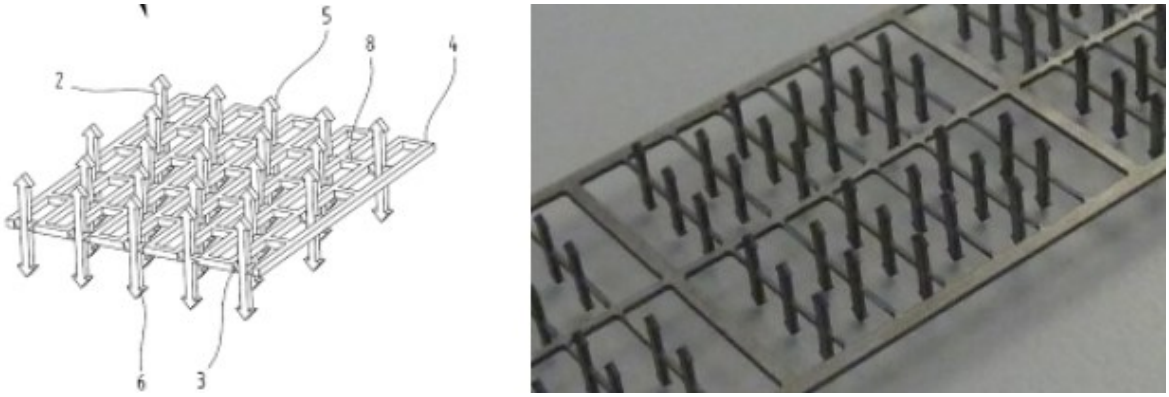

Figure 0.4: Sheet pins [27]

Additive Manufacturing (AM) in the form of laser metal deposition was employed by Parkes [29,30]. Pins produced by AM are called "HYPER" (HYbrid PEnetrative Reinforcement) according to a 2008 Airbus patent [31]. A representation of an array of HYPER pins is reported in Figure 0.5. The main advantage of HYPER technology is that few limits exist in the pin's design, and the intrinsic morphology of the surface obtained by AM seems to promote adhesion at multiple scales [32]. Typical pin size are: diameter of 1 [mm] and a height of 4 [mm] [29,33]; with the impressive growth of AM technologies in recent years, even smaller diameters can be succesfully manufactured.

Figure 0.5: Macro images of the AM built hyper pins [29]

Despite the low TRL level of HYPER joint, investigations to date have shown impressive results over unpinned counterparts and other technologies [34,35]. Investigations also showed feasibility for implementing the conventional ultrasonic NDT method for damage inspection [30,36] and damage evolution prediction by finite element modeling [33,37].

In most of the studies presented above, the metal alloy used in the experimental tests was a titanium alloy. Titanium alloys exhibit a coefficient of thermal expansion (CTE) that is nearly 3 times less than the CTE of an aluminum alloy and about 2 times less concerning the CTE of a stainless steel alloy. Carbon fiber-epoxy composites have an anisotropic CTE that depends on their stacking sequence: carbon fibers have low negative CTE in the axial direction and large positive CTE in the radial direction. Significant fabricational thermal residual stresses may thus be generated during the co-cure joining process due to the difference of CTE between metallic and composite adherends [37–39]. It can be argued that these considerations apply mainly to the bonding surface by virtue of its relatively large spatial extent, and to a secondary extent to the protrusions by virtue of their small size. A technique for reducing defects in co-cured aluminum-carbon fiber axisymmetrical joints is illustrated in Chapter 1. In that case, penetrative reinforcements could not be added due to the inability to access the tube's inner part to grow the protrusions. This highlights a limitation in available hybrid joining technologies when dealing with curved/complex shaped parts.

An inherited limitation observed in all technologies mentioned above is that, due to the penetration of the pins into the wet prepreg, an intense fiber waviness is induced in the composite part. As visible in Figure 0.6 a, obtained by stitching nearly 200 single micrographs together, fiber waviness appears at multiple lengths with a-periodic distributions. The region surrounding the pin (Figure 0.6 b) is “eye-like” as reported in [33].

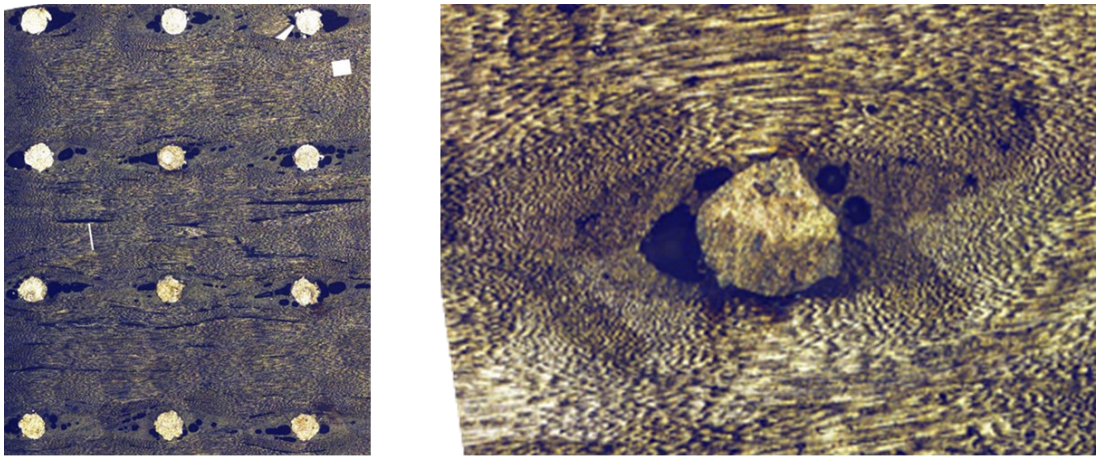

(a) (b)

Figure 0.6: Defects on the composite side in a typical HYPER joint with 0.5 [mm] cylindrical pins. (a) overview on a 3x4 array of pins (b) typical defects surrounding a single pin

Adverse effects of fiber misalignment in composites have been widely studied [38,39] and homogenization techniques were proposed [40]. For instance, it was demonstrated that both decrease in modulus and compressive strength of a laminate can be correlated with the laminate waviness. It can be argued that an optimal design for a penetrative reinforcement should also account for this kind of defect and their spatial extension. In the cited literature, optical microscopy was used by [19,33], but no indications were found on the measuring procedure used in that works. In Chapter 2, a novel non-destructive full field analysis methodology is proposed. The procedure was developed for compression molding, but no limits exist to apply it to detect this kind of defect in hybrid pinned joints.

Penetrative reinforcements are designed to join long-fiber composites systems in conventional autoclave techniques. After extensive research, no study was found in the literature about joining metal and short fiber architectures using penetrative reinforcements. It is worth mentioning that, differently from what happens with endless fiber systems, the final properties of short fibers composite beneficially dependent on the material's flow behavior during compression molding. Uncured short fiber prepreg appears as a randomly oriented conglomerate of unidirectional strands, with inhomogeneous void due to microstructure heterogeneity. Hence the need to develop

a new technique of reinforcement that could be more “infiltrative” than “penetrative”. Indeed, it can be argued that long and thin pins are prone to buckling with relatively small forces; moreover, their poor bending resistance makes this kind of structure totally inadequate to withstand the high load that occurs during a compression molding operation. A novel kind of infiltrative joining technology was developed and illustrated in Chapter 3.

Experimental investigations suggested the need to improve the design of metamaterials to withstand at processing loading conditions. For this purpose, a design framework for optimizing geometric parameters of infiltrative reinforcements to withstand processing loads was developed and illustrated in Chapter 4 and validated through extensive finite element analysis.

Chapter 1. DESIGN AND MANUFACTURE OF HYBRID ALUMINUM/COMPOSITE CO-CURED TUBES WITH VISCOELASTIC INTERFACE LAYER

Marco Povolo[a]*, Luca Raimondia[a,b], Tommaso Maria Brugo[a], Angelo Pagani[c], Dario Comand[c], Luca Pirazzini[c], Andrea Zucchelli[a,b]

[a]*DIN – Università di Bologna, Viale Risorgimento 2, 40136 Bologna, Italia*

[b]*CIRI-MAM – Università di Bologna, Viale Risorgimento 2, 40136 Bologna, Italia*

[c]*REGLASS SRL– Via Caduti di Cefalonia, 4, 40061 Minerbio BO, Italia*

The candidate is one of the investigators of this study. He contributes to the conception and design of the study, data acquisition and analysis, manuscript drafting, revision and approval. The work has been published on Procedia Structural Integrity.

1.1 INTRODUCTION

The increased performances of hybrid pipes and tubular section geometries are desirable in several industry for their higher natural frequencies and bearing stress capability with respect to their metal counterpart. In some industrial applications, the possibility to have a metal coating on the external part of the pipe is desirable for their antistatic properties, improved corrosion resistance and improved tribological properties. Moreover, metal coatings offer the possibility to perform thermal spray treatments for a functionalization of the surface.

Hybrid tubular components has been successfully manufactured in several ways, each one with their specific limitation. Adhesive bonding is commonplace but is applicable only for small components and requires a two-step manufacturing process [41,42]. Interference coupling is usually obtained by heating or cooling the metal part, but the process tends to perform slow in production and requires again two steps cycles.

Co-curing is a novel promising technology that enables the production of a hybrid tube in one step manufacturing process, able to provide cost and time savings. However, despite their

attractive advantages, the manufacturing tasks associated with hybrid metal/composite co-cured tubes are still a challenge in their design process and few and recent studies has been published on the topic.

The manufacturing process of co-cured, hybrid, aluminum-core shaft, was studied by Cho [43] and others. Their investigation showed that the quality of the component is strictly connected with the axial residual thermal stresses due to the large difference of coefficient of thermal expansion (CTE) of the two materials. To reduce the residual thermal stresses, the use of a compressive preload by the employment of a steel jig was suggested.

A similar solution for the design and manufacturing of a co-cured hybrid aluminum drive shaft was suggested by Lee and others[44]. The effects of thermal stresses were again reduced by inducing a compressive preload on metal tube and the stacking sequence was selected by minimizing the failure index according to Tsai Wu criterion. An interface made of glass fiber epoxy composite was introduced to reduce galvanic corrosion between the aluminum and the carbon fiber composite, but authors found a higher failure index.

Han and others [45] found a solution for design and manufacturing of a conical co-cured hybrid pantograph upper arm using a frictional layer to avoid the excessive stress and possible failure in the bonding layers between the composite laminate and aluminum tube. The hybrid structure was designed to reduce the mass and to enhance the structural stiffness. At least, they design a metal-composite hybrid metal arm that exhibit a much higher mechanical performance than a conventional steel arm avoiding material failure. So far, from the state of the art analysis, it is clear that a key aspect in design and manufacturing of hybrid tubes is the reduction of the residual stress peak to avoid premature failure of the component; the adopted strategies to reach this task are based on the variation of the stacking sequence and by changing the materials at the interface between metal and composite.

NOMENCLATURE

D_{iCFRP}	[mm]	internal dimeter of CFRP tube
D_{eCFRP}	[mm]	external diameter of CFRP tube
D_{iAL}	[mm]	internal diameter of aluminum tube
D_{eAL}	[mm]	external diameter of aluminum tube
l	[mm]	length of tube
s_{CFRP}	[mm]	CFRP thickness
s_{AL}	[mm]	aluminum thickness
s_i	[mm]	interface layer thickness
E	[MPa]	elastic modulus
E_L	[MPa]	longitudinal elastic modulus
E_T	[MPa]	transverse elastic modulus
G	[MPa]	shear modulus
G_{LT}	[MPa]	orthotropic shear modulus
ν_{LT}		orthotropic Poisson's ratio
ρ	[Kg/m^3]	density
α	[1/°C]	coefficient of thermal expansion
α_L	[1/°C]	longitudinal coefficient of thermal expansion
α_T	[1/°C]	transverse coefficient of thermal expansion
TS	[MPa]	tensile strength
$\sigma_{L,rupture}$	[MPa]	orthotropic stress limit, traction *l* direction
$\sigma_{T,rupture}$	[MPa]	orthotropic stress limit, traction *t* direction
$\tau_{LT,rupture}$	[MPa]	orthotropic stress limit, shear *lt*

To the best author's knowledge, this is the first study on hybrid co-cured metal composite tube that employs a viscoelastic interface layer and an optimization of the stacking sequence based on numeric algorithm to minimize the possibility of premature failure and maximize the flexural stiffness. Additionally, an experimental procedure for validating FEA result is proposed. Moreover, due to the viscoelastic properties of the interface, jig is no longer required and tubes can be made in one-step manufacturing cycle.

1.2 MATERIALS AND METHODS

The procedure adopted in the present work combines numerical analysis and experimental tests in order to set-up the design procedure of a hybrid tube with a low impact of residual stresses and minimum deflection under constant bending moment. This loading condition and the well-defined geometry are specific for the field of application of industrial printing machines.

1.2.1 Design and materials

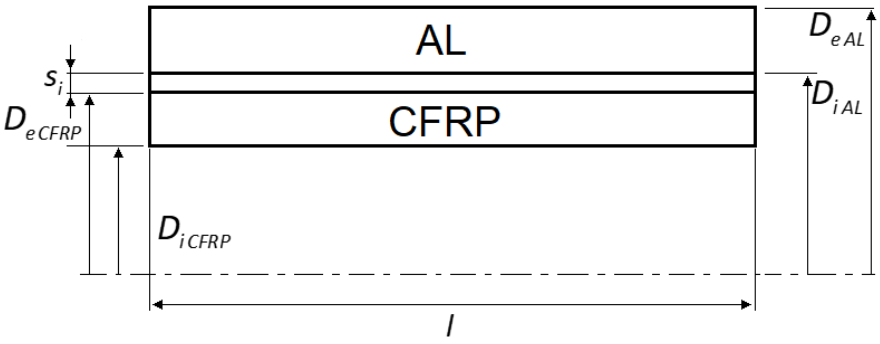

Figure 1.1: Geometric Scheme

The total length of the test tube was 900 mm and the external diameter of the metal tube was 75 mm. The design thickness of the composite was 2.2 mm as a compromise with stiffness and functional requirement. The design thickness of the extruded aluminum tube, made in 6082-T6 alloy, was 2.5 mm. Mechanical properties of UD, Aluminum alloy and elastomeric layer are provided in table 2, 3 and 4 respectively. The stacking sequence initially consisted of 6 layers of unidirectional (UD) CFRP prepreg in the axial direction, which is fundamental for guaranteeing performance and for validating the FEA results. The prepreg named M23350R was supplied by Reglass Srl, Minerbio (BO) Italy. This material is manufactured using Toray T300 and impregnated with a 55% in volume (Vf) of custom epoxy resin EP200, supplied by Reglass Srl. The prepreg was laminated in a clean room at 24 °C and the curing temperature was 110° C.

Table 1.1 Geometric properties of the tube

Properties	D_{iCFRP} (mm)	D_{eCFRP} (mm)	D_{iAL} (mm)	D_{eAL} (mm)	l (mm)	s_{CFRP} (mm)	s_{AL} (mm)	s_i (mm)
Value	64.6	69.0	70.0	75.0	900	2.2	2.5	0.5

Table 1.2 Prepreg properties, M23350R (Reglass Srl)

Properties	E_L (MPa)	E_T (MPa)	G_{LT} (MPa)	ν_{LT}	ρ (Kg/m^3)	α_L (1/°C)	α_T (1/°C)	$\sigma_{L,rupture}$ (MPa)	$\sigma_{T,rupture}$ (MPa)	$\tau_{LT,rupture}$ (MPa)
Value	115100	7700	4400	0.33	1630	-2.7 10^{-7}	4.1 10^{-5}	2200	30	60

Table 1.3 Interface viscoelastic layer (Reglass)

Properties	E* (MPa)	G* (MPa)	ρ (Kg/m^3)	TS (MPa)	$E_{50\%}$ (MPa)
Value	275	92	1250	15.0	12.5

**according to DIN 53504 calculated data (at 1% elongation).*

Table 1.4 Aluminum tube (6082-T6) properties

Properties	E (MPa)	ρ (Kg/m^3)	α (1/°C)
Value	70000	2700	2.4 10^{-5}

1.2.2 Manufacturing process

An innovative process has been implemented to produce hybrid tubes according to the process depicted in Figure 1.2.

1) First, a cylindrical mandrel with silicon body was prepared and cleaned with methylethylketone.
2) Prepreg layers were stacked with a suitable overlap on the surface.
3) A mandrel was inserted into the external metal tube and metal bushings were inserted to maintain the axial symmetry of the component.
4) Pressure of 3 bar was then given to expand the silicon surface of the mandrel and the prepreg and viscoelastic layer were forced to adhere to the inner area of the metal cylinder. In this condition the curing phase of the entire component was able to take place.
5) Once the curing cycle is over, the pressure was raised, and the mold was extracted
6) The component was machined finished.

This manufacturing process uses the low elastic modulus of the interface layer to compensate the deformations due to the different CTE during the cooling phase. This allow to avoid the usage of a jig as suggested by Cho[46] and Lee [47].

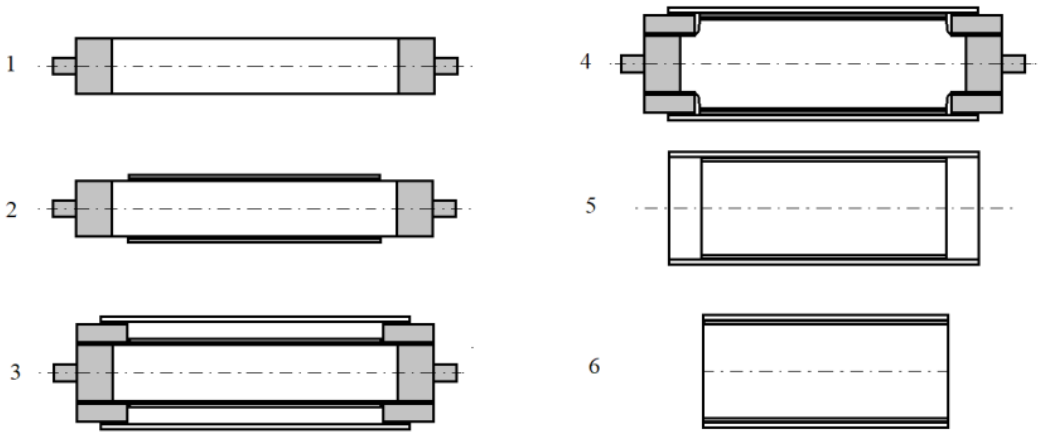

Figure 1.2: Production process

The proposed manufacturing process was successfully used to prepare a first batch of hybrid co-cured tube with the geometrical properties depicted in Table 1.1 and with a stacking sequence of $[0°]_6$ along the axial direction. In Figure 1.3 a micrograph of the so manufactured tube is shown and no delamination phenomena were detected.

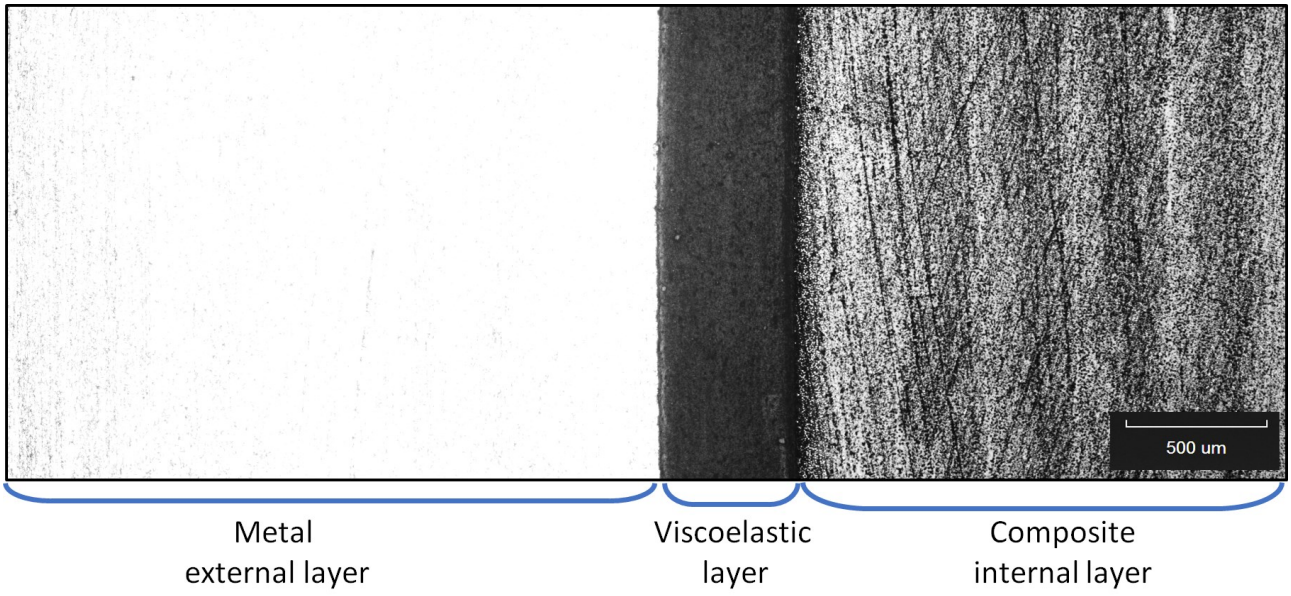

Figure 1.3: Production process scheme

1.3 FINITE ELEMENT MODEL AND EXPERIMENTAL VALIDATION

1.3.1 FEM model and stress analysis

In order to better understand the distribution of the residual stresses at the free edges, finite element analysis (FEA) has been performed. The symmetry of both geometry and loads allowed to study a quarter of cylinder in order to reduce computation time. The FEA model was thermally loaded and the cooling phase was simulated adopting an implicit solver. The tube was modeled in Ansys using SOLID186 elements. SOLID186 is a higher order 3-D 20-node solid element that exhibits quadratic displacement behavior. Reduced integration was used to minimize locking

phenomena without using the layered option. The composite was therefore modeled using a layer by layer configuration in order to better describe the shear phenomena. The viscoelastic layer was modeled selecting a bilinear material behavior (Young's modulus 220 MPa, Yield strength 7 MPa, Tangent Modulus 10 MPa). A mesh convergence test was conducted to minimize the stress error and to respect the zero stress conditions at the free edges. The mesh was refined at free edge and it was found that the maximum element size to correctly represent the stress distributions is 0.01 mm in axial direction.

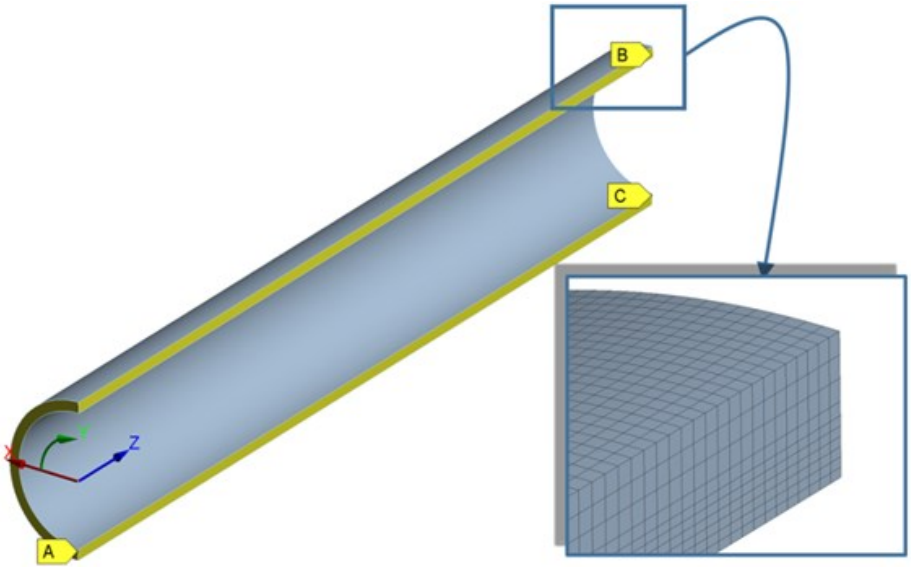

Figure 1.4: Meshed tube and constraints

Contact elements were not introduced to reduce the computational time without reducing precision. The model so build and constrained is represented in Figure 1.4. Face marked with letter A was constrained in axial (z) direction and both faces B and C were constrained in circumferential direction (y).

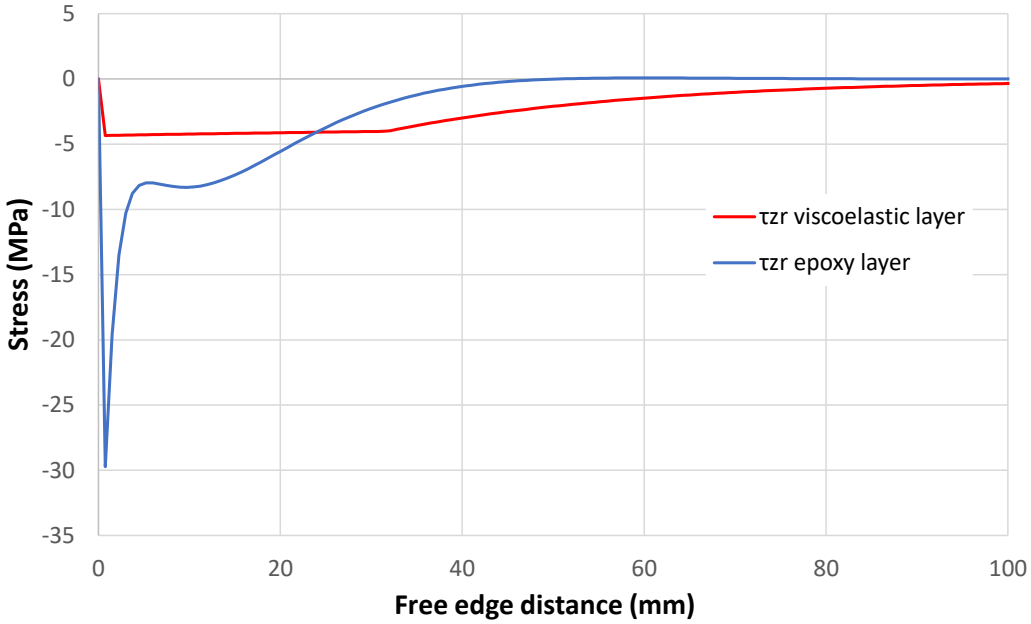

Figure 1.5: FEM Shear stresses comparison in the interface layer at the end node of the tube

Thanks to the model it was possible to investigate the stress and strain distribution along the axial direction. It was found that the most stress is the shear stress τ_rz developed between the aluminum and the composite. A comparison of the shear stress distribution at the centerline of the adhesive interlayer is represented in Figure 1.5, for both epoxy (blue curve) and viscoelastic interlayer (red curve). For the case of the epoxy interlayer, material stress concentration occurs at 0.7 mm c.a from the free edge, with a maximum absolute value of 30 MPa. This value is above the critical shear strength of commonly used epoxy adhesives and therefore makes this solution not doable. On the contrary, for the viscoelastic layer, the curve show a large "plateau" close to the free edge zone, due to the elastoplastic behavior of the material.

1.3.2 Experimental validation

Test tubes was manufactured with all 6 layers at 0° in the axial direction to validate the stress analysis calculated using FEM.

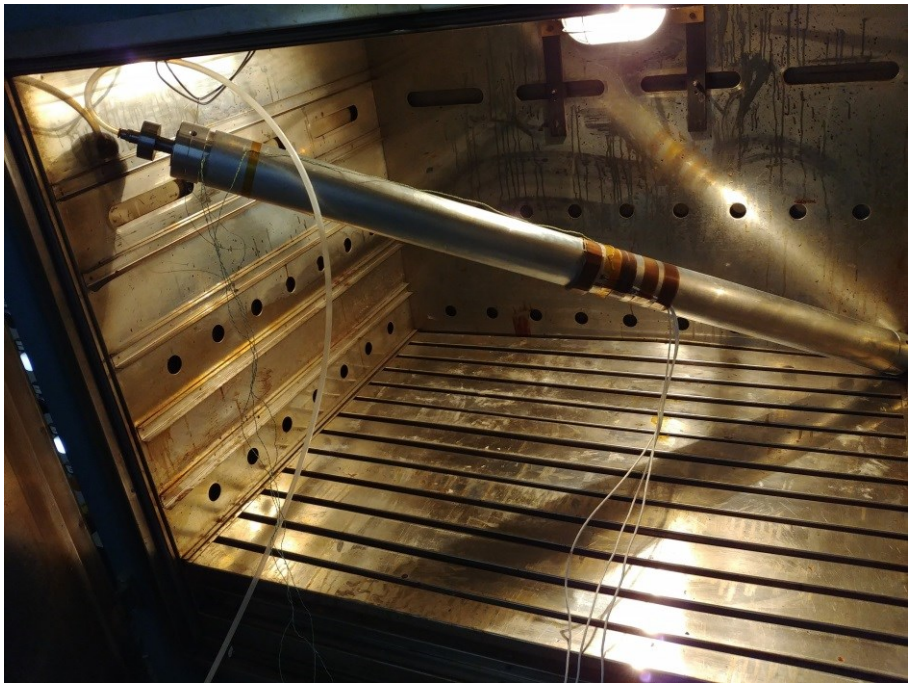

Figure 1.6: Experimental set-up

Subsequently, 2 self-temperature-compensated strain gauges were applied at the center of tube to monitor axial and hoop strain evolution during the whole curing cycle. It was found that the after curing axial and hoop strain differs from the numerical model of less than 7% and 4%, respectively. This small error ensures a good accuracy in the optimization procedure.

1.4 OPTIMIZATION AND RESULTS

In common practice, the optimization process of a composite structure is dominated by one or more objective functions, design variables and constraints [48]. In the present work, a failure index of 0.7 according to Hashin 3D criteria as been assumed as a constrain. Hashin 3D is an interactive failure criteria that enables to detect fiber or matrix failure and is able to describe as well the interlaminar one [49]. The minimization of the deflection under pure bending load has been set as objective function. The stacking sequence angles of the 6 layers that composes the laminate were set as a continuous variable. The optimization was performed using the "surrogate model" proposed in the Design Of Experiment (DOE) module of Ansys, in order to evaluate the influence of the variables on the responses and reducing the global computational time. After the DOE was performed, the tube has been optimized by a Multi-Objective Genetic Algorithm

(MOGA). The best solution obtained with MOGA foresees a predominance of layers at almost zero degrees, with the exception of the first two in contact with the viscoelastic layer (Table 1.5). This solution provided a failure index of 0.68, but manufacturability limits imposes to use discrete angles for the prepreg wrapping sequence. For this reason, a new simulation with manufacturable layers angles (Table 1.5) was carried out and the result were compared. An acceptable 3% increase of the deflection was obtained with a failure index of 0.63.

Table 1.5 Stacking sequence comparison

Layer number	Optimization angle value (°)	Equivalent manufacturing angle value (°)
1	-19.8	-30
2	+42.6	+30
3	-5.4	0
4	-0.9	0
5	-3.7	0
6	-9.2	0

1.5 CONCLUSION

In this study a manufacturing process, an experimental validation and an optimization of the stacking sequence for hybrid co-cured aluminum/composite tube with interface layer under constant bending moment is proposed. In particular, for the first time a one-step, cost effective, manufacturing process of an hybrid metal-composite tube is proposed.

The process was successfully implemented and used to realize a first batch of hybrid-metal composite tubes. Micrograph analysis reveal no defect in the composite and perfect bonding between the viscoelastic layer and both metal and composites layers, thus demonstrating the effectiveness of the new process. Moreover the results of the experimental analysis together with the numerical simulations of the hybrid tubes, gave the conclusion that:

- the numerical model well represented the real behavior of the hybrid tube;
- the viscoelastic interface layer between aluminum and CFRP tube, compared to the configuration with an epoxy interface layer, is effective to reduce thermal residual stress peaks thus providing a suitable failure index for the entire part.

Thanks to the preliminary setup of the numerical model it was possible to establish a robust procedure for the optimization of the composite stacking sequence. Manufacturability was ensured by perform a further simulation with discrete ply angles close to the optimal solution.

In this work, only laminate with a constant thickness and composite tube with defined number of layers and defined geometry was analyzed. In the future, different type of stacking sequence and geometry constraints will also be investigated.

Chapter 2. FIBER MISALIGNMENT ANALYSIS IN PCM-UD COMPOSITE MATERIALS BY FULL FIELD NODAL METHOD

Luca Raimondi[a *], Tommaso Maria Brugo[a,b], Andrea Zucchelli[a,b*]

[a]*DIN – Università di Bologna, Viale Risorgimento 2, 40136 Bologna, Italia*

[b]*CIRI-MAM – Università di Bologna, Viale Risorgimento 2, 40136 Bologna, Italia*

The candidate is the main investigator of this study. He contributes to the conception and design of the study, design and implementation of the code, experimental testing, data acquisition and analysis, manuscript drafting, revision and approval. The work has been published on Composites part C: open access/Composites Structures.

2.1 INTRODUCTION

Recent advances in polymers and novel out-of-autoclave techniques have enabled composite materials to be at the forefront of lightweight technologies in the automotive and transportation industries [50]. Long fiber carbon prepregs have been traditionally formulated for autoclave processing, but continuous improvement in fast-curing resins has recently extended their processability to compression molding, enabling this technology suitable for high volume part production [51]. Despite its attractive benefits, prepreg compression molding (PCM) can produce more significant fiber misalignment to the autoclave process, especially when continuous fibers are co-molded with discontinuous fibers [52,53].

It is worth mentioning that prepreg is subjected to an intense flow during PCM processing favored by the system's high heat efficiency, the limited heat capacity of small thickness prepreg charge, and the tools' high compressing speed. Rheological studies in long discontinuous fibers composites [54–56] have demonstrated that the effective viscosity tensor is highly anisotropic with maximum elongational viscosity in the fiber direction. Sommer [57] reports that compression molding with long fiber composites is aptly described by a plug flow with highly anisotropic in-plane behavior. According to the cited literature, it can be argued that fiber

waviness in a PCM process is caused by fiber transport and interaction phenomena correlated to the flow characteristics in the mold.

The negative effect of fiber misalignment on composites under compressive loading has been widely studied [38,39], and homogenization techniques have been proposed [40]. The issues related to the previously cited literature highlight the need to identify practical tools that have to quantify fiber misalignment in composite materials as a result of the process to predict the mechanical properties of the components.

Several techniques have been developed to measure and detect fiber distortion, mostly based on 2D micrography. Yurgartis [58] proposed a method based on the measurement of the fibers' ellipticity in a cross-section of the component. By measuring the major and minor axes of the ellipsoids and knowing the fiber diameter, the 3D spatial orientation of the fibers can be estimated. This method, however, is destructive and it is not able to identify the sign (positive or negative) of the deviation of the fibers and is more limited by the fact that the cross-section of the fibers is not always perfectly circular.

Kratmann and others [59] and, more recently, Wilhelmsson and Asp [60] settled methodologies in which surfaces parallel to fiber direction were sand gridded and evaluated by image algorithm on a 2D micrograph. The methods have been proven to be robust and economical, however require sample preparation that irreversibly damages the surface of the composite.

Recently, some Non-destructive testing (NDT) methodologies were proposed to detect fiber misalignment using Micro Computed Tomography (micro-CT) [61] or eddy current [62]. However, these techniques are challenging to be implemented in a mass production line to perform a real-time quality inspection.

From the state of the art analysis, it is clear that most current methods for determining the fiber orientations in a composite part require expensive equipment, are difficult to perform on full-sized parts, or result in the part being destroyed.

This work aims to settle a fast and cost-effective methodology for estimating in-plane fiber misalignment in molded composite components by analyzing the displacement field that occurs on a discrete number of points on the surface of the part during the manufacturing process.

The precision of the proposed method, namely Full Field Nodal Method (FFNM), is successfully benchmarked with one of the most recent methodologies available in the state of the art, and potential advantages of implementation in FEA analysis for stiffness prediction is demonstrated. The proposed NDT, being a fast, full field optical technique, can be easily implemented in real time process monitoring either for stiffness and strength prediction of UD PCM components, either for assessing process parameters to reduce fiber misalignment defects.

2.2 MATERIALS AND METHODS

Materials and plate manufacturing are described in Section 2.2.1, the step-by-step description of the FFNM procedure is explained in Section 2.2.2 and experimental validation methods are illustrated in Section 2.2.6.

2.2.1 Materials and plates manufacturing

Prepreg used in the study was a UD P 384_S supplied by Torayca, Tokyo, Japan. This material is manufactured with T700S high strength carbon fibers and impregnated with 40% (V_f) #2300 resin, both manufactured by Toray Industries. This prepreg's initial misalignment angle was measured to be 0.88°, as reported in Supplementary Data, Section 2.5.2. A total of 3 plates (1 for optical microscopy analysis and 2 for both mechanical testing and optical microscopy analysis) were manufactured by stacking 3 plies of UD P 384_S4 in the $[0°]_3$ configuration. The pre-assembled plies were grided according to the procedure described in next section 2.2 and compression-molded. To ensure demoldability, the release agent employed was a Chemlease® PMR EZ supplied by Chem-Trend L.P. Howell, Michigan United States.

2.2.2 Step-by-step description of the proposed methodology

The proposed method can be described in 3 main steps: preparation of the surface and subsequent compression molding (section 2.2.3), digitalization, image processing and corners detection (section 2.2.4), deformation analysis and fiber misalignment detection (section 2.2.5).

2.2.3 Step 1: Surface sampling points preparation and compression molding

In the present work, sampling points were generated as corners of a uniform, equally spaced, 35 mm grid. In particular, the grid has been drawn in two perpendicular directions directly on the wet prepreg by using a 3 mm wide Berner paint marker, with a similar approach to the one described in [3]. Before the curing phase, samples were scanned into a Kyocera TASKalfa 3501i Multifunction Laser Printer with a resolution of 600x600 dpi. After that, the 3 gridded prepreg plates were compression molded into a 320x320 mm tool designed to produce arbitrary thickness plates and installed in a downstroke AEM3 press. The temperature of the tool was set at 140 °C and monitored by 2 thermocouples. The tool was spray-coated with the release agent, the charge was 98% tool coverage, and plates were manufactured using a 15 minutes cycle at 56.4 bar pressure. After curing, samples were extracted, cooled in free air up to room temperature, and scanned with the previously mentioned equipment at the same resolution of 600x600 dpi.

2.2.4 Step 2: Image processing and corners location detection

Scanned images were processed using custom software written in Matlab R2019a. The script performs a series of image manipulation and cleaning techniques to remove the noise and detect each corner's coordinate location. The step-by-step procedure is reported in Supplementary Data, Section 2.5.1.

2.2.5 Step 3: Deformation analysis & Fiber Misalignment detection

The displacement of sample points of the grid, identified as the difference $\overline{\boldsymbol{u}}$ of their position prior and after compression molding by the procedure described in section 2.2.4, were considered as nodal displacements of a set of 4 nodes interconnected iso-parametric elements. For each element, according to the formulation described in [63,64], both components of the displacement field and

position were approximated using interpolating "shape" functions N_i, so that $\boldsymbol{u} = \sum_{i=1}^{4} N_i u_i$,$\boldsymbol{v} = \sum_{i=1}^{4} N_i v_i$ and $\boldsymbol{x} = \sum_{i=1}^{4} N_i x_i$, $\boldsymbol{y} = \sum_{i=1}^{4} N_i y_i$, being u_i and v_i the displacement component in x and y directions of element nodes, $\boldsymbol{u}$,$\boldsymbol{v}$, and $\boldsymbol{x}$, $\boldsymbol{y}$ respectively, the components of the displacement field $\boldsymbol{U}$ and the components of the position vector $\boldsymbol{X}$ in the image reference system for each element of the grid as shown in Figure 2.1 a and Figure 2.1 b. This approach [65] allows calculating the in-plane components of the element deformation by its gradient $\boldsymbol{F}_{el}$, as a function of nodal displacement $\overline{\boldsymbol{u}}$ and shape functions by the relationship

$$\boldsymbol{F}_{el} = \boldsymbol{I} + \sum_{j=1}^{n} \overline{\boldsymbol{u}}^{j} \otimes \frac{\partial N^{j}}{\partial \boldsymbol{X}} \quad (1)$$

where $\boldsymbol{I}$ is the identity matrix. Both deformation and rigid body rotation are combined in the operator mentioned above: separation of the two has been conducted by considering the transformation

$\boldsymbol{F}_{el} = \frac{1}{2}\left(\boldsymbol{F}_{el} + \boldsymbol{F}_{el}{}^{T}\right) + \frac{1}{2}\left(\boldsymbol{F}_{el} - \boldsymbol{F}_{el}{}^{T}\right) = \boldsymbol{\varepsilon_{el}} + \boldsymbol{\omega_{el}}$, in which $\boldsymbol{\varepsilon_{el}}$ accounts to pure deformation and $\boldsymbol{\omega_{el}}$ accounts to the rigid body rotation, according to the classical theory of elasticity results. Since the mathematical formulation of the element is based on C_0 continuity shape functions, nodal components $\boldsymbol{\varepsilon}_k$ of a common node k connecting two or more elements may differ: nodal averaging of deformations by direct averaging their values at nodes has been introduced as an approximation. Calculation of approximate in-plane deformation inside each element was therefore performed by interpolating the averaged nodal values using the shape functions N_j as shown in Figure 2.1 c, Figure 2.1 d, and Figure 2.1 e. The final loop in the FFNM method computes the approximate fiber deviation angle as the arctangent of the averaged "shear" strain as shown in Figure 2.1 f: $\boldsymbol{\theta}$ = ArcTan(2 $\boldsymbol{\varepsilon}_{xy}$).

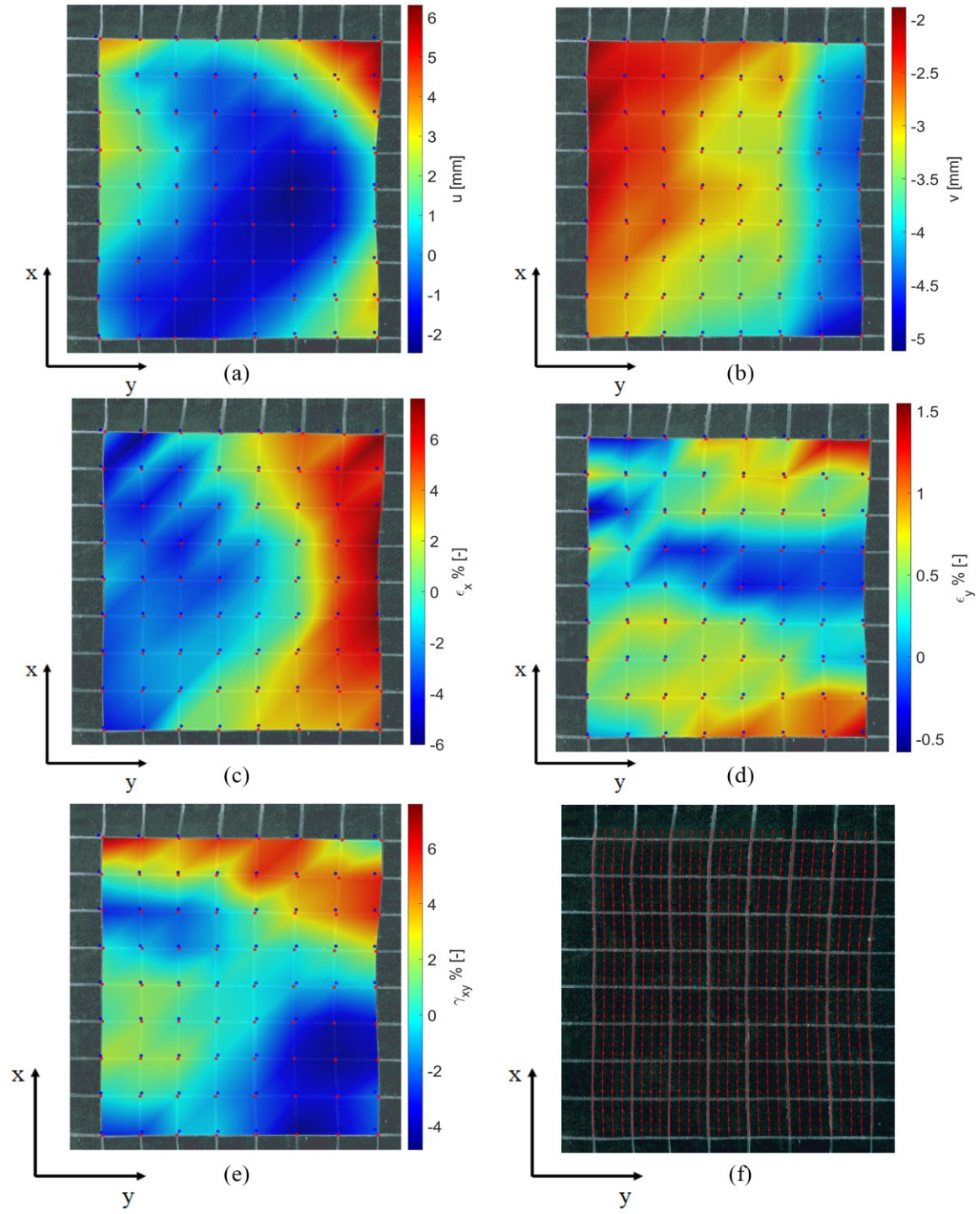

Figure 2.1: Typical UD PCM plate analyzed with FFNM method utilizing 4 node element formulation. Blue Makers: corner location before compression molding. Red Markers: corner location after compression molding. a) u component of displacement. b) v component of displacement c) ε_x component of strain d) ε_y component of strain e) ε_{xy} component of strain f) Computed fiber orientation

2.2.6 Numerical and experimental methods for validation

The methodology was validated by micrograph analysis (section 2.2.7) and mechanical testing (section 2.2.8) techniques and a FEM model was built to exploit the potential of stiffness prediction (section 2.2.9)

2.2.7 Optical Microscopy 2.3.1

The investigation of the method's capability and accuracy to detect local fiber orientation was done by extracting several CFRP specimens from each of the 3 manufactured plates, to allow capturing micrographs in at least 9 node locations on each plate and in at least 36 locations within each analyzed grid element.

Wet ground with 400, 800, and 2500 grit SiC paper along fiber direction, as suggested by [59], was used to condition the specimens initially. Final polishing steps were performed using water-based alumina suspensions with progressively decreasing particle size. Particle size ranges were 3÷1 μm in the first step, 0.5÷0.3 μm in the further one. A low-napped silk polishing pad was used for the alumina 3÷1 μm, while high-napped silk polishing for alumina 0.5÷0.3 μm. Samples were cleaned using an ultrasonic water bath after each polishing step and thus checked on an optical microscope to eliminate scratches induced by the previous step.

Trials with dummy samples were conducted to optimize force, the platen's speed, and time to avoid fiber pullout and artifacts. Samples were studied using a Zeiss Axio Observer 3 at a magnification of 50x and acquired by an Infinity Lite B camera with a resolution of 1.5 megapixel, which results in a resolution of 2.5 μm/pixel.

Micrographs were analyzed by the high-resolution misalignment analysis (HMRA) method [60] for its ability to be relatively insensitive to micrographic surface quality, by selecting a cell size of 80 μm for retrieving a stable standard deviation and by adopting a threshold for binarization of 0.45.

Other useful parameters were: fiber diameter set to 7 μm (as measured on prepreg), minimum fiber diameter set to 3 μm, and minimum aspect ratio set to 6. The HMRA method measures fiber

misalignment angles using a direct Matlab procedure, in which individual fibers are traced one at a time and measured on individual micrographs.

Typical results for the adopted procedure are shown in Figure 2.2, in which very few cells exhibit an overestimation of fiber deviation, as highlighted in Figure 2.2 c. In these regions, individual fiber directions are not appropriately distinguished by the algorithm, contributing to an overall increase of the standard deviation.

The spurious abnormous measurements, always located at the normal distribution tails, were mitigated by using the percentile filtering technique suggested by Wilhelmsson [66]. Detailed inspection on acquired micrographs suggested adopting 95:th percentile as a compromise between filtering of high spurious angles induced by the HMRA method and low filtering of real fiber waviness for the composite system studied herein.

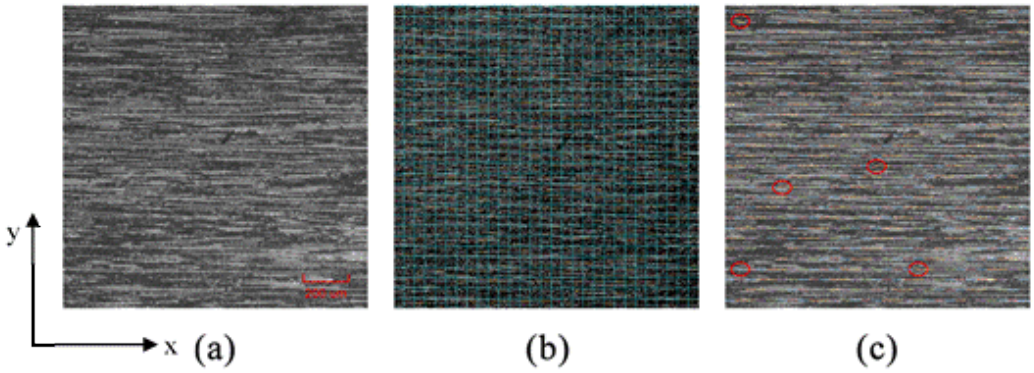

Figure 2.2: Micrograph of a PCM UD sample prepared with the suggested procedure extracted from the top. a) original micrograph at 5x magnification. b) 80 µm cell decomposition c) post-processed micrograph by HMRA method with red circles highlighting cells with high deviation (spurious results)

2.2.8 Mechanical testing 2.3.2

Three tensile specimens were cut from each plate using a high-speed rotating diamond saw tool and checked for imperfections. Justification for the reduced number of ply was the maximization of the specimen's frontal area (25 mm x 320 mm) while maintaining ultimate tensile force within

compatible values for tabs and fixtures. A stochastic speckle pattern was applied on the front face using water-based paint: care was taken in optimizing the size and distribution of the pattern to ensure images were able to collect the wider possible region of each sample for the entire duration of the test.

Tensile tests were carried out under displacement-controlled conditions at a constant cross-head rate of 2.5 mm/min into a servo-hydraulic INSTRON 8033 universal testing machine equipped with a 25 kN load cell. Specimens were monitored during tests at the frequency of 1 Hz by the two cameras of a 3D DIC system (Q-400, Dantec Dynamics, Skovlunde, Denmark), equipped with 17-mm lenses (Xenoplan, Schneider-Kreuznach, Bad Kreuznach, Germany).

Istra-4D software (Dantec Dynamics) was employed to elaborate images and calculate displacements and strain distributions. Facet size and facet overlap were set to 25 pixels and 9 pixels, respectively, and a local regression displacement smoothing filter of 25 x 25 facets, available within Dantec software, was applied as a compromise between accuracy and spatial resolution according to [67]. Results were stored and exported to Matlab for further processing.

2.2.9 FEA Model 2.3.3

An additional analysis of the FFNM capability in predicting mechanical properties due to fiber misalignment was performed by modeling tensile specimens in Ansys APDL using solid elements (SOLID186).

Element size was set to 0.8 mm as shown in Figure 2.3-a, fiber misalignment angle was mapped and applied elementwise by rotating element coordinates systems as suggested by Wilhelmsson and others [68] and shown in Figure 2.3 c.

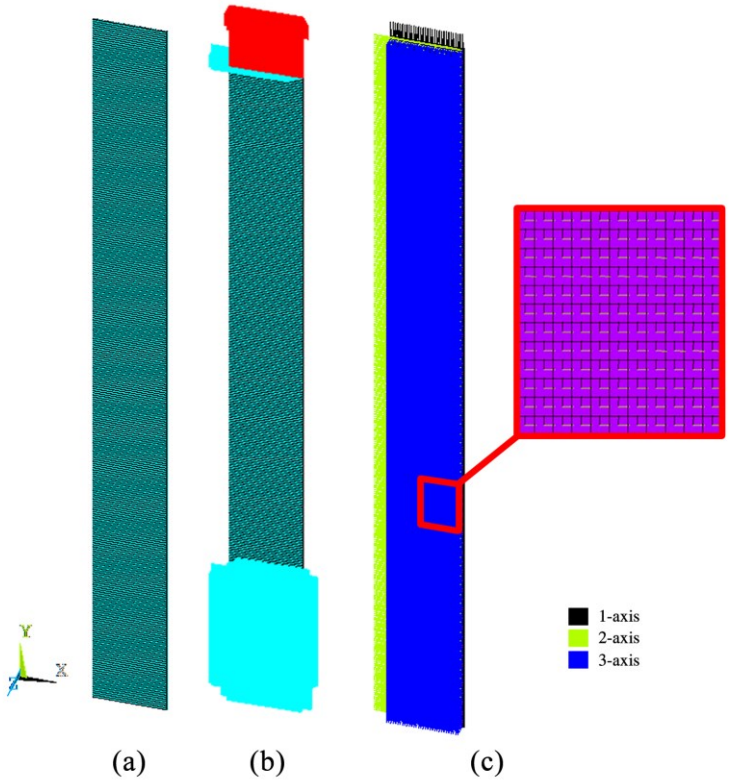

Figure 2.3: FEA Model. a) mesh b) boundary conditions and forces c) coordinate element system

Boundary forces and prescribed displacements were applied as nodal components on the corresponding surface of the mesh: bottom boundary was fixed in all degrees of freedom, the top boundary was fixed in the horizontal X direction of the model as shown in Figure 2.3 b, and forces were introduced by dividing their values by node. Material data were self-measured according to applicable ASTM standards from autoclave processed plates and reported in Table 2.1.

Table 2.1 Prepreg properties, P 384_S

Properties	E_1 (GPa)	E_2 (GPa)	G_{12} (GPa)	v_{12}
Value	115±1	8.6±0.46	4.4±0.28	0.27±0.016

2.3 RESULTS AND DISCUSSION

The misalignment angle measured over the 3 plates by the FFNM method is reported in Figure 2.1. Regions from which tensile specimen were extracted is marked in black dashed line in both Figure 2.4 a and Figure 2.4 c.

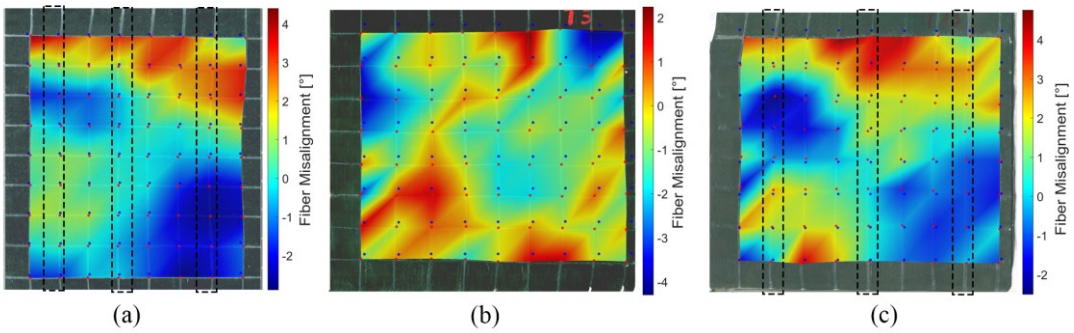

Figure 2.4: Fiber misalignment detected on the 3 sample plates by FFNM method. Tensile specimen locations on molded plaques evidenced in black dashed line on a) and c)

The accuracy of the method is experimentally benchmarked with the HMRA method and discussed in section 3.1. Comparison of mechanical tests and FEA results are presented and discussed in Section 3.2.

2.3.1 Optical Microscopy

The global accuracy of the FFNM method in detecting fiber misalignment is strictly related to its ability to correctly identify fiber misalignment at nodes, where the error on the displacement field is expected to approach a minimum.

All plates in Figure 2.4 show comparable misalignment angles in the range [-2°, 4°], with a sign that depends on the preferred direction of deformation of the grid. Plaques in Figure 4 a and Figure 2.4 c show a moderate variation of misalignment between neighboring nodes for most of their extension whilst the plate of Figure 2.4 b shows a more randomized misalignment in both nodes and elements.

This peculiarity led to the decision to use the plaque of Figure 2.4 b for a more extensive comparison with the HMRA method and to perform random checks on the nodes of the remaining slabs once the tensile specimens had been extracted.

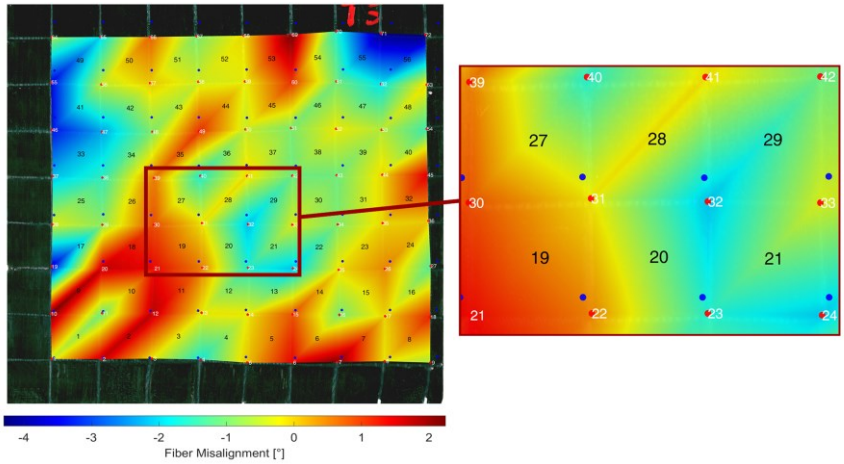

Figure 2.5: Misalignment angle by the FFNM method and result in the representative inner region of the plate

To validate the approximations, discussed in section 2.2.7, of strain averaging at nodes and interpolating averaged nodal values through polynomial shape functions, the investigation on the plaque of Figure 2.4 b was performed within the representative inner region shown in Figure 2.5.

Figure 2.6 compares the results of both FFNM and HMRA methods. The average difference of the mean angle detected by the two methods was as small as 0.175°. Comparable results were obtained for samples extracted by the plates of Figure 2.4 a and Figure 2.4 c. The HMRA method results reveal high standard deviation values, with a maximum value of 1.28°.

The primary justification for these results can be related to the combination of (i) the contribution of the initial waviness of the prepreg, (ii) spurious measurements provided by the HMRA algorithm while processing micrographs with a high content of fibers, and (iii) additional misalignment caused by the friction between prepreg and the halves of the mold during processing.

It is worth mentioning that the overall fiber deviation field reported in Figure 2.1 f is not symmetric about the vertical axis of symmetry due to the high percentage of charge adopted in this study. Indeed, by analyzing the displacement field (Figure 2.1 a, Figure 2.1 b), the flow appears to be highly anisotropic with a limited extension along the direction of the fibers.

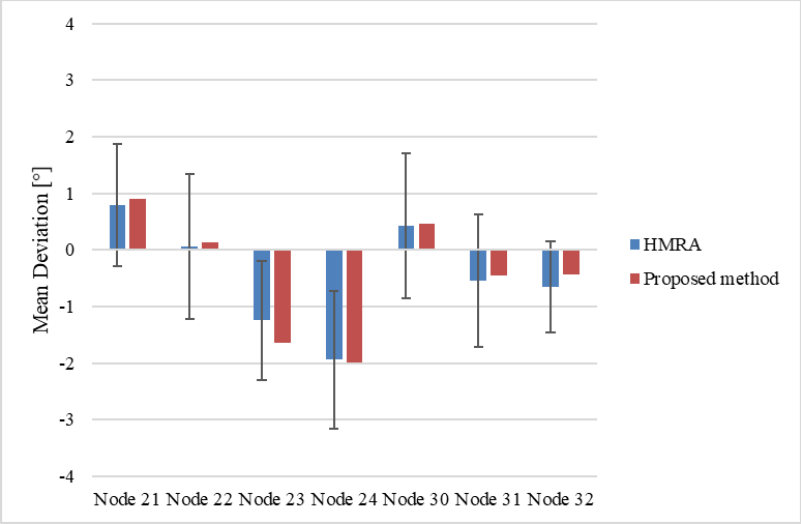

Figure 2.6: Mean fiber orientation at different nodes evaluated by HMRA and present method using bilinear element formulation

This evidence highlight some potential limitation for the proposed methodology. Being the FFNM a surface technique, its precision in addressing fiber misalignment in internal plies is dependent on both flow characteristics through the thickness of the laminate during processing and its stacking sequence.

It can be argued that for laminates in which all plies are stacked with the same orientation and whenever the flow profile is constant through the thickness, measures of misalignment on external plies should be representative of the misalignment of the whole laminate. For stacking sequences having different orientations, measures from FFNM are strictly valid only on the surface of the component.

This could be particularly useful for assessing flexural properties of PCM parts, where UD reinforcements are used in external plies to maximize bending stiffness and strength [69]. Interpolated results of comparing both FFNM and HMRA methods in a region about element 28

of Figure 2.5 are presented in Figure 2.7 to test the ability of shape function to represent the misalignment angle variation over an area correctly.

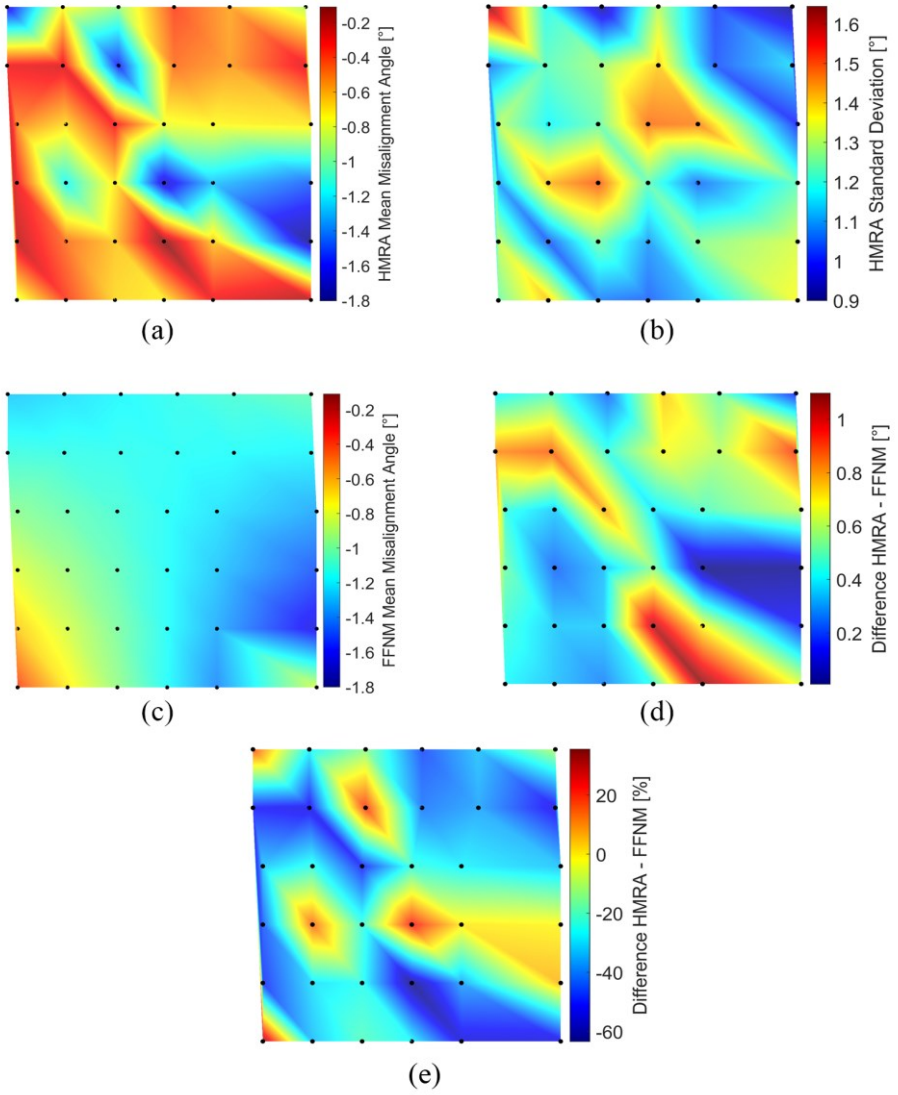

Figure 2.7: Interpolated results of mean misalignment angle evaluated over a region. a)mean misalignment by HMRA method b) HMRA standard deviation c) misalignment angle by FFNM d) absolute difference between HMRA and FFNM.e) relative difference between HMRA and FFNM

Experimental measures of the mean misaligned angle over 36 sample micrographs, detected by the HMRA method and shown in Figure 2.7 a, exhibit a non-linear angle variation distribution,

characterized as a random succession of local peaks and valleys. HMRA Standard deviation, depicted in Figure 2.7 b, exhibits high values again compared to the mean misalignment measured angle. Interpolated results at sample points for the FFNM method are presented in Figure 2.7 c in which angle variation appears to be bilinear as a consequence of the shape function formulation.

Figure 2.7 d shows the difference in measured angle by the two methods, where the highest values were is approached at one border. In this region, the lines of the grid drawn on the plate tend to become more curved, and linear interpolation can no longer adequately describe the displacement field of the plate's surface.

From a detailed analysis of Figure 2.7 d, in addition to the mentioned approximation error, the presence of random noise contained in a few tenths of a degree is observable. It can be argued that this effect may be caused partially by the local initial waviness of the prepreg which cannot be accounted for by the proposed method, whose scope is the evaluation of misalignment caused by processing.

For these reasons, a higher mean average difference of 0.5° was observed within the element, with a maximum of 1.1° in one micrograph over the bottom border of element 28. The relative difference between the two methods, calculated by the formula [70]

$$Relative\ Difference(\%) = 100 * \frac{\theta_{FFNM} - \theta_{statistical,HRMA}}{\min\left(\theta_{FFNM}, \theta_{statistical,HRMA}\right)} \quad (2)$$

is shown in Figure 2.7 e. Note that the highest relative difference values were obtained for extremely small angles measured by HMRA (Figure 2.7 a). This trend in relative difference could be partially explained by the limitations of interpolating by bilinear shape functions used in the proposed method, partially by the dependence of extracted fiber angle and pixel resolution by HRMA for very small misalignment angle [14], and partially on how the relative difference is calculated.

2.3.2 Mechanical test and FEA results

Comparison of tensile tests and FEA result of 3 representative samples are shown in Figure 2.8, in which displacement was measured by the DIC system as the relative displacement of two gauge points positioned at the extrema of each sample.

Experimental curves show several drops due to cracking of the laminate: progressive damage of each sample due to fiber misalignment was demonstrated by slope variation of force-displacement curves after each cracking.

It is worth mentioning that depending on the position where specimens were cut from each plate, the tensile tests revealed different stiffness values. In particular, a maximum stiffness reduction of 4% concerning an aligned UD sample's stiffness was observed. Stiffness's values resulting from FEA, which included fiber orientation derived from the FFNM method, and calculated as the ratio k between applied loads and displacements at boundary nodes of the model, revealed a 1 % average mismatch to the experimental result.

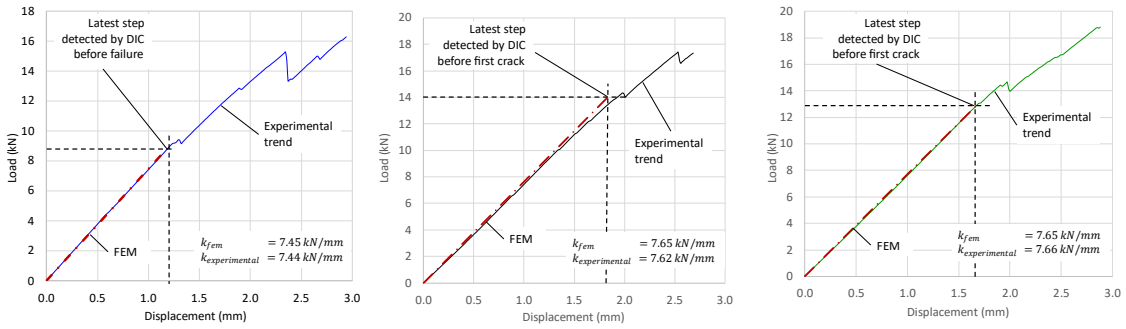

Figure 2.8: Comparison of load versus displacement curves of the 3 different samples

These considerations support the FFNM method's effectiveness when used in combination with FEA to predict small local stiffness variations in the case of PCM composite components with misaligned long fibers.

Comparison between FEA strain results and DIC results are presented in Figure 2.9. Results were evaluated at different applied loads and at the DIC system's latest steps within the linear region of each sample.

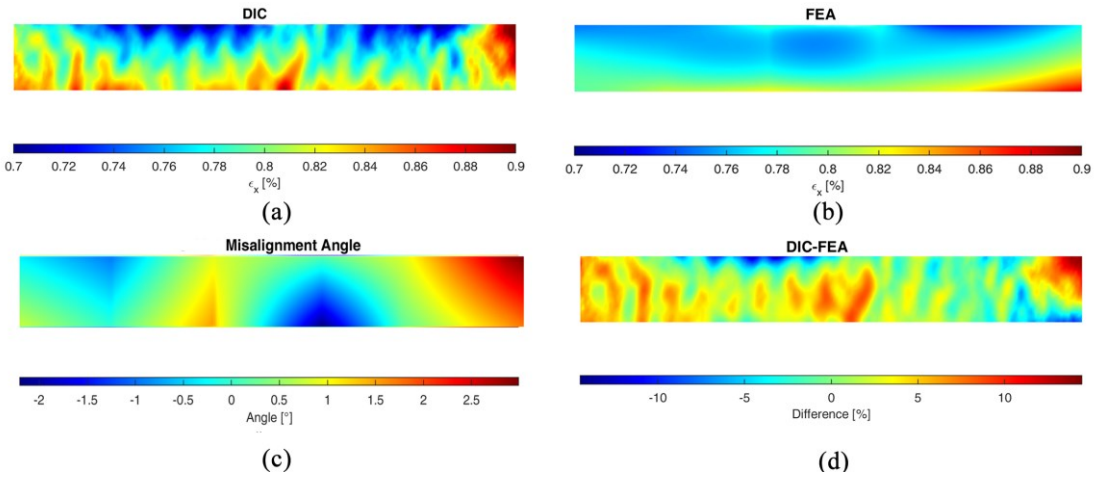

Figure 2.9: Comparison between FEA analysis and DIC results on a typical sample. a) measured strain distribution by DIC system b) computed strain distribution by FE model c) contour p d) Difference between measured and computed strains

First macroscopic failure on specimens occurred in those locations where the maximum absolute value of fiber deviation was detected. Indeed, these regions acted as a triggering point for through-thickness cracks that happened in the fiber-resin interface and the resin.

As shown in Figure 2.9-a, DIC results exhibit a non-uniform strain distribution on the surface, as a superimposition of local cracking of the laminate surface or noise [71] and effects due to misaligned fibers.

Interestingly, strain distribution tends to become more uniform in the centerline of the specimen. A possible explanation is that due to in-plane bending introduced by fiber waviness, more considerable variations were mostly concentrated at borders, where matrix-dominated phenomena are more marked due to abrupt cut of fibers on edges. This phenomenon is partially confirmed by the FFNM method's measurement and shown in Figure 2.9 c: maximum values of strain measured by DIC were mainly located in regions where maximum misalignment was measured.

Results from FEA, depicted in Figure 2.9 b, predicted a more uniform strain distribution over the sample's surface. However, the difference between DIC and FEA results, shown in Figure 8 d and evaluated as [(DIC strain) – (FEM strain)]/(DIC strain)x100, approaches a maximum mismatch value of about 15%. Maximum absolute difference was mainly located at the edges of each

specimen, meaning that the linear FEM analysis was able to describe only an averaged representation of fiber misalignment induced effects.

2.4 CONCLUSIONS

A new, cost-effective and reliable methodology for fiber misalignment detection on PCM composites is presented in this work. A filtering algorithm has been developed to remove process-induced noise on images, thus extending the method's range of application. The approximate displacement field which occurred during compression molding was evaluated by interpolating the displacement of a set of sample points through polynomial interpolating functions. The fiber misalignment angle was successfully retrieved and benchmarked with one of the most recent and reliable methodologies available in the art state. Comparable results with even reduced standard deviation were obtained, proving the precision of the present method in measuring averaged fiber deviation in thin structures. The mechanical test has been performed on PCM samples, and for each sample, a FE model was developed by rotating elemental coordinate system according to fiber orientation estimated utilizing the new method. The experimental results showed that samples' stiffness could be predicted with great accuracy by the improved FE model. Strain distribution on the tensile samples' surface, captured immediately before their first macroscopic failure, was found to be highly inhomogeneous at borders due to matrix-dominated nonlinearities. In these regions, a maximum 15% strain error of the improved FEA model was detected. The technique will be used in the future using UV-visible ink to minimize the visual impact on manufactured parts and a general 3D formulation is under development for the analysis of in-plane fiber misalignment in curved components with complex shapes.

2.5 SUPPLEMENTARY DATA ON FIBER MISALIGNMENT ANALYSIS IN PCM-UD COMPOSITE MATERIALS BY FULL FIELD NODAL METHOD

2.5.1 Algorithm for corner's detection

In a first step, each of the 3 channels of the original RGB image (Figure 2.10 a) was equalized, and a median filter was applied to mitigate the noise. Images showed several drops resp agglomeration of release agent residues [72]: their high repeatability in color allowed to implement of a custom RGB filter to remove them; results are shown in Figure 2.10 b.

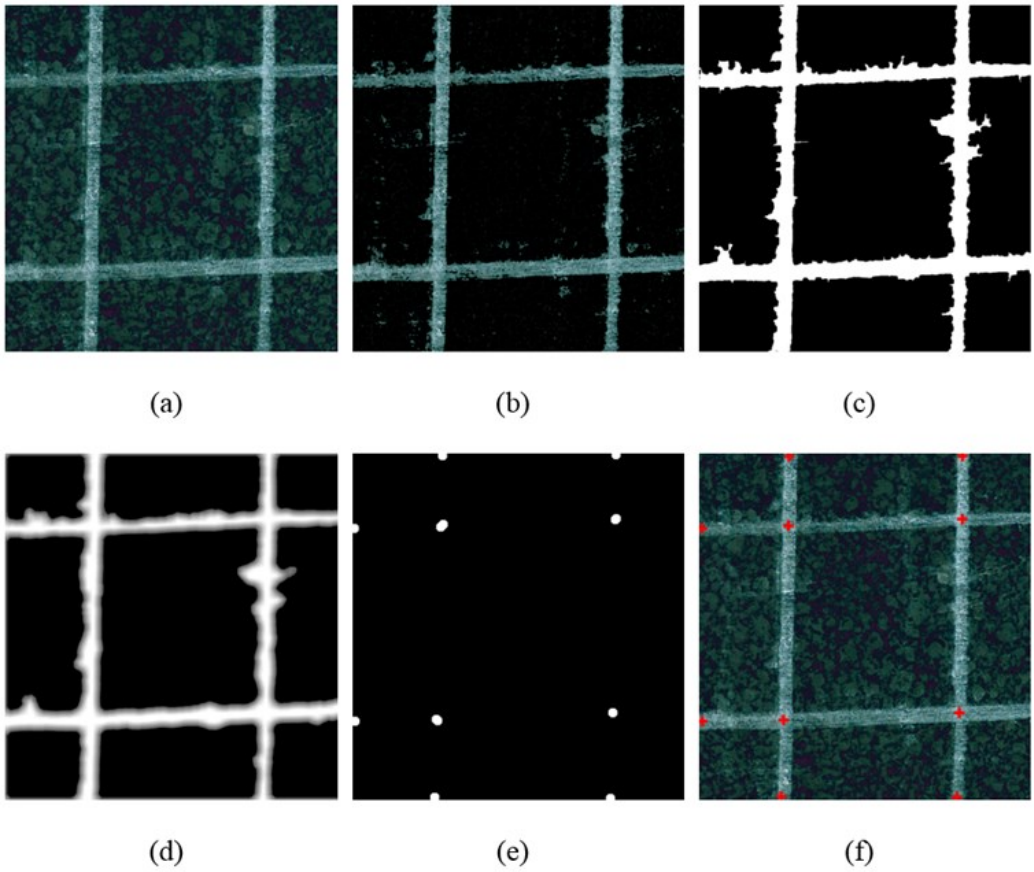

Figure 2.10: Step-by-step image processing on a portion of the plate. a) original image b) image after RGB filtering c) image after binarization d) average filtered BW image e) dilatated branch point of the BW image f) original image with corners detected by the algorithm.

Images were binarized (Figure 2.10 c) and eroded employing the "thinning" technique to detect the centerline of the grid: an average filter of 50 pixels was applied on the binary image (Figure

2.10 d) and the 'thin' option of "bwmorph" (an inbuilt Matlab function) [2] was automatically repeated until one-pixel width skeleton was obtained. Spur branches and single unconnected pixels were removed, and branch points of the skeleton were detected by using the 'brenchpoint' option of bwmorph. The grid's corners were finally detected by the coordinates of the centers of mass, shown in Figure 2.10 f, of the dilatated branchpoint image (Figure 2.10 e).

2.5.2 Prepreg characterization

To account for the initial misalignment, a prepreg characterization was conducted with a similar procedure to the one described in [73]. Six single-ply samples were extracted at different locations from the same roll of prepreg used in section 2.2.1 of the present work.

The dimension of the samples was about 100 mm in the 1-direction and 30 mm in the 2-direction. The mid wide of the samples was coincident with the mid wide of the roll and with two lines, located 30 mm far from the edges.

To minimize fiber distortions, samples were cured using the vacuum bagging technique in an oven at a temperature of 140°C for 3 hours over a flat aluminum tool with a PTFE layer at the interface. A vacuum of about 101kPa was applied and maintained during the whole curing cycle. After curing, each sample was cut at about 5° in the 1-3 plane and split into 4 wedges as shown in Figure 2.11.

Figure 2.11 Cured specimen sectioned at 5°

Each wedge was mounted in a cold embedding acrylic resin (Technovit® 4006, Kulzer GmbH, Wehrheim, Germany). Mounted samples were polished using modified metallographic techniques and examined using a Zeiss Axio Observer 3 at a magnification of 200x.

Digital micrograph images were stitched together to cover a larger representative area and analyzed using a custom code written in Matlab R2019a.

The semi-automatic script performs several image modification and ellipse fitting techniques to calculate and output statistics on the population of identified fiber footprints. A frequency table was generated by populating 0.025° wide bins for each analysis.

Due to the high magnification required by the method and the limited depth of field, the focus was frequently fine-adjusted. This fact caused faults in automating image-stitching, and analysis of the specimens' full length was unfeasible. For these reasons, frequency tables on the most extensive possible stitched images were created, bins summed, and finally normalized using the total number of measured fibers for each specimen.

(a)

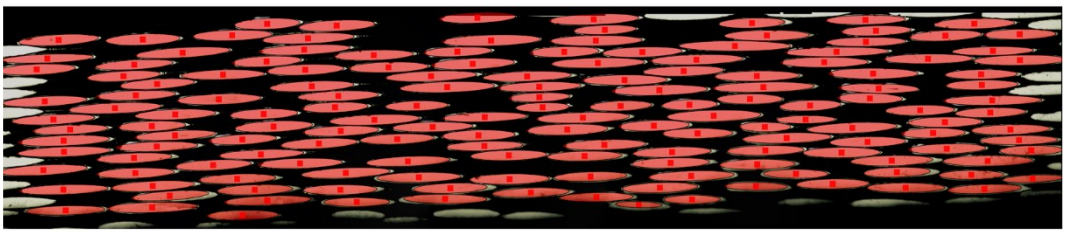

(b)

Figure 2.12: Image processing analysis for calculation of fiber orientation. a) stitched image micrograph, b) processed image with ellipse fitting algorithm

The output of the ellipse fitting software is shown in Figure 2.11. Concerning Figure 2.11 b, the presence of "tails", i.e. sharp corners in white out of the best fitting ellipse, can be identified.

However, as demonstrated by Potter and al. [74], they are documented to overestimate the ellipse's major diameter, altering the measurement of in-plane misalignment. For this reason, the code was studied to omit them in processing and calculations.

Results of prepreg characterization are reported in Table 2.2. Populations of the 6 samples were always consistent independently from the position on the roll, and a small standard deviation in the range 0.82°-0.92° was observed, thus demonstrating the high alignment in direction 1 of the material used in this study.

Table 2.2: In-plane fiber misalignment standard deviation for the material

ID	Axial position	Population	Standard deviation of in-plane misalignments
S1	Left	11287 fibers	0.92°
S2	Center	11094 fibers	0.82°
S3	Right	10974 fibers	0.89°
S4	Left	11107 fibers	0.87°
S5	Center	10473 fibers	0.85°
S6	Right	10893 fibers	0.90°

Indeed, about three-quarters of the literature citing Yourgartis has interpreted the standard deviation as a characteristic angle of the prepreg, sometimes referred to as "initial fiber misalignment" [75–77].

According to its definition, the material's initial fiber misalignment angle is representative of populations of footprints and therefore needs to be treated statistically. The prepreg's overall standard deviation, calculated as "pooled standard deviation" [78] of samples S1-S6, is 0.88° and used by authors to account for the initial misalignment angle prepreg.

Chapter 3. LATTICE MATERIAL INFILTRATION FOR HYBRID METAL-COMPOSITE JOINTS: MANUFACTURING AND STATIC STRENGHT

Luca Raimondi[a*], Luca Tomesani[a,b], Lorenzo Donati[a,b], Andrea Zucchelli[a,b]

[a]*DIN – Università di Bologna, Viale Risorgimento 2, 40136 Bologna, Italia*

[b]*CIRI-MAM – Università di Bologna, Viale Risorgimento 2, 40136 Bologna, Italia*

The candidate is the main investigator of this study. He contributes to the conception and design of the study, experimental testing, data acquisition and analysis, manuscript drafting, revision, and approval. The work has been published on Composites Structures.

3.1 INTRODUCTION

The growing request for lightweight applications, especially for structural parts in the transportation and automotive industry, raises the need to develop innovative technological solutions for multi-material components, in which different functions are deployed in different regions by the best material for a specific need [79,80]. As an example, metal inserts can be introduced into a composite part in order to allow subsequent assembly operations. The tailoring of different materials within the same component is further enhanced as more weight can be saved by integrating multiple functions in the same component, leading to complex hybrid material solutions [50,81].

In this context, carbon fiber reinforced plastics (CFRP) are mostly used for their extreme stiffness to weight ratio and for the tailoring of the mechanical proprieties through specific layups, whereas metals are selected for their toughness, shock absorption ability, ease to be precisely cut and finished in view of assembly operations. The metal-composite interface has thus from a long time grown as an important issue for high value-added components [82].

The most widely used technique for joining such an interface is the adoption of the adhesive joint. The effects of adopting different material combinations over the strength of the joint have been recently studied both numerically and experimentally, and an extensive literature exists on the topic [83–90]. To obtain a strong and durable joint, a surface treatment of the adherends is

required to remove contaminants like lubricants, dust, loose corrosion layers, micro-organisms from the surfaces [91–94] and different physical and chemical surface treatment are available. However, at the industrial scale, they can be difficult to be implemented or will increase the overall production cost for material and time losses.

In order to enhance overall resistance of the bond toughness, in particular, in aerospace applications, the direct insertion of metal protrusions into the composite fabric has been used; protrusions are obtained at high cost by machining directly bulk metal parts [25] or shaped onto the metallic adherend by Electron Beam Melting or Laser Beam Welding [95–97]. Likewise, the penetrative reinforcing technique was used to link different fiber textiles by double-side pin insert extracted from a metal sheet by laser cutting [28,98].

More recently, the fast technological evolution in manufacturing has led, in the field of composites, to composite materials for high production rates, such as Advanced Sheet Molding Compound (ASMC) with short to medium fiber length; these materials can be compression molded into any kind of shape by warm tooling in a short production time [80]. The availability of ASMCs with good mechanical properties, either with thermoset or thermoplastic matrices [99,100], makes their adoption a viable solution for stiffness driven structural applications.

At the same time, in the field of metals, the additive manufacturing technique of selective laser melting (SLM) has led to the production of full density components in which very complex freeform shapes can be obtained at a relatively low manufacturing cost if compared to machining from the bulk. The continuous decrease of costs and the recent development of in-situ, in-process quality assurance methods [101–103] make SLM a suitable process for the manufacturing of metal inserts for hybrid material components.

In fact, by using SLM, the metal insert can be structured with an inner bulk core and an outer high complex surface where several ASMC tows can penetrate to realize a high strength and high toughness permanent bond [104]. This joining by infiltration can be performed by locating SLM inserts directly in the shape mold where the ASMC material is processed.

The infiltration process will be dependent on several key factors, related to both the ASMC material and the 3DP structure. Due to the engineered properties of the material on the SMC side, the overall fiber orientation [105], the strand length [99], the fiber/matrix volume ratio [100,106], the matrix viscosity as a function of pressure, temperature and time [107–109], should have an impact to the lattice infiltration. On the 3DP structure side, the geometry of the structure [110], the dimension of the cells, their distribution, the void to volume ratio (the density) [111,112], will also have a potential influence on the infiltration.

In this paper, the possibility to infiltrate a 3DP pyramidal cellular structure by SMC sheets in a one-step molding operation is experimentally evaluated, in order to understand the effect of some geometric and processing parameters. Several hybrid metal-composite joints with a complex interface were produced, in which both the effect of fiber orientation and the cell dimension were considered as representative of the main processing issues. The different configuration of two process parameters was then used for two distinct experiments: the first aimed at evaluating the infiltration process, the second for producing samples for mechanical characterization.

3.2 MATERIALS AND METHODS

3.2.1 Metal side

The SLM process was used to directly build the metallic adherend from AISI 316L onto the cylindrical platform of the machine (SISMA MYSINT100) with 99 mm in diameter. The chamber was preliminarily filled with argon to avoid oxidation of the component during the manufacturing process, with a residual oxygen content below 0.2%. An LPW 316 powder was used for manufacturing (LPW Technology Ltd, Runcorn, UK). Printing parameters were: 150W laser power, 50μm spot diameter 20μm layer thickness as suggested by [113] for higher density.

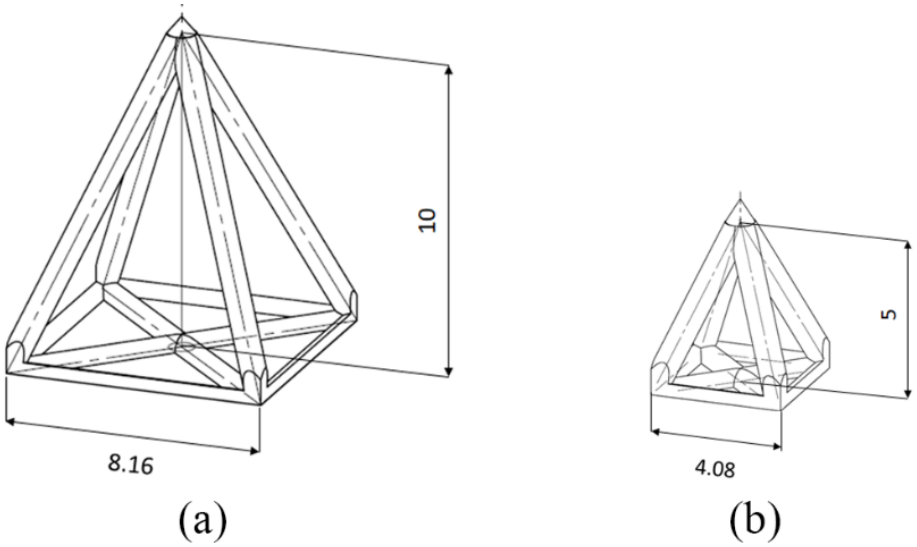

Figure 3.1: Two types of pyramids: a) big; b) small

The lattice structure which was chosen, among the available in literature, was the pyramidal one. The pyramidal structures was chosen because of its intrinsic high compressive stiffness thanks to stretch dominant behavior [112,114], due to its high efficiency in heat transfer [115–117] and, last but not least, due to the expected effect promoting the SMC charge flow during the moulding process. For the purpose of this study, two dimensions of square-based pyramids were printed: a big one with 8.16 mm side and 10 mm height and a small one with a 4.08 mm side and 5 mm height. For both, rod diameter was 0.80 mm, see Figure 3.1. Dimensions of pyramids and of rods, were chosen as a compromise between density of the structures, the accuracy obtainable with the 3D printing machine used in this work. The two types of pyramids were printed onto three different types of platform:

- Platform A, with a grid of 86 adjacent elements with 8.16 mm base side (Figure 3.2. a)
- Platform B, with a grid of 368 adjacent elements with 4.08 mm base side (Figure 3.2.b)
- Platform C, with a mix of separate elements for samples extraction (Figure 3.2.c)
    - 4 elements with one big pyramid each (BS, Figure 3.2 d)
    - 4 elements with 4 small pyramids each (SS, Figure 3.2 d)
    - 4 elements with flat surface for simple adhesion reference samples (FS, Figure 3.2 d)

After printing, all the grids were visually checked for imperfections. Care was taken in identifying an appropriate positioning of each grid over the platforms, either to reduce edge effects during infiltration and to cover the largest possible area. In Platform C the supporting elements of the pyramids were covered with a release film (PTFE) in order to ease samples extraction after the molding procedure.

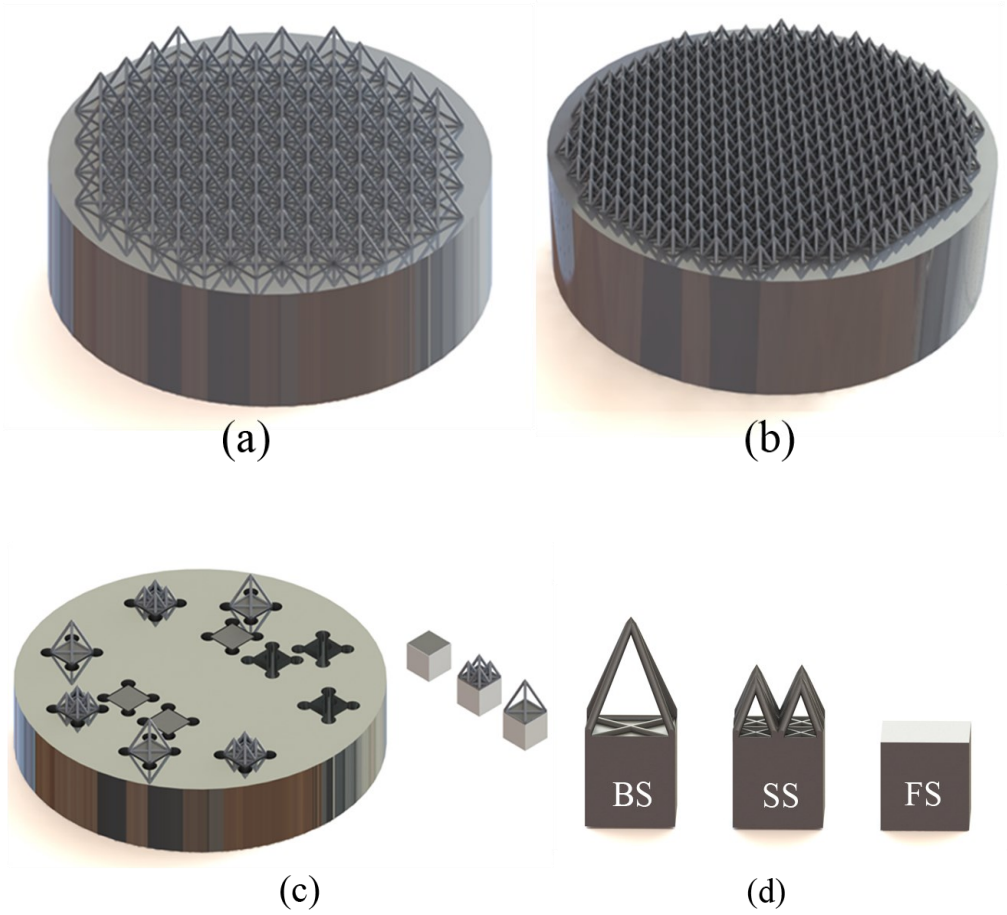

Figure 3.2: 3D printed grids on platform a) Platform A with a grid of big pyramids b) Platform B with a grid of small pyramids; c) Platform C for extraction of samples for material characterization d) metal adherends for mechanical characterization.

3.2.2 Composite side

To produce the composite adherend, an HexMC®/C/2000/M77 ASMC supplied by Hexcel, Duxford (UK) was used. Such a material is a carbon fiber prepreg (57% fibre volume fraction, Vf), formed by randomly distributed 50 mm long 8 mm wide chips, with an areal density of 2000

g/m^2 (approximate, as supplied) impregnated with M77 epoxy resin. M77 is a fast curing epoxy (3 min at 140 °C) specifically developed for compression molding.

To investigate the effect of prepreg orientation over processability, two plies orientation within the charge were adopted: (a) parallel to the grid interface and (b) orthogonal to the grid interface.

ASMC roll was extracted from cold storage 4 hours before cutting and put in a white chamber. To obtain the charge for condition (a), 10 circular layers of ASMC of 95 mm diameter were cut out and carefully stacked on top of each other to form a charge of 35 mm in height, as shown in Figure 3.3a; to obtain the charge for the condition (b), 35 mm width stripes of ASMC were cut using a sharp knife, then wound to form rolls with an average diameter of 95 mm, as shown in Figure 3.3b.

Figure 3.3: a) ASMC stacked with fiber orientation parallel to the platform interface; b) ASMC stacked with fiber orientation orthogonal to the platform interface.

3.2.3 Compression Molding

Eight different hybrid joints, four for infiltration evaluation and four for mechanical properties evaluation, were manufactured by co-curing the two ASMC stacks towards the three platforms in a custom AISI 316L mold, as shown in Figure 3.4 a-c and installed into an upstroke laboratory press. The whole experimental plan is depicted in Table 3.1.

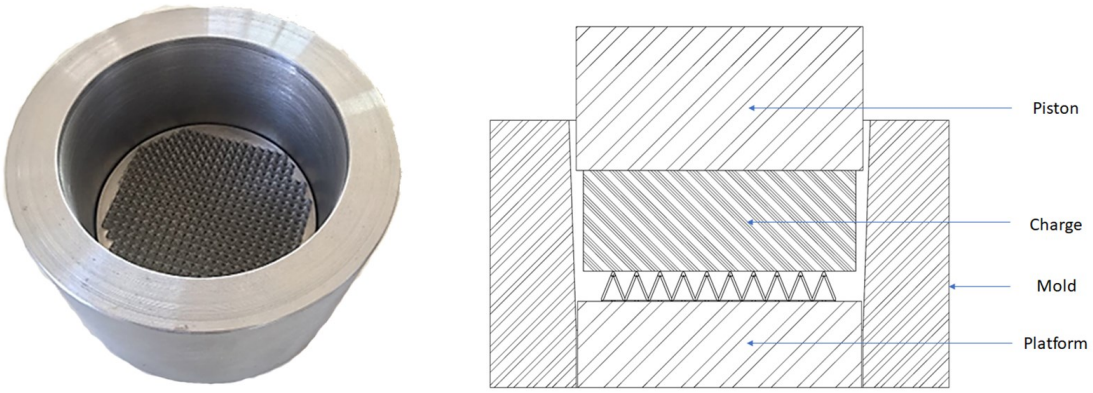

(a) (b)

Figure 3.4: a) Platform placed at the bottom of the mold b) pressing section

To ensure a uniform temperature distribution, both mold and 3D printed samples were uniformly preheated in an oven at a temperature of 150 °C and monitored by k-type thermocouples with a tolerance of ±2 °C. Care was taken in optimizing the compression molding force in order to avoid the possibility of pyramids collapsing. For this purpose, a compression test was performed on both platforms A and B, as reported in section 3.4.1 of supplementary information. As a result of this test, a maximum force of 24 kN was assumed for processing.

The temperature of the plates was set to 150 °C. Metal samples were assembled into the mold, prepreg was charged, and compression-molded, as shown in Figure 3.4 c for 4 minutes.

***Table 3.1**: Experimental Plan*

Type of Experiment	Number of molds produced	Platform Type	ASMC Orientation	Samples Produced
Infiltration	1	A	═	n.1 platform for visual inspection
	1	B	═	n.1 platform for visual inspection
	1	A	⊥	n.1 platform for visual inspection
	1	B	⊥	n.1 platform for visual inspection
Mechanical properties/evaluation of samples deformation after curing	2	C	═	n.8 samples BS (Big) n.8 samples SS (Small) n.8 samples FS (Flat)
	2	C	⊥	n.8 samples BS (Big) n.8 samples SS (Small) n.8 samples FS (Flat)

3.2.4 Infiltration evaluation

After curing, the type A and B hybrid joints aimed at infiltration evaluation were progressively milled orthogonally to the interface and visually checked, to put in evidence the presence of unfilled volumes and tow orientation.

3.2.5 Mechanical testing and data analysis methodology

After curing, the type C hybrid joint was cut into 24 square samples of 13 mm side, using a high-speed rotating diamond tool. Two types of samples were obtained, one with a single embedded pyramid with 8 mm side, the other with four adjacent embedded pyramids with 4mm side each; one more type of flat sample was produced as a reference for the conventional co-curing joining technique. The number of samples produced is reported in Table 3.1. Hybrid samples were monotonically loaded at a rate of 0.5 mm/min into an INSTRON 8033 universal testing machine equipped with a 2 kN and a 25 kN load cell, using the custom setup of Figure 3.5.

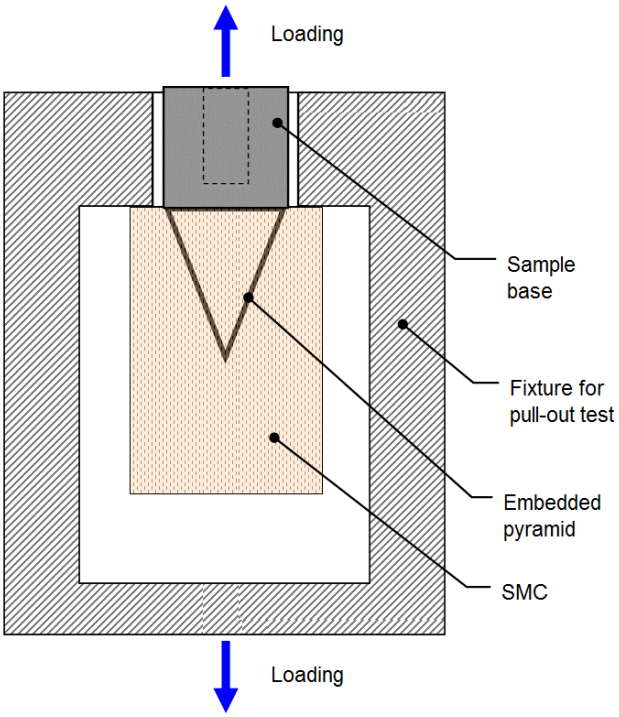

Figure 3.5: scheme of the testing fixture for pullout test and sample assembly

For each sample, composite adherends were linked to the hydraulic cylinder through a custom fixture with a 9 mm square hole on the top and aligned to the testing machine axis. The base of the metal adherend was connected to the load cell through a spherical connection using a threaded and a cylindrical joining, to prevent misalignment between the sample axis and the testing machine axis under loading. Load and displacement were recorded along the whole pullout test to evaluate load bearing capacity and the absorbed energy of each sample configuration.

In order to concentrate the analysis exclusively on the elasto-plastic behavior of the samples, thus excluding the elastic response of the testing equipment, corrected pullout displacement s was obtained by:

$$s = s_c - \frac{F}{K^*} \quad (1)$$

where s_c is the measured displacement of the cylinder, F is the opening traction load, and K^* is the stiffness of the load train, which was estimated by a tensile test on a dummy AISI 316L specimen tested with the same equipment.

The failure energy E was calculated as the area under the traction load versus the sample displacement:

$$E = \int F ds \quad (2)$$

3.2.6 Analysis of the fractured surface and Morphological characterization

After the pullout test, fractured surfaces of the samples were preliminary analyzed using a ZEISS Stemi 508 Greenough Stereo Microscope equipped with a 5MP ZEISS Axiocam 105 color camera to investigate for their macroscopic failure behavior. Analysis of morphological fracture modes was assessed via Scanning Electron Microscopy (SEM, Phenom ProX). When necessary (e.g. CFRP samples or samples fully covered by resin) analyzed surfaces were gold coated in order to make them conductive.

3.3 RESULTS AND DISCUSSION

3.3.1 Infiltration evaluation

In Figure 3.6 and Figure 3.7 the sequence of sections of the hybrid joints in which the prepreg tows were oriented parallel to the interface is presented. In Figure 3.6, where the grid was made of big pyramids, the ASMC was not able to reach the base of the adherend other than very near to the mold wall, generally stopping in the space between adjacent pyramids. As shown in Figure 3.6 b and Figure 3.6 c, excess of resin was identified within the grid in the form of large resin blocks. In Figure 3.7, where the fine grid was used, the resin of the ASMC could somewhere penetrate the lattice up to its base, especially in proximity to the mold wall, but still with vast unfilled areas see Figure 3.7 b, Figure 3.7 c and Figure 3.7 d.

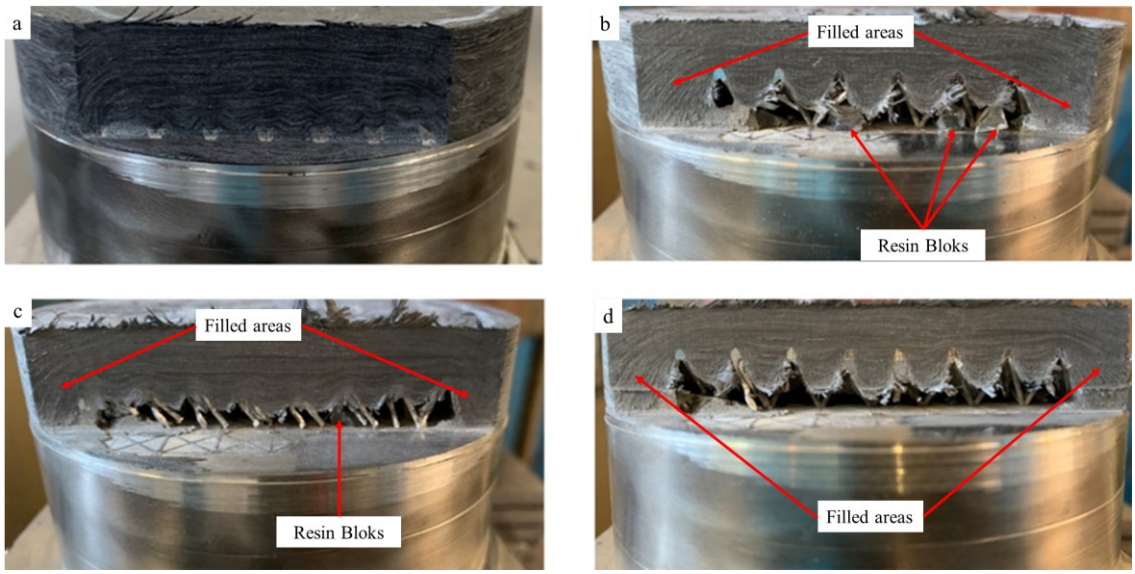

Figure 3.6: Infiltration results for Platform A (rough grid) - ASMC parallel to the interface

The reason for the easier filling near the mold wall may be related to the more efficient heating of the SMC material at the direct contact with the heated mold, whereas the material at the center of the joint could not be perfectly heated by the lattice, as the contact is limited to the vertices of the pyramids. It can be argued that the rough grid lattice, with a reduced number of heating

vertices, was much less effective in prepreg heating than the fine grid lattice, where a far larger number of heating points was present. Thus, a complete embedding of the lattice structure by the ASMC material was not successful for both configurations, with the fiber material generally draping around the vertices of the pyramids. About the general resistance of the lattices to processing flow, no appreciable plastic collapse of the structure was evidenced in both lattice structures in Figure 3.6 and Figure 3.7. This result shows that for this particular configuration, the interaction effects over the metal rods of the grid due to the motion of the ASMC during molding can be neglected. Processing force can be therefore adjusted up to the proportionality limit of the lattice material in compression to avoid appreciable plastic deformations on the metal part of the component.

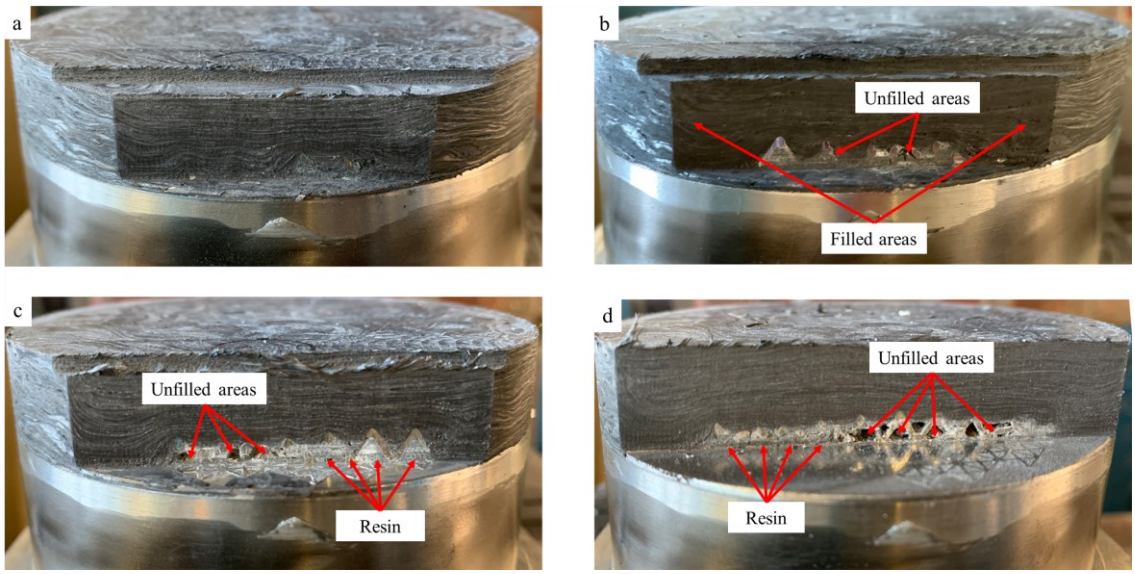

Figure 3.7: Infiltration results for Platform B (fine grid) - ASMC parallel to the interface

In Figure 3.8 and Figure 3.9, the sequence of sections of the hybrid joints, with prepreg tows oriented orthogonally to the interface, is presented. In Figure 3.8, where the grid was made of big pyramids, the ASMC was able to reach the base of the grid structure at any point of the interface, in particular also in the billet center, although some very clear plastic collapses of the pyramids can be seen at different locations. Such a behavior is related to the infiltration process. In fact during resin infiltration pyramids are compressed at their vertices, and lateral sides are bent since the ASMC flow is forced to fill their volume.

On the other hand, no collapse of the small pyramids was found (Figure 3.9). It can be stated, then, that complete embedding of pyramidal lattice material was feasible for both configurations in which the charge-constituting SMC tows were oriented orthogonally to the interface (thus aligned with the main molding flow direction), but only the fine grid structure could properly withstand the processing load.

Differently from what happened in the parallel configuration experiments, in the bulk of the ASMC material, diffuse wrinkling in strands is evidenced in all sections of both configurations, as a result of intense fiber displacement and consequent tow buckling. In particular, in Figure 3.8, where the rough grid lattice is shown, fiber distribution is highly irregular and both tows swirling, and wrinkling can be noticed, as a consequence of the higher displacement to be performed during the molding and, probably, also of the simultaneous buckling of the pyramids. As contrast to that, in Figure 3.9, the grid configuration with fine grid structure evidences a less severe and almost symmetrical wrinkling distribution about the central vertical axis.

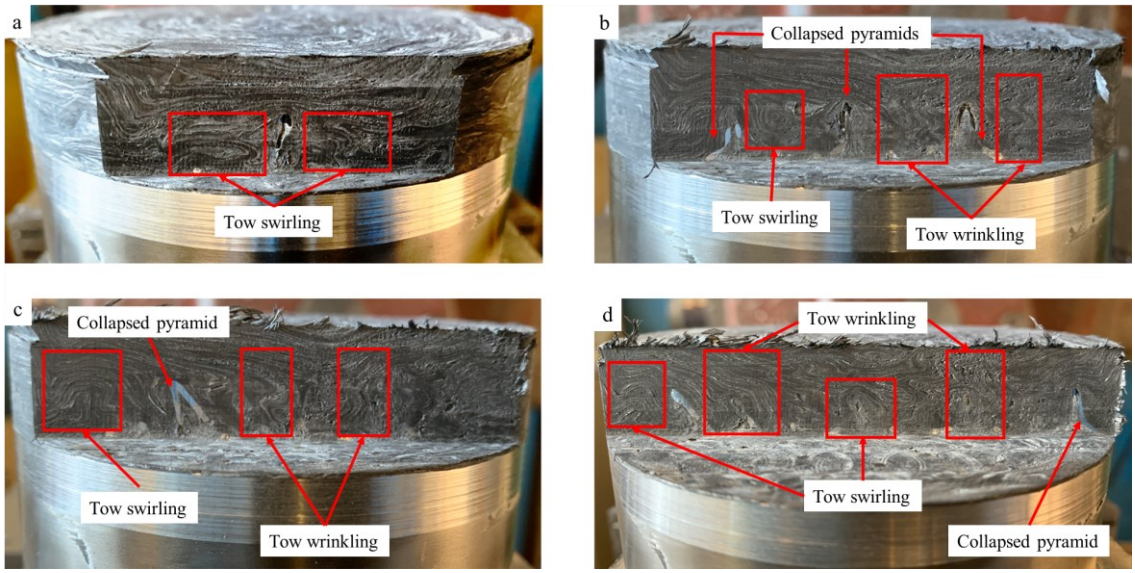

Figure 3.8: Infiltration results for Platform A (rough grid) - ASMC orthogonal to the interface

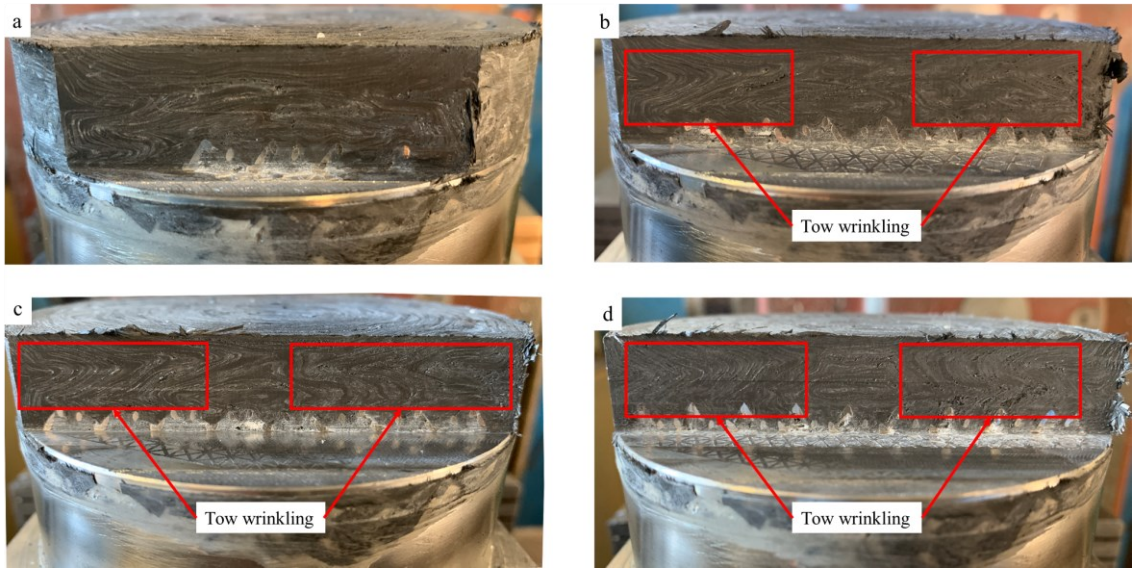

Figure 3.9: Infiltration results for Platform B (fine grid) - ASMC orthogonal to the interface

3.3.2 Mechanical Tests

Significant differences of mechanical properties were evidenced in the pull out tests depending on the preferential direction of the charge-constituting tows, as evidenced in Figure 3.10.

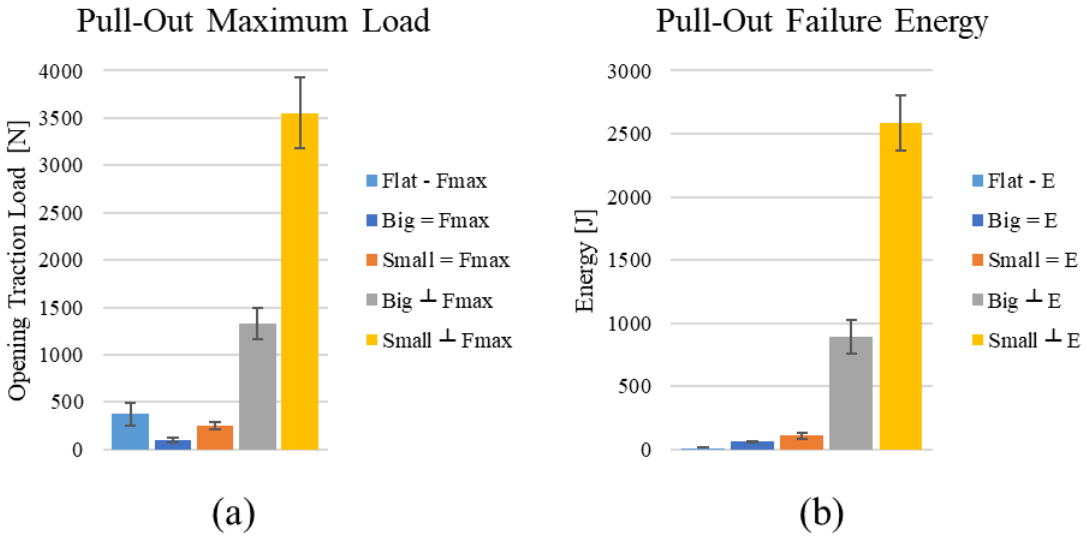

Figure 3.10: Summary of mechanical properties of the hybrid joints in the different tested configurations; 10a) Maximum Load; 10b) pullout failure energy

Samples whose pyramids were embedded by a charge with tows parallel to the interface evidenced much lower strength than those penetrated by tows arranged perpendicularly to the

interface, as a consequence of the defects already discussed in Section 3.3.1. Moreover, the large dispersion of data for the parallel configuration led to a coefficient of variation (CVs) greater than 20% for all samples, further demonstrating the instability of the parallel configuration.

On the other hand, remarkable results are obtained for the orthogonal configuration, in particular for the small pyramids one, for which an average maximum load of 3554 N was found in contrast to the 1334 N of the big pyramid case and the 374 N of the reference sample. Also, for failure energy, a mean value of 2584 J for the small pyramid samples greatly exceeded the 895 Joules of the big pyramid ones and the 32 J of the reference samples.

In Figure 3.11, the full pullout load-displacement curves for samples with orthogonal prepreg configuration are shown, evidencing excellent repeatability across all samples, with CVs values always lower than 14% in maximum pullout load and energy absorption except for the flat reference for which a CV of 25% was measured.

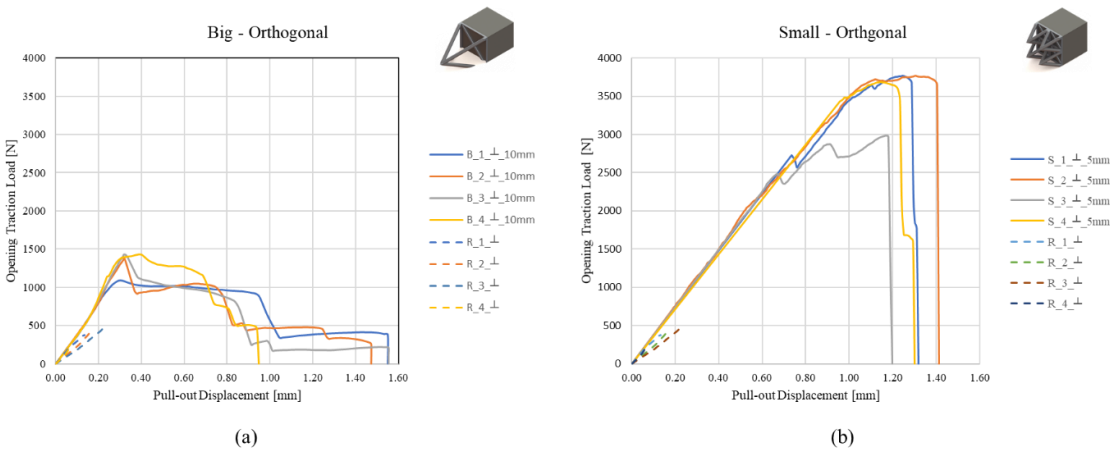

Figure 3.11: Load-displacement curves for both the orthogonal configurations. 11a) Big pyramids and reference samples; 11b) small pyramids and reference samples.

Samples with big pyramids showed a variable number of load drops during the test, often followed by wide “plateau” in which opening load was almost constant. This phenomenon, probably due to the progressive fracture of rods of the single embedded pyramid, provided a considerable increase in the energy absorbed. The maximum opening traction load was comparable (CV 12%)

among samples with big pyramids, resulting in a hybrid joint that was 3.6 times stronger to the flat unstructured solution.

It must be noticed that, during tractioning, samples with big pyramids exhibited an increase in stiffness of about 1.5% from an average value of opening traction load equal to 640 N up to their first macroscopic failure. As demonstrated in section 3.3.1 and as reported in section 3.4.2 of supplementary information, the compression molding process induces a partial buckling of the big pyramids. During pullout, the deformed pyramid is supposed to interact with the composite material to recover its original shape partially, thus leading to an incremental stiffening effect on the specimens.

In samples with small pyramids, a linear behavior between traction load and displacement was detected up to the 79%-90% of the maximum load. Afterward, a marked plastic zone exists, which noticeably contributes to enhancing the absorbed energy of the joint: for this configuration, fracture energy was considerably higher than those measured in samples with big pyramids and in reference samples, respectively. Except for one sample, for which a progression of load drops is evidenced, few and less marked load drops were generally encountered for this configuration, with no change in the slope of the pullout load-displacement curves.

Fracture analysis revealed that this behavior appeared in those samples in which voids and cavities were present. Maximum load was 2.7 times higher with respect to the big pyramids, and 9.5 times higher than the one measured on the flat reference. Pullout failure energy for this configuration was about three times higher than the one measured in samples with big pyramids and more than 80 times higher to the reference samples.

3.3.3 Analysis of the fractured surface and Morphological characterization

In the three types of samples infiltrated in the orthogonal configuration, different failure modes have been observed, and typical results of the stereomicroscopic analysis are shown in Figure 3.12.

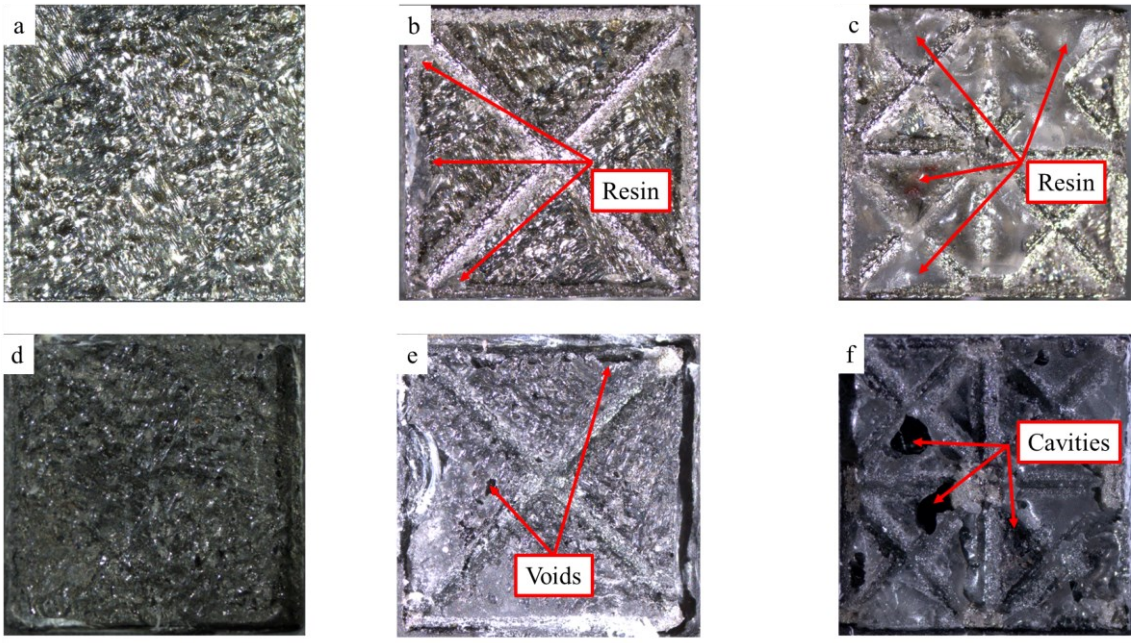

Figure 3.12: Fractured surfaces of samples infiltrated by the orthogonal configuration of tows. a), b) and c) metal side view, d), e) and f) CFRP side view; a) and d) reference (flat) sample; b) and e) big pyramid sample; c) and f) small pyramid sample;

On the metal side of the flat adherend (Figure 3.12 a) only traces of resin are present, suggesting an adhesive failure mode of the samples. On the other hand, at the CFRP side, no traces of metal were found, thus confirming the hypothesis of merely adhesive fracture (Figure 3.12 d).

In the case of samples with big pyramids (Figure 3.12 b), only small regions with traces of resin are visible at the metal surface: close to rod ends and along with the edge features of the pyramid. On the CFRP side (Figure 3.12 e), the resin is present almost everywhere, except for a limited number of small voids and cavities, probably due to trapped air or gas formation during processing. The general scarcity of resin on the metal side, together with the near-full density of resin on the opposite side, suggests that an adhesive failure mode occurred at the metal-resin interface. At the same time, a marked plastic deformation of the corners of the pyramid is observable i.e., where the pyramids failed under the pullout traction load. From these observations, it can be argued that a large part of the failure energy exploited during the test is due to the progressive yielding of those regions.

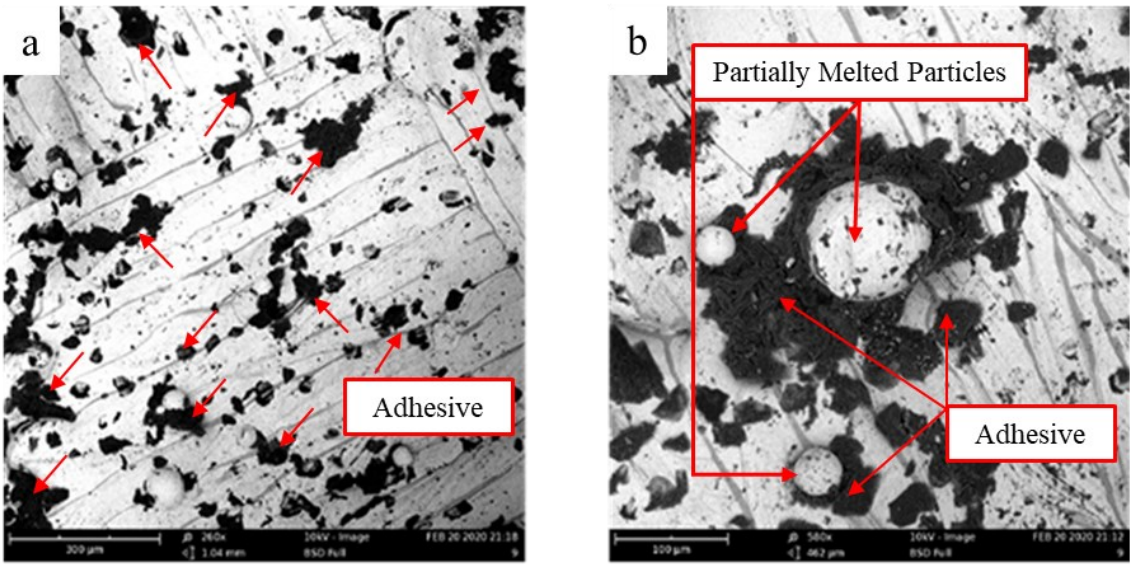

Figure 3.13: Magnification of fractured areas on the metal side for a) big pyramids, with a magnification of 260x, and b) big pyramids with a magnification of 560x

In the sample with small pyramids (Figure 3.12 c), the metal adherend appears to be uniformly covered by layers of resin with varying thickness, suggesting that the mode of fracture was typically cohesive, thus providing active participation of the interface to the overall joint resistance.

On the CFRP side (Figure 3.12 f), the adherend shows some voids, probably due to a local lack of infiltration or trapped air [118] . Similar to what happens with big pyramids, also with small ones, there is evidence of extensive plastic deformation at the pyramids' bases, where the rods are connected to the bulk metal. It must be noticed, then, that the much larger number of corners in the small pyramid samples well explains the much higher maximum load of this configuration.

In samples with the big pyramids, and flat references as well, higher magnification analysis performed on the metal side of fractured surfaces (Figure 3.13) evidenced a mixed cohesive/adhesive fracture in the range 50-100 µm (Figure 3.13 a). Thanks to the unique morphology of the surface obtained by SLM process, a relatively high number of partially melted particles in the range 15-45µm were present. The resin was interestingly able to more strongly adhere, thanks to an interlocking mechanism, as evidenced in Figure 3.13 b and already reported by [32] for hybrid joints with titanium alloys.

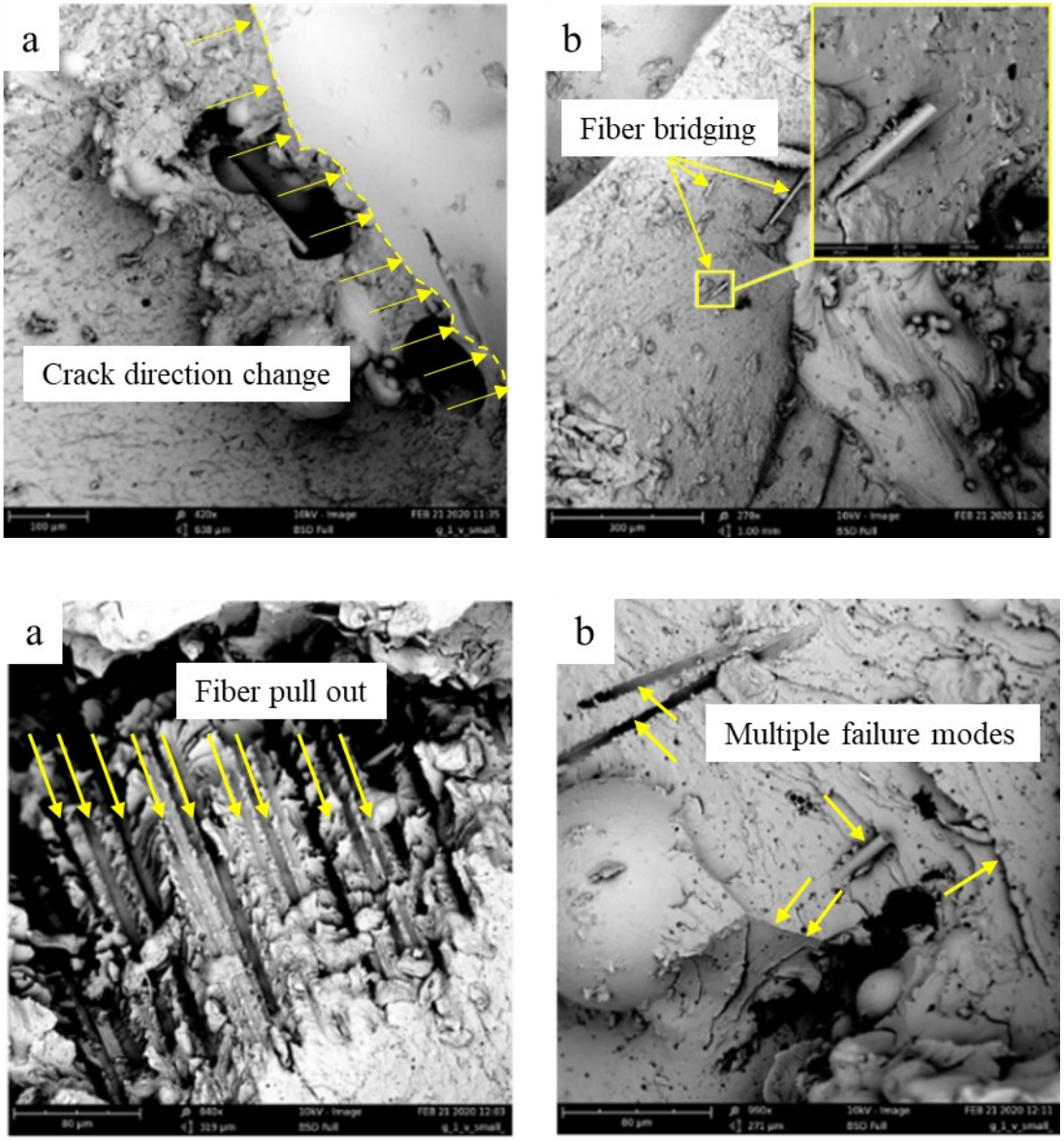

Figure 3.14: Fracture mechanisms in the small pyramids samples. a) crack direction changes b) fiber pullout c) fiber bridging and d) combination of previous mechanisms

In Figure 3.14, the fracture mechanisms present on the metal adherend of the small pyramid samples are shown. Here, the fully cohesive fracture that occurred during the pullout is evidenced by a mix of complex behaviors: the crack direction changes abruptly and frequently over the sample, as evidenced in Figure 3.14 a, fiber pullout (Figure 3.14 b) and fiber bridging (Figure 3.14 c) can be observed in regions close to the connections between the metal base and the rods

of the pyramids. The phenomena mentioned above generally coexist over the whole area of the metal adherend surface, as shown in Figure 3.14 d. It must be underlined that the presence of fibers at the fracture surface is a clear sign of successful infiltration of fibers, and not only resin, into the lattice, even for the small pyramid structure.

3.4 CONCLUSIONS

An innovative technological solution for the manufacturing of high strength and high toughness metal-composite interface is here investigated, in which a 3DP printed cellular structure at the metal side is infiltrated by ASMC composite. The main findings are the following.

- The infiltration process is successful only when, in the bulk charge, the ASMC tows are oriented orthogonally to the lattice interface, in order to ease fiber displacement during the molding. In the orthogonal configuration, both lattices with small and big pyramids were successfully infiltrated.
- The lattice with big pyramids undergone some buckling under compression molding, evidencing a weak structure for the infiltration process; on the other hand, the lattice with small pyramids perfectly withstood the compression molding loads.
- When tested to pullout, the fracture always occurs at the lattice base in both lattices. The finer lattice failed under a load 2.66 times higher than, the rougher one, owing to the higher metal section provided to the pullout test. Moreover, the finer lattice promotes the resin fracture to occur by cohesive failure instead of adhesive one.
- As a general remark for the investigated technology, the hybrid samples with finer lattice could exhibit a pullout opening pressure force of about 3500 N and pullout energy of about 2500 J, which were respectively 10 and 80 times higher than the values obtained on the flat reference. Mechanical properties were found to be always consistent in this case.

SUPPLEMENTARY INFORMATION FOR LATTICE MATERIAL INFILTRATION FOR HYBRID METAL-COMPOSITE JOINTS: MANUFACTURING AND STATIC STRENGHT

3.4.1 Compression test of the lattice material

Two compression tests were performed on sacrificial platforms A and B in order to evaluate the respective buckling modes and maximum sustainable loads. Tests were carried out under displacement control at a constant rate of 1 mm/min using an Instron 8033 universal testing machine equipped with a 250 kN load cell. The setup in the testing machine is evidenced in Figure 3.15 a. It consists of two "platens" in which the top one is adjustable by means of screws to accommodate for small angular misalignment, so to ensure an even distribution of loads during the test.

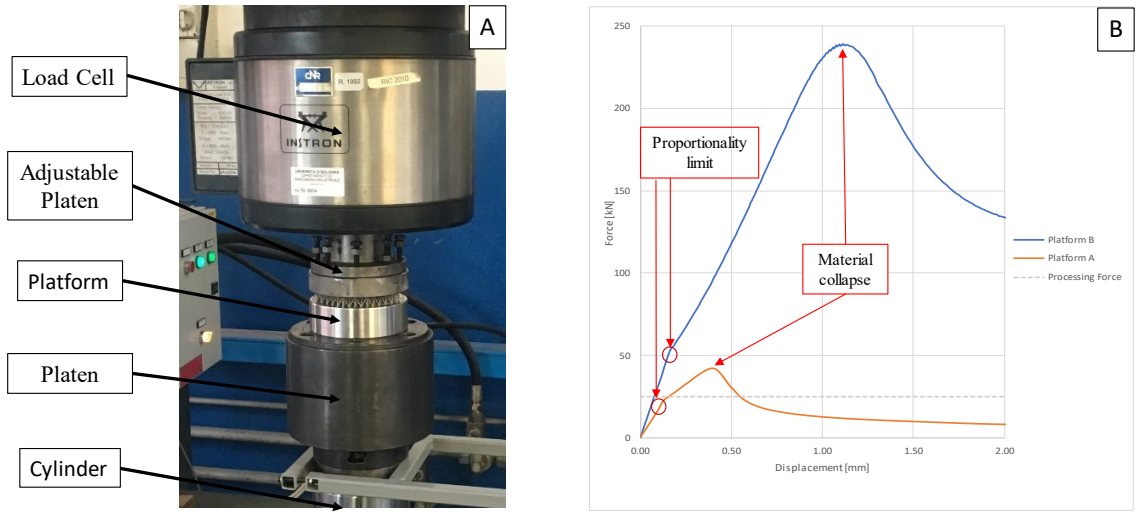

(a) (b)

Figure 3.15 Compression test of pyramidal lattice material. a) Testing equipment. b) Force-Displacement curves

The results for platforms A and B are represented in Figure 3.15 b, in which the respective load-displacement curves are shown. Proportionality limits were found to be 24 kN for the platform A (with big pyramids) and 54 kN for the platform B (with small pyramids). Afterward, the

lattice structure fails plastically with a maximum load of 42 kN for platform A and 239 kN for platform B.

The proportionality limit of 24 kN was then taken as a maximum load for the infiltration experiments. This load corresponds to a specific pressure of 30 bar on the SMC in the compression molding process, which is within the pressure interval suggested by the material producer.

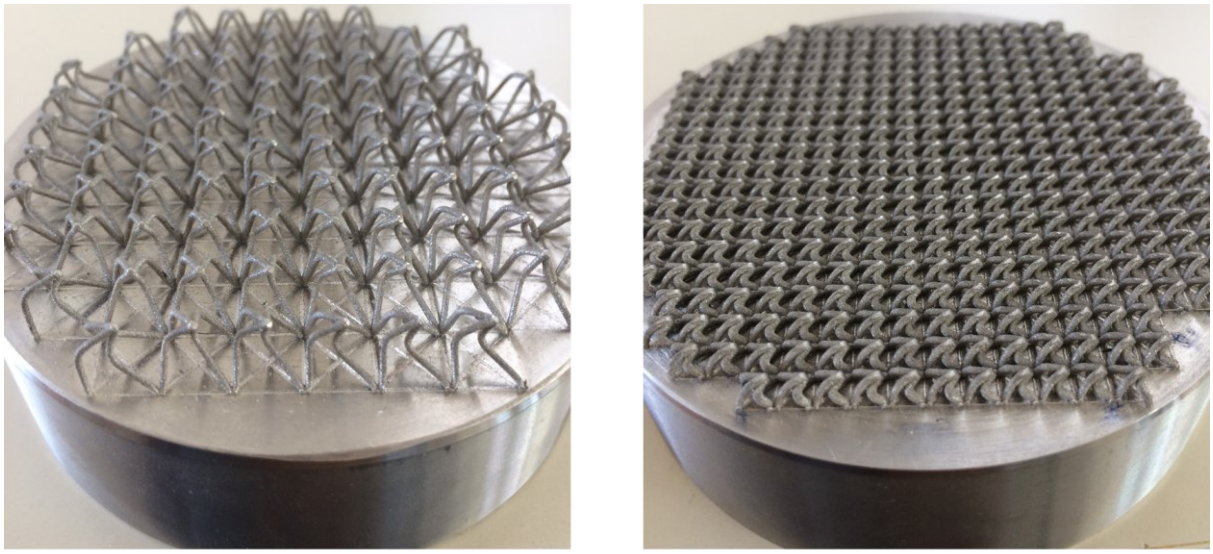

(a) (b)

Figure 3.16: Platforms A and B with buckled pyramids after compression test. a) Platform A; b) Platform B

3.4.2 Evaluation of pullout samples deformation

In order to precisely evaluate the effect of the compression molding procedure on the samples extracted from Platform C (which could not be tested by the procedure described in section S1), 8 samples, 4 with big pyramids and 4 with small pyramids, having the two prepreg configurations described in Table 3.1, were heated in a crucible at a temperature of 550 °C for 1 hour in order to obtain the degradation of the resin and extract the metal adherend from the sample.

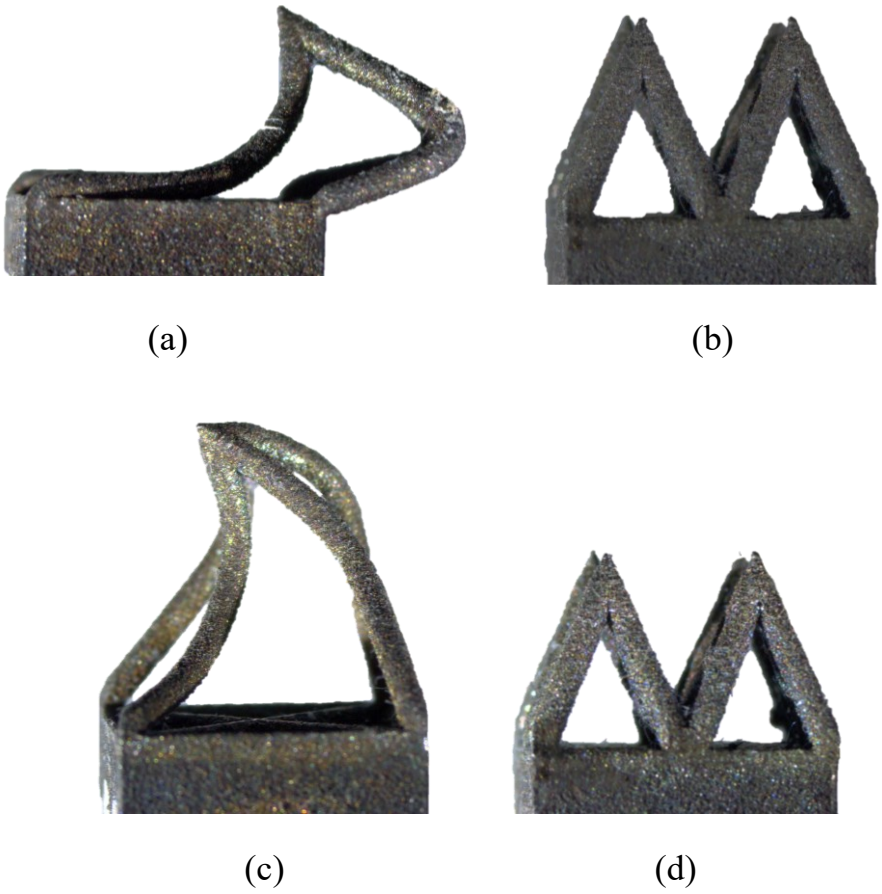

Figure 3.17: Pullout samples after thermal degradation of the resin. a) Sample B, parallel b) sample S, parallel c) sample B, parallel d) sample S, parallel

Typical geometries are shown in Figure 3.17. It can be seen the big pyramids undergone severe buckling in the parallel configuration of the prepreg and less severe buckling in the orthogonal configuration; on the other hand, the small pyramids well withstood in both prepreg configurations without any damage.

3.4.3 Fracture surface of CFRP adherends of samples with big pyramids

The fracture surface of CFRP adherend of samples with big pyramids were further investigated at a magnification of 270x to detect the presence of metal at the interface and to quantify the amount of resin left on it. The analysis revealed that no significant amount of metal was found on the CFRP surface despite the presence of some locally unmelted/partially melted particles, as

shown in Figure 3.18. Typical fractured surface exhibited a layer of resin of about 0.3 mm thickness (Figure 3.18 a and Figure 3.18 b) with underlying fibers, as evidenced in Figure 3.18 b. The footprint of partially melted particles, shown in Figure 3.18 c was observed.

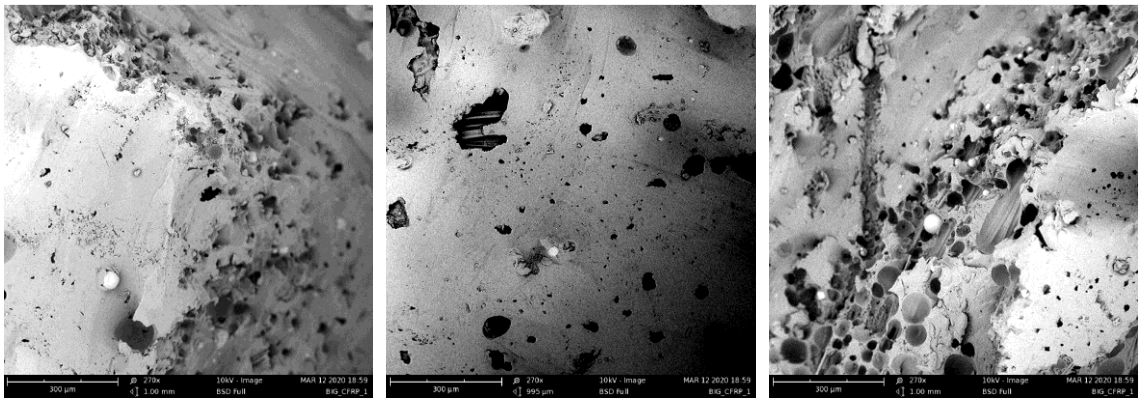

(a) (b) (c)

Figure 3.18: Typical fracture surface over CFRP adherends. a) resin with trapped partially melted metal particles; b) resin with underlying fibers; c) resin and fibers with embedded particles and voids.

Chapter 4. EXAMINING THE OPTIMIZATION FOR BUCKLING RESISTANCE OF TWO THREE-DIMENSIONAL LATTICE ARCHITECTURES

Luca Raimondi[a *], Luca Tomesani[a,b], Andrea Zucchelli[a,b*]

[a]*DIN – Università di Bologna, Viale Risorgimento 2, 40136 Bologna, Italia*

[b]*CIRI-MAM – Università di Bologna, Viale Risorgimento 2, 40136 Bologna, Italia*

The candidate is the principal investigator of this study. He contributes to the conception and design of the study, data acquisition and analysis, manuscript drafting, revision and approval. The work has recently submitted to Journal of the Mechanics and Physics of Solids.

4.1 INTRODUCTION

Cellular Solids and Structures (CSS) are a class of metamaterial with increasing interest in several industrial sectors thanks to their unique possibility to extend the constitutive material property space by a tailored design of their mesostructure [119]. Because of their flexibility, engineered CSS, have recently found increasing applications in transport (e.g., aerospace [120–124], mobility [125,126], rail [127–129]) as well as in the biomedical sector [130].

At their mesoscale, i.e in a range spanning from 0.1 [mm] to 10 [mm], CSS materials essentially consist of an interconnected network of struts or plates that form the edges and faces of the unit cell [131]; a CSS is, in this context, a theoretically infinite periodic cluster of unit cells that are packed together form the solid metamaterial.

Architected CSS are often referred to as lattice structures (LS), mainly when they comprise location-specific struts and nodes [132–134]. Several new classes of LS were developed by embedding different cell architectures at multiple scales: ultra-light/ultra-stiff [135,136], shape recovering [137], negative Poisson's ratio [138–141], close to infinite bulk-to-shear modulus ratios [142,143], high specific energy absorption [144] or thermal and vibration insulators [145].

Traditional manufacturing methods can be challenging to produce high complexity cell structures with precise geometries [146–149].

The extreme development over the last decades in additive manufacturing (AM) has vastly expanded the design and manufacturing possibility for creating novel LS [110,134,150–154] with an ever-increasing level of precision.

Many theoretical, numerical, and experimental bodies were dedicated to designing new lattice arrangements and studying their properties, as documented by several recent reviews [155–157]. Ashby, Gibson, Fleck, and Dhespande [112,158–161] are well known for developing closed-form mathematical formulations to describe the performance of LS in terms of Young modulus, yielding stress, and critical buckling load using beam and column theory. Their studies analyzed the unit cell by exploiting symmetry and assuming that the struts were pin-jointed. Although they provide a highly used design framework in selecting unit cell geometric parameters, the accuracy of the results of these analytical models with experimental and numerical results through the finite element method (FEA) is mixed in the literature [162,163]. Hanks et al. [163] report that analytical models tend to overestimate the modulus with respect to FEA and experimental data; Moreover, yielding stress predicted by analytical models overlap with FEA results if bending in struts is negligible; A particularly relevant comment is that the aforementioned analytical models do not account for the contribution of the node to the unit cell's overall mechanical properties, as pointed out by Meza and others [164].

Due to the nature of their mesostructure, elastic buckling and plastic yielding are two of the most occurring failure mechanisms that affect the compressive strength of LS. Several studies demonstrate that buckling may occur either at strut level [165–169], at the material level, or in-between [170].

On the other side, from macroscopic stress-strain curves, changes in slope due to yielding or buckling are challenging to distinguish [163]. Considering that the critical buckling load of a slender column scales by two orders of magnitude with its decreasing radius with respect to yield

stress, significant strength improvements can be achieved by optimizing the buckling resistance. Researchers have employed different methods to optimize the unit cell design against critical buckling load P_{cr}. One of the most direct way, as suggested by Deshpande [112] was the adoption of the well known Euler's formula:

$$P_E = \frac{n^2 \pi^3 E_s a^4}{4\, l^2} \tag{1}$$

Being a, l the radius and the length of the strut, E_s its elastic modulus and n a factor depending on the rotational stiffness of the nodes [171]. Despite its apparent simplicity, a proper selection of the coefficient n for Eq. (1) has reported to be challanging (see [172–175] amongst others). Moreover the formula does'n account for the lateral deflections due to the actual pre-stressed state of the cell under a given loading condition and neglects out-of-plane deformations.

Meanwhile, FEA eigenvalue buckling was adopted by several researchers and found to be consistent with experimental data [176–180].

In the attempt to provide a reliable model for optimizing unit cell design against buckling, an analytical model was developed and compared to the existing ones available in the literature. The investigation focuses on two cell types in this work, specifically the pyramidal and the tetrahedral (see Figure 4.1), but there are no constraints to extend the methodology to more complex shaped cells. Effects of strut length l, inclination angle ω, and strut diameter d over mechanical propertis are analized in detail.

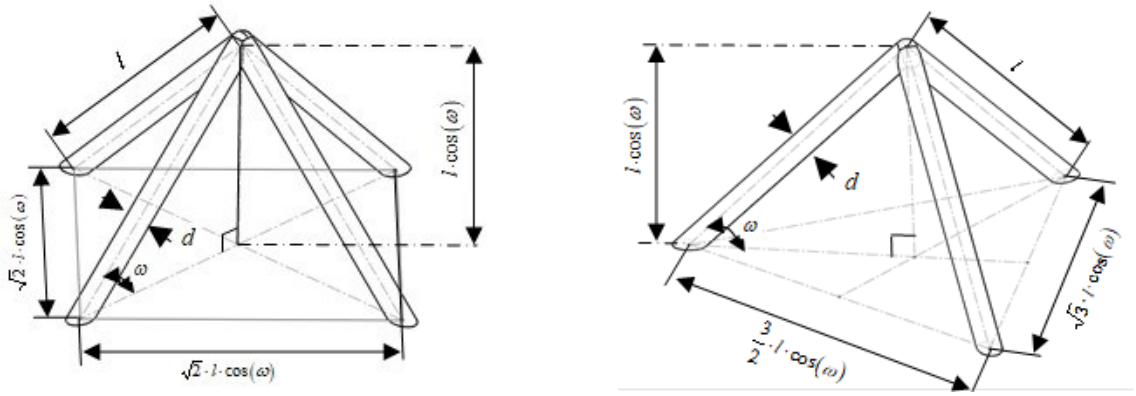

Figure 4.1: The two unit cells analyzed in this study with their characteristic dimensions. a) regular pyramidal cell. b) regular tetrahedral cell.

The model's accuracy is analyzed using FEA analysis, and the effect of the contribution of nodes to mechanical properties is addressed.

4.2 MATERIALS AND METHODS

The section is conceptually split in two. Section 4.2.1 illustrates an analytical framework to model stiffness, deflection, and internal reaction forces in a lattice cell. An analytical model to account for the effects of membrane stress on lateral deflection is illustrated in section 4.2.2. Numerical validation methods is illustrated in section 4.2.3.

4.2.1 Modeling for pre-stress analysis

In this study, struts are modeled as interconnected beams with rigid nodes, as shown in Figure 4.2. To study the influence of shear and rotational bending effect during deformation of the structure, a 3D Timoshenko beam model was adopted for the analysis.

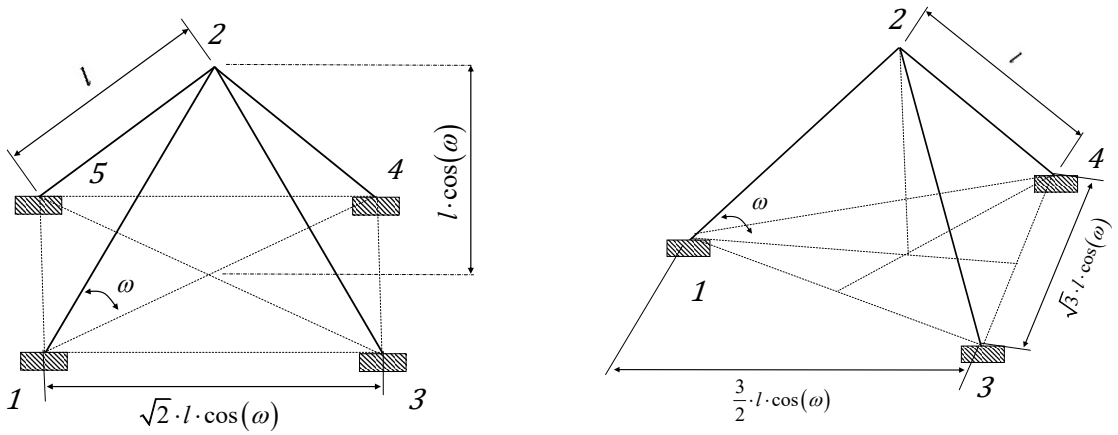

(a) (b)

Figure 4.2: Beam model of (a) pyramidal and (b) tetrahedral cell with rigid end nodes and built-in constraints

Each node possesses six degrees of freedom i.e. normal displacement (u_{ix}) two out of axis mutually orthogonal displacements (u_{iy} and u_{iz}), torsion angle (θ_{ix}), and two out of axis mutually orthogonal angles (θ_{iy} and θ_{iz}) (see Figure 4.3).

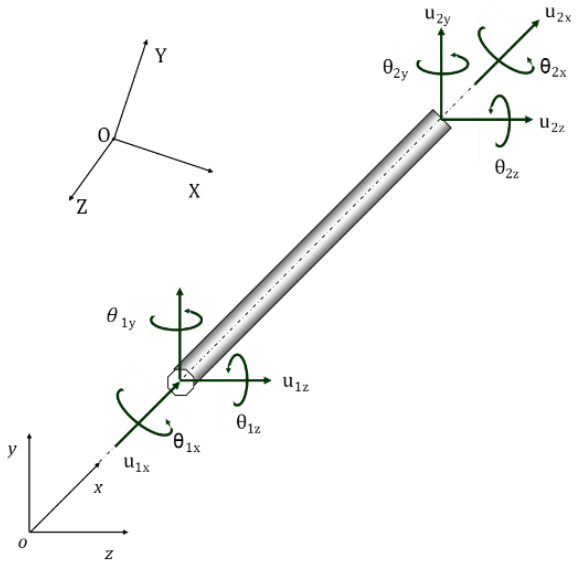

Figure 4.3: The global ($OXYZ$) and local ($oxyz$) reference system for the 3D beam and local displacement

Respective forces are axial load, two out of axes mutually orthogonal shear load, torque, and two out of axes mutually orthogonal bending moment. In the element reference system, the relationship between generalized forces f and generalized displacement δ at node i and j are:

$$\begin{Bmatrix} f^e{}_i \\ f^e{}_j \end{Bmatrix} = [K]^e \begin{Bmatrix} \delta^e{}_i \\ \delta^e{}_j \end{Bmatrix} \tag{2}$$

A closed-form version of the element stiffness matrix is given in [181] and reported in Eq. A1 of Appendix 1. In Eq.A1 we have denoted with E the Young modulus and with G the shear modulus of the material. A is the cross sectional area, I_y and I_z are the moment of inertia of the cross-section to y and z axis, while I_p is the polar moment of inertia.

For cylindrical beams, $A = \frac{\pi d^2}{4}$, $I_y = I_z = \frac{\pi d^4}{64}$ and $I_p = \frac{\pi d^4}{32}$. In Eq. A1, shear stiffness is accounted by $\Phi y = \frac{12\,E\,I_z}{k_s G\,A\,l^2}$ and $\Phi z = \frac{12\,E\,I_y}{k_s G\,A\,l^2}$, where the term k_s is the so-called geometrical factor. For a circular cross-section $k_s = 9/10$ and $\Phi y = \Phi z = \Phi$

Since $[K]^e$ is defined in the local $oxyz$ reference system while struct of cells and global displacement are defined in the global $OXYZ$ one, a transformation of the stiffness matrix is required. We introduce

$$[\Gamma] = \begin{bmatrix} l_{ox} & m_{ox} & n_{ox} \\ l_{oy} & m_{oy} & n_{oy} \\ l_{oz} & m_{oz} & n_{oz} \end{bmatrix} \tag{3}$$

as the matrix of direction cosines for the ox, oy, oz directions measured in the datum $OXYZ$ reference system. Being $[\Gamma]$ formed by orthonormal unit vectors, $[\Gamma]^T = [\Gamma]^{-1}$. The transformation matrix is thus given by:

$$[T]^e = \begin{bmatrix} [\Gamma] & \mathbf{0} & \mathbf{0} & \mathbf{0} \\ \mathbf{0} & [\Gamma] & \mathbf{0} & \mathbf{0} \\ \mathbf{0} & \mathbf{0} & [\Gamma] & \mathbf{0} \\ \mathbf{0} & \mathbf{0} & \mathbf{0} & [\Gamma] \end{bmatrix} \tag{4}$$

and element stiffness matrix in global coordinates is therefore given by

$$[\bar{K}]^e = [T]^{eT}[K]^e[T]^e \tag{5}$$

The stiffness matrix $[\overline{\mathrm{K}}]$ of the whole structure can be easily obtained by assembling all the element stiffness matrices obtained following the procedure described herein [182]. For both pyramid and tetrahedron, the nodes at the base of the cells were assumed to be built-in constrained. A vertical unit force $F = 1$ [N] was applied at the tip of both cells to retrieve the uknown displacements of the upper node 2 (see Figure 4.2), by solving the linear system

$$[\bar{K}]\,\{\bar{\Delta}\} = \{\bar{F}\} \tag{6}$$

The displacement vector $\{\bar{\Delta}\}^e$ for each beam in the global reference system was then reconstructed. Nodal forces for each member in the local reference system were calculated using the transformation

$$\{F\} = [K]^e[T]^e\{\bar{\Delta}\}^e \tag{7}$$

Results were stored and used for building the following geometrical stiffness matrix.

4.2.2 Modeling for buckling

In this work, the effects of membrane stress on lateral deflection are accounted for by a matrix $[Kg]^e$ wich augments the conventional stiffness matrix $[K]^e$. For a beam element, elements of $[Kg]^e$ are generally a function of geometry (such as beam length and shape of the cross-sectional area) and pre-stressed loading conditions. We call $[Kg]^e$ the geometrical stiffness matrix, although several other definitions are commonly used (such as “stress-stiffness matrix” or “initial stress stiffness matrix”).

In literature are reported different formulations of $[Kg]^e$. In this work, we have adopted the formula reported in Eq. A2 because it accounts for the torsion and is given in a closed-form [183,184]. The rotation of the geometrical stiffness matrix in the global reference system and assembly procedure is identical to the one explained in the previous Section 4.2.1. Eigenvalue buckling is based on linear perturbation and can be predicted by using the equation

$$\{P_{cr}\} = 0 + \lambda_i\{\bar{F}\} \tag{8}$$

where P_{cr} is the critical load at which the straight pre-buckling equilibrium configuration ceases to be a stable state of equilibrium (and an alternate buckling configuration is also possible at load P_{cr}) and λ_i is the scalar eigenvalue. Eigenvalue buckling formulation is given by

$$[\bar{K}] + \lambda_i[\overline{Kg}]\{\psi_i\} = \{0\} \tag{9}$$

In Eq. (11) $[\bar{K}]$ is the global stifness matrix, $[\overline{Kg}]$ is the global stress-stiffening matrix, λ_i is the i-th eigenvalue (or load multiplier) and $\{\psi_i\}$ the i-th eigenvector of displacement.

4.2.3 Numerical simulations

After a pre-stress analysis, numerical simulations were performed using ANSYS APDL eigenvalue buckling solver [185]. Each beam was meshed using 20 BEAM188 elements. The formulation of BEAM188 element is based on Timoshenko beam theory which includes shear-deformation effects. The element provides options for restrained warping of cross-sections and is suitable for analyzing slender to moderately stubby/thick beam structures. Material was supposed to be a steel, with a Young modulus of 200 [GPa] and a poisson ratio $\nu = 0.3$.

To validate results from section 4.2.1, cells with 10 different diameters (0.15 [mm], 0.25 [mm], 0.5 [mm], 0.75 [mm], 1 [mm], 1.25 [mm], 1.5 [mm], 1.75 [mm], 2 [mm], 2.25 [mm] and 2.50 [mm]) and 20 different strut lengts (from 0.5 [mm] to 10 [mm] at incremental steps of 0.5 [mm]) were investigated over varing inclination angle (from 5° to 90° at incremental steps of 2.5°) for a total of 7700 data point per each cell topology. To validate results from section 4.2.2 cells with 9 different diameters (0.5 [mm], 0.75 [mm], 1 [mm], 1.25 [mm], 1.5 [mm], 1.75 [mm], 2 [mm], 2.25 [mm], 2.50 [mm]) and 20 different strut lengts (from 10 [mm] to 20 [mm] at incremental steps of 1 [mm]) were investigated over varing inclination angle (from 5° to 90° at incremental steps of 2.5°) for a total of 6300 data point per each cell topology.

4.3 RESULT AND DISCUSSION

4.3.1 Modeling for pre-stress analysis

Calculated deflection of the tip of the pyramidal cell under the vertical unit force exhibits only a vertical component and is reported in Eq. (10)

$$\delta_{pyr} = -\frac{l^3(\Phi+1)}{2E\left(cos(2\omega)\left(12I - Al^2(\Phi+1)\right) + Al^2(\Phi+1) + 12I\right)} \tag{10}$$

and deflection of the tip of the tetrahedral cell under the same loading condition is reported in Eq. (11)

$$\delta_{tet} = -\frac{2l^3(\Phi+1)}{3E\left(cos(2\omega)\left(12I - Al^2(\Phi+1)\right) + Al^2(\Phi+1) + 12I\right)} \tag{11}$$

For the pin-jointed version of both cells, deflection is given by Eq. (12):

$$\delta = -\frac{l}{nEA\ sin^2(\omega)} \tag{12}$$

with $n = 4$ for the pyramidal cell and $n = 3$ for the tetrahedral cell. It is worth mentioning that deflections predicted by both Eq. (10) and Eq. (11) are influenced by the nodal connectivity as demonstrated by the presence of both the moment of inertia I and the quantity Φ.

For degenerate cells in which $\omega = {}^{\pi}/_{2}$, from Eq. (10) and Eq. (11) we get $\delta_{pyr} = \frac{l}{4EA}$ and $\delta_{tet} = \frac{l}{3EA}$. This results are consistant with both Eq. (12) and elementary beam theory; due to symmetry the unit force is equally distributed in the 4 rods of the degenerated pyramidal cell and in the 3 rods of the tetrahedral cell. For $\omega = 0$, Eq. (12) returns an infinite, while Eq. (10) and Eq. (11) returns $\delta_{pyr} = -\frac{l^3(\Phi+1)}{48EJ}$ and $\delta_{tet} = -\frac{l^3(\Phi+1)}{36EJ}$ respectively. Neglecting Φ, these deflection are respectively 4 times and 3 times less to the case of a fixed-guided beam subject to a unitary prescribed force [186], thus confirming the validity of the present formulation also in this case.

Comparison of the 7700 FEA results for the deflection of the pyramidal cell and correspondent results obtained by Eq. (10) and Eq. (12) are presented in Figure 4.4. FEA and Eq. (10) results are in great accordance for all the investigated combinations of l, ω and d. Small discrepancies between FEA and Eq. (10) results are visible for the highest values of l combined with minimal values of ω. FEA, Eq. (10), and Eq. (12) results overlaps only for the smallest diameter used in the investigation i.e $d = 0.15$ [mm]. Meanwhile, it can be observed that FEA and Eq. (12) general trends tend to diverge as diameter increases. It can be argued that for negligible bending and shear stiffness Eq. (12) is appropriate to describe the stiffness of the pyramidal cell, especially for relatively large inclination angles ω and relatively small struts length l. Comparison of the 7700 FEA results for the deflection of the tetrahedral cell and correspondent results obtained by Eq. (11) and Eq. (12) are presented in Figure 4.5.

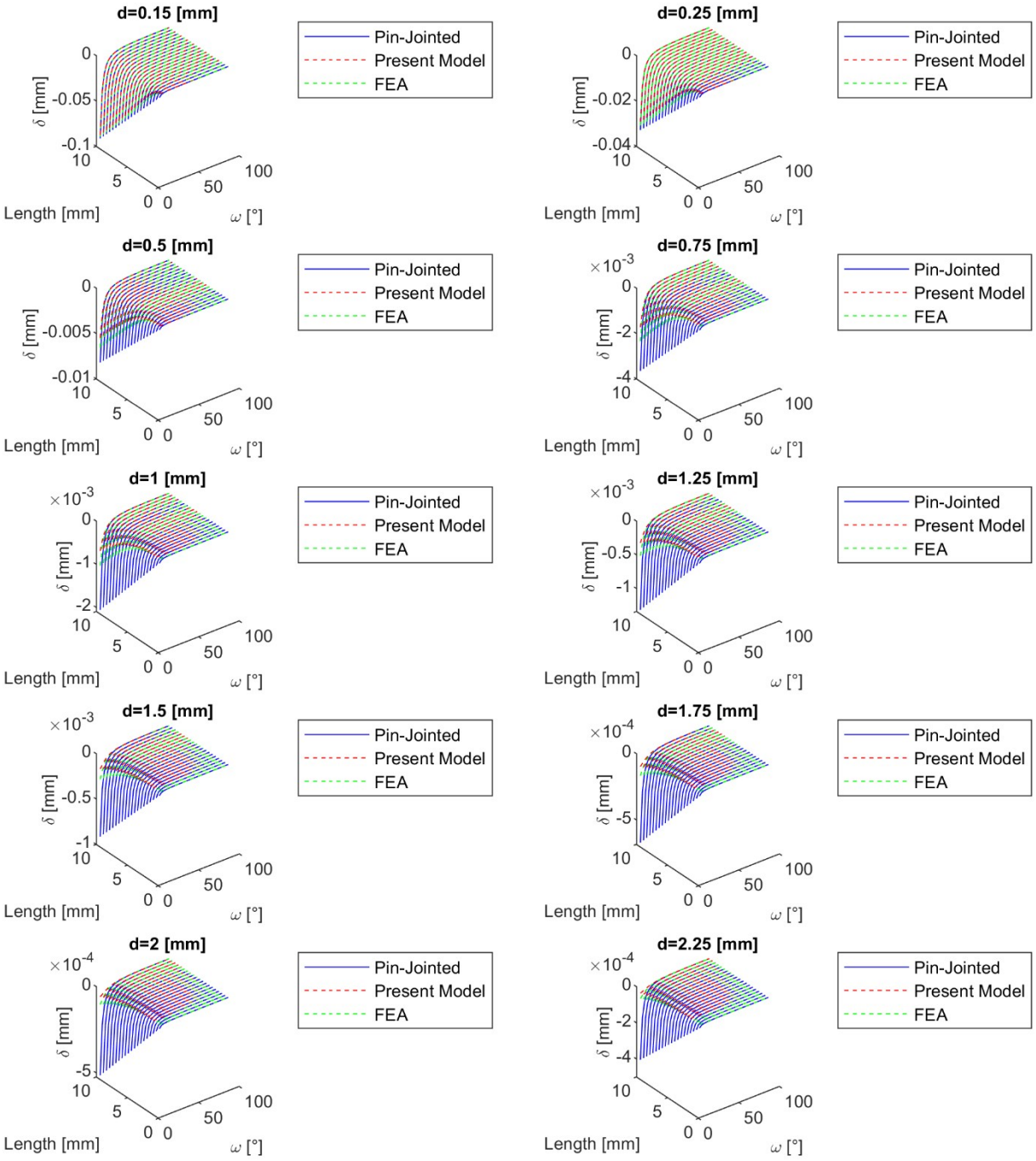

Figure 4.4: Deflection of the pyramidal cell. Comparison between FEA model, Pin-Jointed model, and model presented in this work

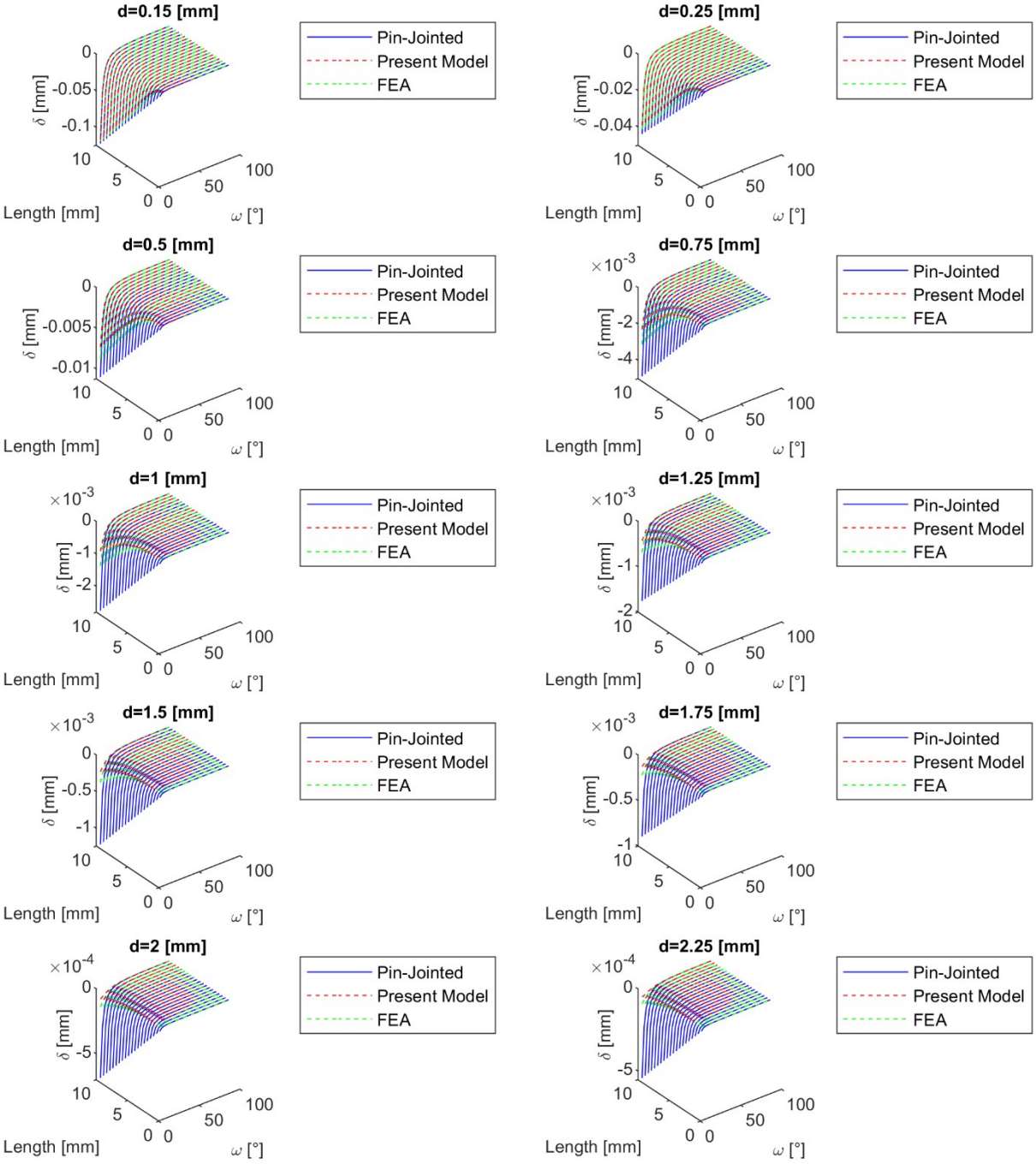

Figure 4.5: Deflection of the tetrahedral cell. Comparison between FEA model, Pin-Jointed model, and model presented in this work

Deflection predicted by all models is greater in the tetrahedral cell compared to the deflection of the pyramidal one. Again results from FEA, Eq. (11), and Eq. (12) overlap only for the smallest diameter used in the investigation i.e $d = 0.15$ [mm]. As observed above, for small inclination angles, formulations including bending and shear such as FEA and Eq. (11) predicts more reduced deflections than the one provided by Eq. (12). Again, the deviation between FEA and the simplified calculation framework obtained by studying the pin-jointed version of the cell increases with increasing strut length and diameter.

It is worth mentioning that according to Maxwell stability criterion, both cells are conventional classified to be "stretch dominated". From the results retrieved in this section, this conventional definition was proven to be ambiguous. Results strengthen the words of Meza and others [164] when they state that "the existing classification of lattice topologies as stretching- or bending-dominated is insufficient and new theories must be developed".

Nodal forces in the element reference system for the pyramidal cell is given in Eq. (13)

$$\begin{Bmatrix} F_{1x} \\ F_{1y} \\ F_{1z} \\ M_{1x} \\ M_{1y} \\ M_{1z} \\ F_{2x} \\ F_{2y} \\ F_{2z} \\ M_{2x} \\ M_{2y} \\ M_{2z} \end{Bmatrix} = \begin{Bmatrix} \dfrac{2Al^2(\Phi+1)\,sin(\omega)}{3\left(cos(2\omega)\left(12I - Al^2(\Phi+1)\right) + Al^2(\Phi+1) + 12I\right)} \\ -\dfrac{8Il\sqrt{cos^2(\omega)}}{\sqrt{l^2}(cos(2\omega)\,(Al^2(\Phi+1) - 12I) - Al^2(\Phi+1) - 12I)} \\ 0 \\ 0 \\ 0 \\ \dfrac{4Il\sqrt{cos^2(\omega)}}{cos(2\omega)\left(12I - Al^2(\Phi+1)\right) + Al^2(\Phi+1) + 12I} \\ -\dfrac{2Al^2(\Phi+1)\,sin(\omega)}{3\left(cos(2\omega)\left(12I - Al^2(\Phi+1)\right) + Al^2(\Phi+1) + 12I\right)} \\ \dfrac{8Il\sqrt{cos^2(\omega)}}{\sqrt{l^2}(cos(2\omega)\,(Al^2(\Phi+1) - 12I) - Al^2(\Phi+1) - 12I)} \\ 0 \\ 0 \\ 0 \\ \dfrac{4Il\sqrt{cos^2(\omega)}}{cos(2\omega)\left(12I - Al^2(\Phi+1)\right) + Al^2(\Phi+1) + 12I} \end{Bmatrix} \quad (13)$$

For the investigated loading condition, all struts exhibit the same nodal reaction in their respective element system for the pyramidal cell due to symmetry. Nodal forces in the element reference system for the tetrahedral cell is reported in Eq (14)

$$\begin{Bmatrix} F_{1x} \\ F_{1y} \\ F_{1z} \\ M_{1x} \\ M_{1y} \\ M_{1z} \\ F_{2x} \\ F_{2y} \\ F_{2z} \\ M_{2x} \\ M_{2y} \\ M_{2z} \end{Bmatrix} == \begin{Bmatrix} \frac{Al^2(\Phi+1)\sin(\omega)}{2\left(\cos(2\omega)\left(12I-Al^2(\Phi+1)\right)+Al^2(\Phi+1)+12I\right)} \\ -\frac{6Il\sqrt{\cos^2(\omega)}}{\sqrt{l^2}\left(\cos(2\omega)\left(Al^2(\Phi+1)-12I\right)-Al^2(\Phi+1)-12I\right)} \\ 0 \\ 0 \\ 0 \\ \frac{3Il\sqrt{\cos^2(\omega)}}{\cos(2\omega)\left(12I-Al^2(\Phi+1)\right)+Al^2(\Phi+1)+12I} \\ -\frac{Al^2(\Phi+1)\sin(\omega)}{2\left(\cos(2\omega)\left(12I-Al^2(\Phi+1)\right)+Al^2(\Phi+1)+12I\right)} \\ \frac{6Il\sqrt{\cos^2(\omega)}}{\sqrt{l^2}\left(\cos(2\omega)\left(Al^2(\Phi+1)-12I\right)-Al^2(\Phi+1)-12I\right)} \\ 0 \\ 0 \\ 0 \\ \frac{3Il\sqrt{\cos^2(\omega)}}{\cos(2\omega)\left(12I-Al^2(\Phi+1)\right)+Al^2(\Phi+1)+12I} \end{Bmatrix} \quad (14)$$

Also in this case, all struts exhibit the same nodal reaction in their respective element system for the pyramidal cell due to symmetry.

4.3.2 Modeling for buckling

Eigenvalue buckling analysis had a high computational cost, and some simplifications in the formulas were requested. The area A was the only maintained unknown parameter related to the cross-section ($I_y = I_z = \frac{A^2}{4\,\pi}$ and $I_p = \frac{A^2}{2\,\pi}$). Under these assumptions, the 4 independent critical loads predicted by the present model for the pyramidal cell are:

$$\begin{aligned} P_{cr1} = {} & (15A^2\csc(\omega)(6A(6AE(E^2-EG+2G^2)+G\csc^2(\omega)(12AE^2+\pi Gl^2(16E \\ & -4G\omega\cos+G))+2E\cos(2\omega)(3A(E-2G)(E-G)+\pi Gl^2(5E \\ & -8G))+2\pi EGl^2(5E-8G))+8\pi^2G^2l^4((2E-G)\cos(2\omega)+2E \\ & +G))/(4(3AE+\pi Gl^2)(45A^2E+\pi l^2\csc^2(\omega)(3A(4E+5G) \\ & +4\pi Gl^2)-12\pi AEl^2-4\pi^2Gl^4)) \end{aligned} \quad (15)$$

$$
\begin{aligned}
P_{cr2} = -((&10A(-G\pi l^2 + (G\pi l^2 + 3A(E-G))\cos^2(\omega) \\
&- 3AE)(-4EG^2\pi^3\cos^2(\omega)(\cos(2\omega) - 3)\sin(\omega)l^6 \\
&- 6AG\pi^2\sin(\omega)((2E-G)((4E-G)\cos^4(\omega) + 4(2E \\
&- 3G)\sin^2(\omega)) - 4(4E^2 + 5GE + 3G^2))l^4 - 9A^2E\pi((8E^2 - 23GE \\
&+ 4G^2)\cos^4(\omega) - 8E^2 - 54G^2 - 89EG + (-8E^2 + 39GE \\
&- 54G^2)\cos(2\omega))\sin(\omega)l^2 + 27A^3E^2((11E - 12G)\cos^4(\omega) \\
&+ 17E + 22G + (22G - 7E)\cos(2\omega))\sin(\omega) + \sqrt{CC}\,))/\,((G\pi l^2 \\
&+ 3AE)(2(G\pi l^2 + 3AE)(-4G\pi^2 l^4 - 12AE\pi l^2 + 45A^2E)\cos^6(\omega) \\
&- 9(-12G^2\pi^3 l^6 + 4AG(5G - 18E)\pi^2 l^4 + A^2(-108E^2 + 190GE \\
&+ 75G^2)\pi l^2 + 390A^3E^2)\cos^4(\omega) + 20(G\pi l^2 + 3AE)(-14G\pi^2 l^4 \\
&+ 3A(3G - 14E)\pi l^2 + 54A^2E)\cos^2(\omega) + 180\pi(G\pi l^3 + 3AEl)^2)))
\end{aligned}
\tag{16}
$$

with

$$
\begin{aligned}
CC = \ (&-(-8EG^2\pi^3 l^6 + 6AG(G-2E)(4E+G)\pi^2 l^4 + 9A^2E(-8E^2 + 13GE \\
&+ 4G^2)\pi l^2 + 27A^3E^2(9E - 8G))^2\cos^{10}(\omega) + (320E^2G^4\pi^6 l^{12} \\
&+ 384AEG^3(10E^2 + 3GE - 3G^2)\pi^5 l^{10} + 36A^2G^2(480E^4 \\
&+ 224GE^3 - 428G^2E^2 + 148G^3E + 25G^4)\pi^4 l^8 \\
&+ 108A^3EG(320E^4 + 96GE^3 - 762G^2E^2 + 127G^3E \\
&+ 190G^4)\pi^3 l^6 + 81A^4E(320E^5 - 384GE^4 - 2667G^2E^3 \\
&+ 192G^3E^2 + 1920G^4E - 600G^5)\pi^2 l^4 - 486A^5E^2(128E^4 \\
&+ 559GE^3 - 214G^2E^2 - 530G^3E + 300G^4)\pi l^2 - 13851A^6E^5(9E \\
&- 8G))\cos^8(\omega) - 8(64E^2G^4\pi^6 l^{12} + 96AEG^3(8E^2 + 11GE \\
&- 4G^2)\pi^5 l^{10} + 36A^2G^2(96E^4 + 282GE^3 - 72G^2E^2 + 4G^3E \\
&+ 21G^4)\pi^4 l^8 + 27A^3EG(256E^4 + 1272GE^3 - 582G^2E^2 \\
&- 1201G^3E + 546G^4)\pi^3 l^6 + 81A^4E(64E^5 + 568GE^4 - 873G^2E^3 \\
&- 1879G^3E^2 + 1334G^4E - 150G^5)\pi^2 l^4 + 243A^5E^2(72E^4 \\
&- 512GE^3 - 591G^2E^2 + 766G^3E - 150G^4)\pi l^2 - 729A^6E^4(61E^2 \\
&- 71GE + 6G^2))\cos^6(\omega) + 4(64E^2G^4\pi^6 l^{12} + 24AEG^3(32E^2 \\
&+ 150GE - 21G^2)\pi^5 l^{10} + 36A^2G^2(96E^4 + 985GE^3 + 508G^2E^2 \\
&- 160G^3E + 36G^4)\pi^4 l^8 + 108A^3EG(64E^4 + 1155GE^3 \\
&+ 1102G^2E^2 - 1740G^3E + 264G^4)\pi^3 l^6 + 81A^4E^2(64E^4 \\
&+ 2220GE^3 + 2157G^2E^2 - 9780G^3E + 2784G^4)\pi^2 l^4 \\
&+ 486A^5E^3(170E^3 + 29GE^2 - 1720G^2E + 738G^3)\pi l^2 \\
&+ 729A^6E^4(109E^2 + 20GE + 4G^2))\cos^4(\omega) - 96AE(G\pi l^2 \\
&+ 3AE)(76EG^3\pi^4 l^8 + 3AG^2(173E^2 + 524GE - 66G^2)\pi^3 l^6 \\
&+ 9A^2EG(118E^2 + 637GE - 528G^2)\pi^2 l^4 + 27A^3E^2(21E^2 \\
&+ 152GE - 268G^2)\pi l^2 + 243A^4E^3(13E - 2G))\cos^2(\omega) \\
&+ 576A^2E^2(G\pi l^2 + 3AE)^2(124G^2\pi^2 l^4 + 99AEG\pi l^2 + 81A^2E^2))
\end{aligned}
\tag{17}
$$

$$
\begin{aligned}
P_{cr3} = -((&10A(-G\pi l^2 + (G\pi l^2 + 3A(E-G))\cos^2(\omega) \\
&- 3AE)(-4EG^2\pi^3\cos^2(\omega)(\cos(2\omega) - 3)\sin(\omega)l^6 \\
&- 6AG\pi^2\sin(\omega)((2E-G)((4E-G)\cos^4(\omega) + 4(2E \\
&- 3G)\sin^2(\omega)) - 4(4E^2 + 5GE + 3G^2))l^4 - 9A^2E\pi((8E^2 - 23GE \\
&+ 4G^2)\cos^4(\omega) - 8E^2 - 54G^2 - 89EG + (-8E^2 + 39GE \\
&- 54G^2)\cos(2\omega))\sin(\omega)l^2 + 27A^3E^2((11E - 12G)\cos^4(\omega) \\
&+ 17E + 22G + (22G - 7E)\cos(2\omega))\sin(\omega) - \sqrt{CC}\,))/((G\pi l^2 \\
&+ 3AE)(2(G\pi l^2 + 3AE)(-4G\pi^2 l^4 - 12AE\pi l^2 + 45A^2E)\cos^6(\omega) \\
&- 9(-12G^2\pi^3 l^6 + 4AG(5G - 18E)\pi^2 l^4 + A^2(-108E^2 + 190GE \\
&+ 75G^2)\pi l^2 + 390A^3E^2)\cos^4(\omega) + 20(G\pi l^2 + 3AE)(-14G\pi^2 l^4 \\
&+ 3A(3G - 14E)\pi l^2 + 54A^2E)\cos^2(\omega) + 180\pi(G\pi l^3 + 3AEl)^2)))
\end{aligned}
\tag{18}
$$

and

$$
P_{cr4} = \frac{20AE\sin(\omega)(3A(E-G) + 3AG\csc^2(\omega) + \pi G l^2)^2}{(6\csc^2(\omega) - 1)(3AE + \pi G l^2)^2} \tag{19}
$$

Due to the formulas' complexity, it is very challenging to determine if any of the four will always return a minimum value for any combination of length, diameter, inclination, or material parameters.

The minimum buckling load will be determined from time to time by analyzing the values of the four P_{cr}. It is worth mentioning that Eq. (16) and Eq. (18) differ only for the sign of the square root of CC given in Eq. (17). Domain of validity of the present formulation is $\left]0, \frac{\pi}{2}\right[$ since for $\omega = 0$ axial load vanish in Eq. (13). For $\omega = \frac{\pi}{2}$ Eq.(19) degenerates in $P_{cr4} = 4AE$ that is less than the critical buckling load provided by Euler's formula (Eq. (1)).

After an extensive analysis, it can be assumed that the model presented herein provides buckling loads generally greater than the one predicted with FEA. It is a classical convergency problem due to the limitation of having used only one beam element to model the struts [63]. A deeper investigation revealed that convergency is archived by refining the strut using two elements. From the point of view of symbolic computation, this would have resulted in a larger eigenvalue problem, with more eigenvalues and consequently more critical loads to analyze.

After extensive investigations, it was observed that differences from FEA and present model results were essentially constant by varying the inclination angle ω for a given length and diameter. Therefore, the minimum critical load was normalized for fixed l and d by dividing its local value by the maximum value assumed by it in the range of variation $\left]0, \frac{\pi}{2}\right[$. This information is of particular interest for optimizing strut inclination to improve cell buckling characteristics.

Normalized results provided by Euler buckling, present formulas, and FEA analysis are reported in Figure 4.6 for the pyramidal cell. It can be observed that conventional formulations based on the pin-jointed assumptions systematically fail to identify the optimum inclination angle to improve pyramidal cell buckling resistance. A good accordance between the results of the formulation presented in this work and FEA is observable. Minor discrepancies exist for small strut slenderness l/d. It can be observed that results overlap for slenderness ratio greater than 5.

The critical buckling loads obtained for the tetrahedral cell are

$$\begin{aligned} P_{cr1} = (45A^2 \sin(\omega)(3A(E-G) + 3AG\csc^2(\omega) + \pi G l^2)(E\csc^2(\omega)(3AE + 4\pi G l^2) \\ - 3AE(E-2G) + 2\pi G l^2(G-2E)))/(2(3AE + \pi G l^2)(45A^2 E \\ + \pi l^2 \csc^2(\omega)(3A(4E+5G) + 4\pi G l^2) - 12\pi AE l^2 - 4\pi^2 G l^4)) \end{aligned} \quad (20)$$

$$
\begin{aligned}
P_{cr2} = -((&15A(-G\pi l^2 + (G\pi l^2 + 3A(E-G))\cos^2(\omega) \\
&- 3AE)(-4EG^2\pi^3\cos^2(\omega)(\cos(2\omega) - 3)\sin(\omega)l^6 - 6AG\pi^2((2E \\
&- G)\cos^2(\omega)((4E-G)\cos^2(\omega) - 8E + 12G) - 52EG)\sin(\omega)l^4 \\
&- 9A^2E\pi((8E^2 - 23GE + 4G^2)\cos^4(\omega) - 2(8E^2 - 39GE \\
&+ 54G^2)\cos^2(\omega) - 128EG)\sin(\omega)l^2 + 27A^3E^2((11E \\
&- 12G)\cos^4(\omega) + (44G - 14E)\cos^2(\omega) + 24E)\sin(\omega) \\
&+ \sqrt{CC}))/(2(G\pi l^2 + 3AE)(2(G\pi l^2 + 3AE)(-4G\pi^2 l^4 - 12AE\pi l^2 \\
&+ 45A^2E)\cos^6(\omega) - 9(-12G^2\pi^3 l^6 + 4AG(5G - 18E)\pi^2 l^4 \\
&+ A^2(-108E^2 + 190GE + 75G^2)\pi l^2 + 390A^3E^2)\cos^4(\omega) \\
&+ 20(G\pi l^2 + 3AE)(-14G\pi^2 l^4 + 3A(3G - 14E)\pi l^2 \\
&+ 54A^2E)\cos^2(\omega) + 180\pi(G\pi l^3 + 3AEl)^2)))
\end{aligned}
\tag{21}
$$

$$
\begin{aligned}
P_{cr3} = -((&15A(-G\pi l^2 + (G\pi l^2 + 3A(E-G))\cos^2(\omega) - 3AE)(-4EG^2\pi^3\cos^2(\omega)(\cos(2\omega) \\
&- 3)\sin(\omega)l^6 - 6AG\pi^2((2E-G)\cos^2(\omega)((4E-G)\cos^2(\omega) - 8E + 12G) \\
&- 52EG)\sin(\omega)l^4 - 9A^2E\pi((8E^2 - 23GE + 4G^2)\cos^4(\omega) - 2(8E^2 - 39GE \\
&+ 54G^2)\cos^2(\omega) - 128EG)\sin(\omega)l^2 + 27A^3E^2((11E - 12G)\cos^4(\omega) + (44G \\
&- 14E)\cos^2(\omega) + 24E)\sin(\omega) - \sqrt{CC}))/(2(G\pi l^2 + 3AE)(2(G\pi l^2 \\
&+ 3AE)(-4G\pi^2 l^4 - 12AE\pi l^2 + 45A^2E)\cos^6(\omega) - 9(-12G^2\pi^3 l^6 + 4AG(5G \\
&- 18E)\pi^2 l^4 + A^2(-108E^2 + 190GE + 75G^2)\pi l^2 + 390A^3E^2)\cos^4(\omega) + 20(G\pi l^2 \\
&+ 3AE)(-14G\pi^2 l^4 + 3A(3G - 14E)\pi l^2 + 54A^2E)\cos^2(\omega) \\
&+ 180\pi(G\pi l^3 + 3AEl)^2)))
\end{aligned}
\tag{22}
$$

and

$$
P_{cr4} = \frac{15AE\sin(\omega)(3A(E-G) + 3AG\csc^2(\omega) + \pi G l^2)^2}{(6\csc^2(\omega) - 1)(3AE + \pi G l^2)^2} \tag{23}
$$

Where CC for Eq. (21) and Eq. (22) is identical to the one already seen in the pyramidal cell and given by Eq. (17). Also for the tetrahedral cell, formulas for P_{cr2} and P_{cr3} differs from the square root of CC. Domain of validity is the same provided for the pyramidal cell due to the same considerations.

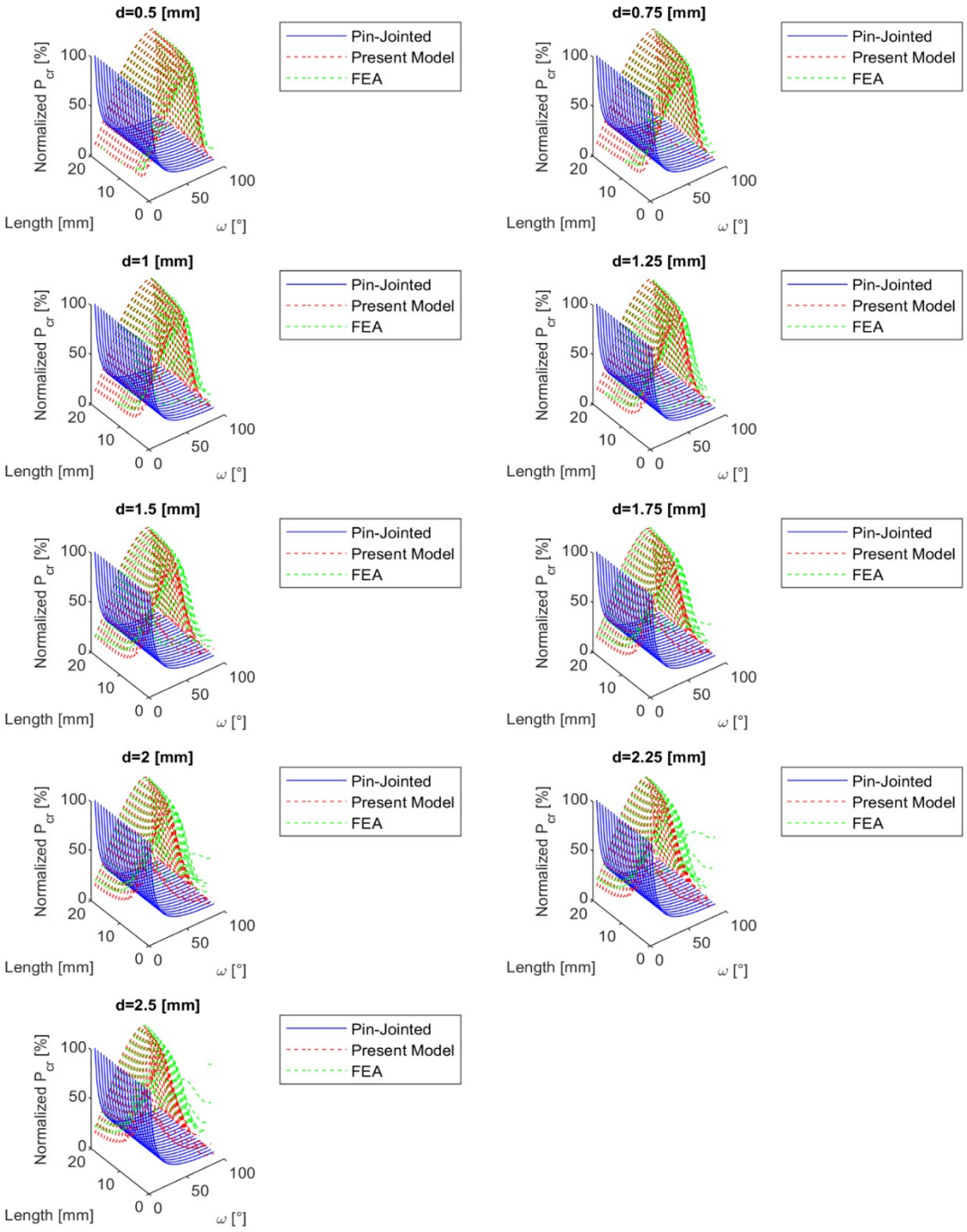

Figure 4.6: Minimum critical buckling load for the pyramidal cell. Comparison of the results for the pin-jointed model, model presented in this work and FEA results.

Also in this case, convergency issues were encountered. For the tetrahedral cell, normalized results provided by Euler buckling, present formulas, and FEA analysis are reported in Figure 4.7. Again, the pin-jointed formulation fails to capture the best inclination angle in any studied configurations. It can be observed that the model is always consistent with FEA results and, again, the best accuracy is obtained for struts having slenderness ratio greater than 5.

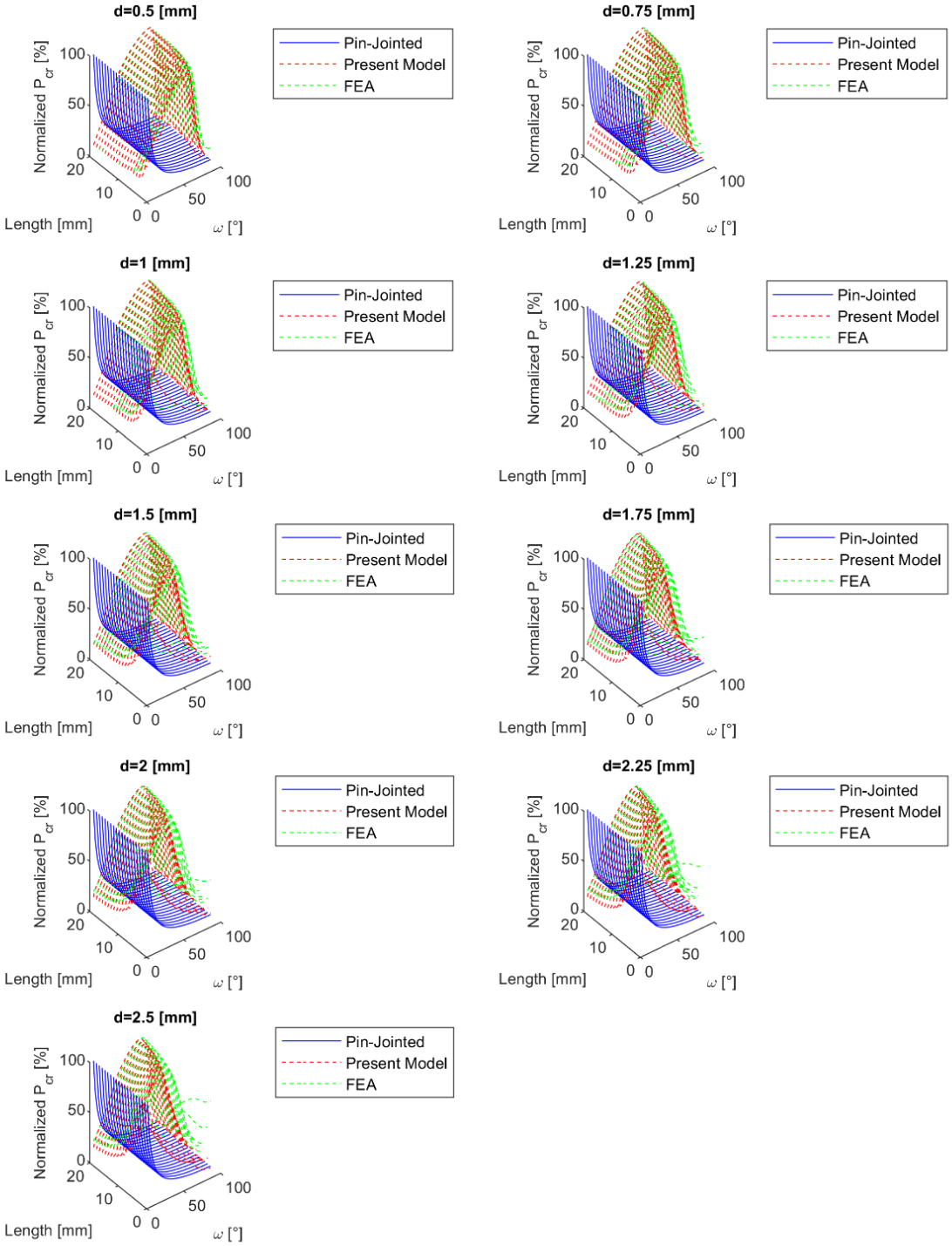

Figure 4.7: Minimum critical buckling load for the tetrahedral cell. Comparison of the results for the pin-jointed model, model presented in this work and FEA results

4.4 CONCLUSIONS

An analytical framework for the optimization of design parameters against stiffness and buckling of lattice material was developed and applied to two different cell architectures, namely a pyramidal cell and a tetrahedral cell. Closed-form solutions for the calculation of the compliance and the critical load of both the pyramidal and the tetrahedral cell were obtained and compared to other analytical models available in the literature. FEA results demonstrated the superiority of the models presented in this work in predicting the mechanical properties of the two mentioned cells over conventional analytical models. It was demonstrated that the existing classification of "strech-dominated" and "bending-dominated" structures is ambiguous and that significant discrepancies can be found between FEA and conventional analytical formulations. The analytical model presented in this paper was always consistent with FEA results.

4.5 APPENDIX A1

Both stiffness and geometrical matrix are reported here for the reader's convenience.

$$
\begin{bmatrix}
0 & 0 & 0 & -\frac{F_{x2}}{L} & 0 & 0 & 0 & 0 & 0 & 0 & 0 & \frac{-\mathrm{E}\,A}{L} & 0 & 0 & 0 & 0 \\
\frac{y1}{L} & \frac{M_{x2}}{L} & \frac{F_{x2}}{10} & 0 & -\frac{6*F_{x2}}{5*L} & 0 & \frac{M_{y2}}{L} & -\frac{M_{x2}}{L} & \frac{F_{x2}}{10} & 0 & 0 & 0 & 0 & 0 & 0 & 0 \\
\frac{z1}{L} & -\frac{F_{x2}}{10} & \frac{M_{x2}}{L} & 0 & 0 & -\frac{6*F_{x2}}{5*L} & \frac{M_{z2}}{L} & -\frac{F_{x2}}{10} & -\frac{M_{x2}}{L} & 0 & \frac{6\ \mathrm{E\ Iz}}{L^2\,(1+\Phi y)} & 0 & \frac{-12\ \mathrm{E\ Iz}}{L^3\,(1+\Phi y)} & 0 & 0 & 0 \\
\frac{*I_p}{*L} & -\frac{2*M_{z1}-M_{z2}}{6} & \frac{2*M_{y1}-M_{y2}}{6} & 0 & -\frac{M_{y1}}{L} & -\frac{M_{z1}}{L} & -\frac{F_{x2}*I_p}{A*L} & -\frac{M_{z1}+M_{z2}}{6} & \frac{M_{y1}+M_{y2}}{6} & \frac{6\ \mathrm{E\ Iy}}{L^2(1+\Phi z)} & 0 & 0 & 0 & \frac{-12\ \mathrm{E\ Iy}}{L^3\,(1+\Phi z)} & 0 & -\frac{6\ \mathrm{E\ Iy}}{L^2\,(1+\Phi z} \\
\frac{z1-M_{z2}}{6} & \frac{2*F_{x2}*L}{15} & 0 & 0 & -\frac{M_{x2}}{L} & \frac{F_{x2}}{10} & -\frac{M_{z1}+M_{z2}}{6} & -\frac{F_{x2}*L}{30} & \frac{M_{x2}}{2} & 0 & 0 & 0 & 0 & 0 & -\frac{G*\mathrm{Ip}}{L} & 0 \\
\frac{1-M_{y2}}{6} & 0 & \frac{2*F_{x2}*L}{15} & 0 & -\frac{F_{x2}}{10} & -\frac{M_{x2}}{L} & \frac{M_{y1}+M_{y2}}{6} & -\frac{M_{x2}}{2} & -\frac{F_{x2}*L}{30} & \frac{4+\Phi z)\mathrm{E\ Iy}}{L(1+\Phi z)} & 0 & 0 & 0 & \frac{6\mathrm{E\ Iy}}{L^2(1+\Phi z)} & 0 & \frac{(2-\Phi z)\mathrm{E\ Iy}}{L\,(1+\Phi z)} \\
0 & 0 & 0 & \frac{F_{x2}}{L} & 0 & 0 & 0 & 0 & 0 & 0 & \frac{(4+\Phi y)\mathrm{EIz}}{L(1+\Phi y)} & 0 & -\frac{6\ \mathrm{E\ Iz}}{L^2\,(1+\Phi y)} & 0 & 0 & 0 \\
\frac{M_{y1}}{L} & -\frac{M_{x2}}{L} & -\frac{F_{x2}}{10} & 0 & \frac{6*F_{x2}}{5*L} & 0 & -\frac{M_{y2}}{L} & \frac{M_{x2}}{L} & -\frac{F_{x2}}{10} & 0 & 0 & \frac{A\,\mathrm{E}}{L} & 0 & 0 & 0 & 0 \\
\frac{M_{z1}}{L} & \frac{F_{x2}}{10} & -\frac{M_{x2}}{L} & 0 & 0 & \frac{6*F_{x2}}{5*L} & -\frac{M_{z2}}{L} & \frac{F_{x2}}{10} & \frac{M_{x2}}{L} & 0 & -\frac{6\ \mathrm{E\ Iz}}{L^2(1+\Phi y)} & 0 & \frac{12\ \mathrm{E\ Iz}}{L^3(1+\Phi y)} & 0 & 0 & 0 \\
\frac{x2*I_p}{A*L} & -\frac{M_{z1}+M_{z2}}{6} & \frac{M_{y1}+M_{y2}}{6} & 0 & -\frac{M_{y2}}{L} & -\frac{M_{z2}}{L} & \frac{F_{x2}*I_p}{A*L} & \frac{M_{z1}-2*M_{z2}}{6} & -\frac{M_{y1}-2*M_{y2}}{6} & 0 & 0 & 0 & 0 & 0 & 0 & 0 \\
\frac{1+M_{z2}}{6} & -\frac{F_{x2*L}}{30} & -\frac{M_{x2}}{L} & 0 & \frac{M_{x2}}{L} & \frac{F_{x2}}{10} & \frac{M_{z1}-2*M_{z2}}{6} & \frac{2*F_{x2*L}}{15} & 0 & \frac{6\mathrm{E\ Iy}}{L^2(1+\Phi z)} & 0 & 0 & 0 & \frac{12\ \mathrm{E\ Iy}}{L^3(1+\Phi z)} & 0 & \frac{6\ \mathrm{E\ Iy}}{L^2\,(1+\Phi z)} \\
\frac{+M_{y2}}{6} & \frac{M_{x2}}{L} & -\frac{F_{x2*L}}{30} & 0 & -\frac{F_{x2}}{10} & \frac{M_{x2}}{L} & -\frac{M_{y1}-2*M_{y2}}{6} & 0 & \frac{2*F_{x2*L}}{15} & 0 & 0 & 0 & 0 & 0 & \frac{G\ \mathrm{Ip}}{L} & 0 \\
 & & & & & & & & & \frac{2-\Phi z)\mathrm{E\ Iy}}{L\,(1+\Phi z)} & 0 & 0 & 0 & \frac{6\ \mathrm{E\ Iy}}{L^2(1+\Phi z)} & 0 & \frac{(4+\Phi z)\mathrm{E\ Iy}}{L(1+\Phi z)} \\
 & & & & & & & & & 0 & \frac{(2-\Phi y)\ \mathrm{E\ Iz}}{L\,(1+\Phi y)} & 0 & -\frac{6\ \mathrm{E\ Iz}}{L^2(1+\Phi y)} & 0 & 0 & 0
\end{bmatrix}
\tag{A2}
$$

SUMMARY

The growing request for lightweight applications, especially for structural parts in in every field of engineering, raises the need to develop innovative technological solutions for multi-material components, in which different functions are deployed in different regions by the best material for a specific need. Recent advances in polymers and novel out-of-autoclave techniques have enabled composite materials to be at the forefront of lightweight technologies in several industries. Conversely, metals are selected for their toughness, shock absorption ability, ease to be precisely cut and finished in view of assembly operations. In this thesis, new methodologies for designing, manufacturing, and monitoring of hybrid metal-composite joints and hybrid composite components were developed.

In Chapter 1, a manufacturing process, a design methodology and experimental validation for hybrid co-cured aluminum/composite tube with rubberlike interface layer under constant bending moment is proposed. Micrograph analysis revealed no defect in the composite and perfect bonding between the viscoelastic and metal and composites layers, thus demonstrating the effectiveness of the optimized metal-composite interface. Moreover, the results of the experimental analysis combined with numerical simulations of the hybrid tubes gave the conclusion that (i) the numerical model well represented the real behavior of the hybrid tube and (ii) the viscoelastic interface layer between aluminum and CFRP tube is effective to reduce fabricational residual stress peaks.

In Chapter 2, a new full-field, cost-effective and reliable methodology for fiber misalignment detection and stiffness prediction for hybrid, long fiber reinforced composite systems is shown.

The fiber misalignment angle was successfully retrieved and benchmarked with one of the most recent and reliable methodologies available in the art state. Comparable were obtained, proving the precision of this method in measuring averaged fiber deviation in laminates. The mechanical test has been performed on composite samples, and for each sample, a FE model was developed by rotating the elemental coordinate system according to fiber orientation estimated utilizing the

new method. The experimental results showed that the improved FE model could predict samples' stiffness with great accuracy. Moreover, a maximum 15% discrepancy between the improved FEA model and the experimental results was demonstrated.

An innovative technological solution for manufacturing high strength and high toughness metal-composite interface, in which a short-fiber composites system infiltrates a 3D printed cellular structure at the metal side is illustrated in Chapter 3. The infiltration process was successful only when, in the bulk charge, the ASMC tows were oriented orthogonally to the lattice interface to ease fiber displacement during molding. The fracture always occurs at the lattice base in both lattices when tested to pullout. The finer lattice failed under a load 2.66 times higher than the rougher one, owing to the higher metal section provided to the pullout test. Moreover, the finer lattice promotes the resin fracture by cohesive failure instead of adhesive one. As a general remark for the investigated technology, the hybrid samples with finer lattice could exhibit a pullout opening pressure force of 10 and 80 times higher than the values obtained on the flat reference. The lattice with big pyramids undergone some buckling under compression molding, evidencing a weak structure for the infiltration process; on the other hand, the lattice with small pyramids perfectly withstood the compression molding loads.

To optimize the design space of lattice materials, a novel closed-form design framework was developed in Chapter 4 and applied to two different cell architectures, namely a pyramidal cell and a tetrahedral cell. Closed-form solutions for calculating the compliance and the critical load of both the pyramidal and the tetrahedral cell were obtained and compared to other analytical models available in the literature. FEA results demonstrated the superiority of the models presented in that chapter in predicting the mechanical properties of the two mentioned cells over conventional analytical models.

The hybrid metal-composite junctions covered in this thesis work have been shown to be sensitive to the process parameters of the composite material. The possibility of fine-tuning digital twin models of the technological process will reduce the time for developing new classes of optimized

hybrid joints. In turn, novel NDT could be developed to monitor the joint's health for structural health monitoring of large multi-material component and parts.

Luca Raimondi 2022

BIBLIOGRAPHY

[1] Staff. Is the BMW 7 Series the future of autocomposites? CompositesWorld 2016. http://www.compositesworld.com/articles/is-the-bmw-7-series-the-future-of-autocomposites.

[2] Godwin EW, Matthews FL. A review of the strength of joints in fibre-reinforced plastics. Part 1. Mechanically fastened joints. Composites 1980;11:155–60. https://doi.org/10.1016/0010-4361(80)90008-7.

[3] Matthews FL, Kilty PF, Godwin EW. A review of the strength of joints in fibre-reinforced plastics. Part 2. Adhesively bonded joints. Composites 1982;13:29–37. https://doi.org/10.1016/0010-4361(82)90168-9.

[4] Adams RD, Cawley P. A review of defect types and nondestructive testing techniques for composites and bonded joints. NDT Int 1988;21:208–22. https://doi.org/10.1016/0308-9126(88)90333-1.

[5] Adams RD. Strength predictions for lap joints, especially with composite adherends. A review. J Adhes 1989;30:219–42. https://doi.org/10.1080/00218468908048207.

[6] Thoppul SD, Finegan J, Gibson RF. Mechanics of mechanically fastened joints in polymer-matrix composite structures - A review. Compos Sci Technol 2009;69:301–29. https://doi.org/10.1016/j.compscitech.2008.09.037.

[7] Hühne C, Zerbst AK, Kuhlmann G, Steenbock C, Rolfes R. Progressive damage analysis of composite bolted joints with liquid shim layers using constant and continuous degradation models. Compos Struct 2010;92:189–200. https://doi.org/10.1016/j.compstruct.2009.05.011.

[8] Maggiore S, Banea MD, Stagnaro P, Luciano G. A review of structural adhesive joints in hybrid joining processes. Polymers (Basel) 2021;13. https://doi.org/10.3390/polym13223961.

[9] Lambiase F, Scipioni SI, Lee CJ, Ko DC, Liu F. A state-of-the-art review on advanced joining processes for metal-composite and metal-polymer hybrid structures. Materials (Basel) 2021;14. https://doi.org/10.3390/ma14081890.

[10] Jahn J, Weber M, Boehner J, Steinhilper R. Assessment Strategies for Composite-metal Joining Technologies-A Review. Procedia CIRP, vol. 50, 2016, p. 689–94. https://doi.org/10.1016/j.procir.2016.05.034.

[11] Campbell FC. Adhesive Bonding and Integrally Cocured Structure. Manuf. Technol. Aerosp. Struct. Mater., 2006, p. 369–418. https://doi.org/10.1016/b978-185617495-4/50008-1.

[12] Woizeschke P, Vollertsen F. Fracture Analysis of Competing Failure Modes of Aluminum-CFRP Joints Using Three-Layer Titanium Laminates as Transition. J Mater Eng Perform 2015;24:3558–72. https://doi.org/10.1007/s11665-015-1638-3.

[13] Silva LFM da, Pirondi A, Öchsner A. Hybrid Adhesive Joints. vol. 6. Berlin, Heidelberg: Springer Berlin Heidelberg; 2011. https://doi.org/10.1007/978-3-642-16623-5.

[14] Chen Y, Yang X, Li M, Wei K, Li S. Mechanical behavior and progressive failure analysis of riveted, bonded and hybrid joints with CFRP-aluminum dissimilar materials. Thin-Walled Struct 2019;139:271–80. https://doi.org/10.1016/j.tws.2019.03.007.

[15] Sadowski T, Golewski P, Zarzeka-Raczkowska E. Damage and failure processes of hybrid joints: Adhesive bonded aluminium plates reinforced by rivets. Comput. Mater. Sci., vol. 50, 2011, p. 1256–62. https://doi.org/10.1016/j.commatsci.2010.06.022.

[16] Buxton AL, Dance BGI. Surfi-Sculpt™ - Revolutionary surface processing with an electron beam. Surf. Eng. - Proc. 4th Int. Surf. Eng. Conf., vol. 2005, 2006, p. 107–10.

[17] Smith F. Comeld - An innovation in composite to metal joining. Weld Cut 2005;4:182–6.

[18] Smith F. COMELD™: An innovation in composite to metal joining. Mater Technol

2005;20:91–6. https://doi.org/10.1080/10667857.2005.11753117.

[19] Zhang H, Wen W, Cui H. Study on the strength prediction model of Comeld composites joints. Compos Part B Eng 2012;43:3310–7. https://doi.org/10.1016/j.compositesb.2012.01.085.

[20] Wang X, Ahn J, Bai Q, Lu W, Lin J. Effect of forming parameters on electron beam Surfi-Sculpt protrusion for Ti-6Al-4V. Mater Des 2015;76:202–6. https://doi.org/10.1016/j.matdes.2015.03.065.

[21] Tu W, Wen PH, Hogg PJ, Guild FJ. Optimisation of the protrusion geometry in Comeld™ joints. Compos Sci Technol 2011;71:868–76. https://doi.org/10.1016/j.compscitech.2011.02.001.

[22] Tu W, Wen P, Guild F. The optimization of Comeld™ joints: A novel technique for bonding composites and metal. WCE 2010 - World Congr. Eng. 2010, vol. 2, 2010, p. 1383–5.

[23] Schierl A. The CMT - Process - A Revolution in welding technology. Weld. World, vol. 49, 2005, p. 38.

[24] Fokens R. Cold Metal Transfer - CMT - A Revolution in Mechanized Root Pass Pipeline Welding. 4th Pipeline Technol Conf 2009:2.

[25] Ucsnik S, Scheerer M, Zaremba S, Pahr DH. Experimental investigation of a novel hybrid metal-composite joining technology. Compos Part A Appl Sci Manuf 2010. https://doi.org/10.1016/j.compositesa.2009.11.003.

[26] Graham DP, Rezai A, Baker D, Smith PA, Watts JF. The development and scalability of a high strength, damage tolerant, hybrid joining scheme for composite-metal structures. Compos Part A Appl Sci Manuf 2014;64:11–24. https://doi.org/10.1016/j.compositesa.2014.04.018.

[27] Ucsnik S, Stelzer S, Sehrschön H, Sieglhuber G. Composite to composite joint with

lightweight metal reinforcement for enhanced damage tolerance. 16th Eur. Conf. Compos. Mater. ECCM 2014, 2014.

[28] Heimbs S, Nogueira AC, Hombergsmeier E, May M, Wolfrum J. Failure behaviour of composite T-joints with novel metallic arrow-pin reinforcement. Compos Struct 2014. https://doi.org/10.1016/j.compstruct.2013.11.022.

[29] Parkes PN, Butler R, Meyer J, de Oliveira A. Static strength of metal-composite joints with penetrative reinforcement. Compos Struct 2014;118:250–6. https://doi.org/10.1016/j.compstruct.2014.07.019.

[30] Parkes PN, Butler R, Almond DP. Fatigue of metal-composite joints with penetrative reinforcement. 54th AIAA/ASME/ASCE/AHS/ASC Struct. Struct. Dyn. Mater. Conf., 2013. https://doi.org/10.2514/6.2013-1879.

[31] Meyer Jonathan, Johns Daniel HA. WO2008110835A1, n.d.

[32] Nguyen ATT, Brandt M, Orifici AC, Feih S. Hierarchical surface features for improved bonding and fracture toughness of metal-metal and metal-composite bonded joints. Int J Adhes Adhes 2016. https://doi.org/10.1016/j.ijadhadh.2015.12.005.

[33] Nguyen ATT, Amarasinghe CK, Brandt M, Feih S, Orifici AC. Loading, support and geometry effects for pin-reinforced hybrid metal-composite joints. Compos Part A Appl Sci Manuf 2017;98:192–206. https://doi.org/10.1016/j.compositesa.2017.03.019.

[34] von H.P.F. Silva MT, Camanho PP, Marques AT, Castro PMST. 3D-reinforcement techniques for co-bonded CFRP/CFRP and CFRP/metal joints: a brief review. Cienc E Tecnol Dos Mater 2017;29:e102–7. https://doi.org/10.1016/j.ctmat.2016.07.011.

[35] Oluleke RJ. METALLURGICAL PERFORMANCE OF HYPER-JOINT PINS IN COMPOSITE TO METAL JOINING. The University of Manchester, 2014.

[36] Jasiūnienė E, Mažeika L, Samaitis V, Cicėnas V, Mattsson D. Ultrasonic non-destructive testing of complex titanium/carbon fibre composite joints. Ultrasonics 2019;95:13–21.

https://doi.org/10.1016/j.ultras.2019.02.009.

[37] Nguyen ATT, Pichitdej N, Brandt M, Feih S, Orifici AC. Failure modelling and characterisation for pin-reinforced metal-composite joints. Compos Struct 2018;188:185–96. https://doi.org/10.1016/j.compstruct.2017.12.043.

[38] Shu JY, Fleck NA. Microbuckle initiation in fibre composites under multiaxial loading. Proc R Soc A Math Phys Eng Sci 1997. https://doi.org/10.1098/rspa.1997.0111.

[39] Jumahat A, Soutis C, Jones FR, Hodzic A. Fracture mechanisms and failure analysis of carbon fibre/toughened epoxy composites subjected to compressive loading. Compos Struct 2010. https://doi.org/10.1016/j.compstruct.2009.08.010.

[40] Li Y, Stier B, Bednarcyk B, Simon JW, Reese S. The effect of fiber misalignment on the homogenized properties of unidirectional fiber reinforced composites. Mech Mater 2016. https://doi.org/10.1016/j.mechmat.2015.10.002.

[41] Jeon SW, Cho YH, Han MG, Chang SH. Design of carbon/epoxy-aluminum hybrid upper arm of the pantograph of high-speed trains using adhesive bonding technique. Compos Struct 2016;152:538–45. https://doi.org/10.1016/j.compstruct.2016.05.079.

[42] Wang J, Gao H, Ding L, Hao Y, Wang B, Sun T, et al. Bond strength between carbon fiber-reinforced plastic tubes and aluminum joints for racing car suspension. Adv Mech Eng 2016;8:1–7. https://doi.org/10.1177/1687814016674627.

[43] Cho DH, Lee DG. Manufacturing of co-cured composite aluminum shafts with compression during co-curing operation to reduce residual thermal stresses. J Compos Mater 1998;32:1221–41. https://doi.org/10.1177/002199839803201205.

[44] Lee DG, Kim HS, Kim JW, Kim JK. Design and manufacture of an automotive hybrid aluminum/composite drive shaft. Compos Struct 2004;63:87–99. https://doi.org/10.1016/S0263-8223(03)00136-3.

[45] Han MG, Cho YH, Jeon SW, Chang SH. Design and fabrication of a metal-composite

hybrid pantograph upper arm by co-cure technique with a friction layer. Compos Struct 2017;174:166–75. https://doi.org/10.1016/j.compstruct.2017.04.041.

[46] Jeon SW, Cho YH, Han MG, Chang SH. Design of carbon/epoxy-aluminum hybrid upper arm of the pantograph of high-speed trains using adhesive bonding technique. Compos Struct 2016;152:538–45. https://doi.org/10.1016/j.compstruct.2016.05.079.

[47] Lee DG, Kim HS, Kim JW, Kim JK. Design and manufacture of an automotive hybrid aluminum/composite drive shaft. Compos Struct 2004;63:87–99. https://doi.org/10.1016/S0263-8223(03)00136-3.

[48] Nikbakt S, Kamarian S, Shakeri M. A review on optimization of composite structures Part I: Laminated composites. Compos Struct 2018;195:158–85. https://doi.org/10.1016/j.compstruct.2018.03.063.

[49] Cesari F, Dal Re V, Minak G, Zucchelli A. Damage and residual strength of laminated carbon-epoxy composite circular plates loaded at the centre. Compos Part A Appl Sci Manuf 2007;38:1163–73. https://doi.org/10.1016/j.compositesa.2006.04.013.

[50] Pervaiz M, Panthapulakkal S, KC B, Sain M, Tjong J. Emerging Trends in Automotive Lightweighting through Novel Composite Materials. Mater Sci Appl 2016. https://doi.org/10.4236/msa.2016.71004.

[51] Akiyama K. Development of preforming process in PCM (Prepreg Compression Molding) technology. 12th Annu Automot Compos Conf Exhib 2012 (ACCE 2012) ; Troy, Michigan, USA, 11 - 13 Sept 2012 2013.

[52] Corbridge DM, Harper LT, De Focatiis DSA, Warrior NA. Compression moulding of composites with hybrid fibre architectures. Compos Part A Appl Sci Manuf 2017. https://doi.org/10.1016/j.compositesa.2016.12.018.

[53] Bücheler D, Henning F. Hybrid Resin Improves Position and Alignment of Continuously Reinforced Prepreg During Compression Co-Molding With Sheet Molding Compound.

17th Eur Conf Compos Mater 2017.

[54] Servais C, Luciani A, Månson JAE. Squeeze flow of concentrated long fibre suspensions: Experiments and model. J Nonnewton Fluid Mech 2002. https://doi.org/10.1016/S0377-0257(02)00018-6.

[55] Pipes RB, Coffin DW, Simacek P, Shuler SF, Okine RK. RHEOLOGICAL BEHAVIOR OF COLLIMATED FIBER THERMOPLASTIC COMPOSITE MATERIALS. Theor. Appl. Rheol., 1992. https://doi.org/10.1016/b978-0-444-89007-8.50390-7.

[56] Mewis J, Metzner AB. The rheological properties of suspensions of fibres in Newtonian fluids subjected to extensional deformations. J Fluid Mech 1974. https://doi.org/10.1017/S0022112074000826.

[57] Sommer DE, Favaloro AJ, Pipes RB. Coupling anisotropic viscosity and fiber orientation in applications to squeeze flow. J Rheol (N Y N Y) 2018. https://doi.org/10.1122/1.5013098.

[58] Yurgartis SW. Measurement of small angle fiber misalignments in continuous fiber composites. Compos Sci Technol 1987. https://doi.org/10.1016/0266-3538(87)90016-9.

[59] KRATMANN K, SUTCLIFFE M, LILLEHEDEN L, PYRZ R, THOMSEN O. A novel image analysis procedure for measuring fibre misalignment in unidirectional fibre composites. Compos Sci Technol 2009. https://doi.org/http://dx.doi.org/10.1016/j.compscitech.2008.10.020.

[60] Wilhelmsson D, Asp LE. A high resolution method for characterisation of fibre misalignment angles in composites. Compos Sci Technol 2018. https://doi.org/10.1016/j.compscitech.2018.07.002.

[61] Nguyen NQ, Mehdikhani M, Straumit I, Gorbatikh L, Lessard L, Lomov S V. Micro-CT measurement of fibre misalignment: Application to carbon/epoxy laminates manufactured in autoclave and by vacuum assisted resin transfer moulding. Compos Part

A Appl Sci Manuf 2018. https://doi.org/10.1016/j.compositesa.2017.10.018.

[62] Mizukami K, Mizutani Y, Todoroki A, Suzuki Y. Detection of in-plane and out-of-plane fiber waviness in unidirectional carbon fiber reinforced composites using eddy current testing. Compos Part B Eng 2016. https://doi.org/10.1016/j.compositesb.2015.09.041.

[63] Cook RR, Malkus DS, Pelsha ME, Witt RJ. Concepts and Applications of Finite Element Analysis. John Wiley Sons Inc 2002.

[64] Griffiths D V. Stiffness matrix of the four?node quadrilateral element in closed form. Int J Numer Methods Eng 1994. https://doi.org/10.1002/nme.1620370609.

[65] Buerzle W, Mazza E. On the deformation behavior of human amnion. J Biomech 2013. https://doi.org/10.1016/j.jbiomech.2013.05.018.

[66] Wilhelmsson D, Gutkin R, Edgren F, Asp LE. An experimental study of fibre waviness and its effects on compressive properties of unidirectional NCF composites. Compos Part A Appl Sci Manuf 2018. https://doi.org/10.1016/j.compositesa.2018.02.013.

[67] PALANCA M, BRUGO TM, CRISTOFOLINI L. USE OF DIGITAL IMAGE CORRELATION TO INVESTIGATE THE BIOMECHANICS OF THE VERTEBRA. J Mech Med Biol 2015. https://doi.org/10.1142/s0219519415400047.

[68] Wilhelmsson D, Asp LE, Gutkin R, Edgren F. Fibre waviness induced bending in compression tests of uniderectional NCF composites. ICCM Int Conf Compos Mater 2017;Volume 201.

[69] Corbridge DM, Harper LT, De Focatiis DSA, Warrior NA. Compression moulding of composites with hybrid fibre architectures. Compos Part A Appl Sci Manuf 2017. https://doi.org/10.1016/j.compositesa.2016.12.018.

[70] Törnqvist L, Vartia P, Vartia YO. How should relative changes be measured? Am Stat 1985. https://doi.org/10.1080/00031305.1985.10479385.

[71] Sánchez-Heres LF, Ringsberg JW, Johnson E. Characterization of Non-Crimp Fabric

Laminates: Loss of Accuracy Due to Strain Measuring Techniques. J Test Eval 2016. https://doi.org/10.1520/jte20150051.

[72] Blass D, Dilger K. CFRP-Part Quality as the Result of Release Agent Application - Demoldability, Contamination Level, Bondability. Procedia CIRP, 2017. https://doi.org/10.1016/j.procir.2017.03.219.

[73] Stewart AL, Poursartip A. Characterization of fibre alignment in as-received aerospace grade unidirectional prepreg. Compos Part A Appl Sci Manuf 2018. https://doi.org/10.1016/j.compositesa.2018.04.018.

[74] Potter K, Langer C, Hodgkiss B, Lamb S. Sources of variability in uncured aerospace grade unidirectional carbon fibre epoxy preimpregnate. Compos Part A Appl Sci Manuf 2007. https://doi.org/10.1016/j.compositesa.2006.07.010.

[75] Varandas LF, Catalanotti G, Melro AR, Tavares RP, Falzon BG. Micromechanical modelling of the longitudinal compressive and tensile failure of unidirectional composites: The effect of fibre misalignment introduced via a stochastic process. Int J Solids Struct 2020. https://doi.org/10.1016/j.ijsolstr.2020.07.022.

[76] Jelf PM, Fleck NA. Compression Failure Mechanisms in Unidirectional Composites. J Compos Mater 1992. https://doi.org/10.1177/002199839202601804.

[77] Tran T, Comas-Cardona S, Abriak NE, Binetruy C. Unified microporomechanical approach for mechanical behavior and permeability of misaligned unidirectional fiber reinforcement. Compos Sci Technol 2010. https://doi.org/10.1016/j.compscitech.2010.04.023.

[78] McNaught AD, Wilkinson A. IUPAC. Compendium of Chemical Terminology, 2nd ed. (the “Gold Book”). 1997. https://doi.org/10.1351/goldbook.

[79] Goede M, Stehlin M, Rafflenbeul L, Kopp G, Beeh E. Super Light Car-lightweight construction thanks to a multi-material design and function integration. Eur Transp Res

Rev 2009. https://doi.org/10.1007/s12544-008-0001-2.

[80] Gardiner G. Is the BMW 7 Series the future of autocomposites? Compos World 2016.

[81] Nehuis F, Kleemann S, Egede P, Vietor T, Herrmann C. Future trends in the development of vehicle bodies regarding lightweight and cost. Lect. Notes Mech. Eng., 2014. https://doi.org/10.1007/978-81-322-1871-5_3.

[82] Banea MD, Rosioara M, Carbas RJC, da Silva LFM. Multi-material adhesive joints for automotive industry. Compos Part B Eng 2018. https://doi.org/10.1016/j.compositesb.2018.06.009.

[83] Owens JFP, Lee-Sullivan P. Stiffness behaviour due to fracture in adhesively bonded composite-to-aluminum joints: I. Theoretical model. Int J Adhes Adhes 2000. https://doi.org/10.1016/S0143-7496(99)00013-5.

[84] Anyfantis KN, Tsouvalis NG. Loading and fracture response of CFRP-to-steel adhesively bonded joints with thick adherents - Part I: Experiments. Compos Struct 2013. https://doi.org/10.1016/j.compstruct.2012.08.060.

[85] Anyfantis KN, Tsouvalis NG. Loading and fracture response of CFRP-to-steel adhesively bonded joints with thick adherents - Part II: Numerical simulation. Compos Struct 2013. https://doi.org/10.1016/j.compstruct.2012.08.056.

[86] Ozel A, Yazici B, Akpinar S, Aydin MD, Temiz Ş. A study on the strength of adhesively bonded joints with different adherends. Compos Part B Eng 2014. https://doi.org/10.1016/j.compositesb.2014.03.001.

[87] Di Franco G, Fratini L, Pasta A. Analysis of the mechanical performance of hybrid (SPR/bonded) single-lap joints between CFRP panels and aluminum blanks. Int J Adhes Adhes 2013. https://doi.org/10.1016/j.ijadhadh.2012.10.008.

[88] Marannano G, Zuccarello B. Numerical experimental analysis of hybrid double lap aluminum-CFRP joints. Compos Part B Eng 2015.

https://doi.org/10.1016/j.compositesb.2014.11.025.

[89] Korta J, Mlyniec A, Uhl T. Experimental and numerical study on the effect of humidity-temperature cycling on structural multi-material adhesive joints. Compos Part B Eng 2015. https://doi.org/10.1016/j.compositesb.2015.05.020.

[90] Povolo M, Raimondi L, Brugo TM, Pagani A, Comand D, Pirazzini L, et al. Design and manufacture of hybrid aluminum/composite co-cured tubes with viscoelastic interface layer. Procedia Struct. Integr., vol. 12, 2018. https://doi.org/10.1016/j.prostr.2018.11.095.

[91] Borsellino C, Di Bella G, Ruisi VF. Adhesive joining of aluminium AA6082: The effects of resin and surface treatment. Int J Adhes Adhes 2009. https://doi.org/10.1016/j.ijadhadh.2008.01.002.

[92] Boutar Y, Naïmi S, Mezlini S, Ali MBS. Effect of surface treatment on the shear strength of aluminium adhesive single-lap joints for automotive applications. Int J Adhes Adhes 2016;67:38–43. https://doi.org/10.1016/j.ijadhadh.2015.12.023.

[93] Islam MS, Tong L, Falzon PJ. Influence of metal surface preparation on its surface profile, contact angle, surface energy and adhesion with glass fibre prepreg. Int J Adhes Adhes 2014. https://doi.org/10.1016/j.ijadhadh.2014.02.006.

[94] da Silva LFM, Carbas RJC, Critchlow GW, Figueiredo MAV, Brown K. Effect of material, geometry, surface treatment and environment on the shear strength of single lap joints. Int J Adhes Adhes 2009. https://doi.org/10.1016/j.ijadhadh.2009.02.012.

[95] Xiong W, Wang X, Dear JP, Blackman BRK. The effect of protrusion density on composite-metal joints with surfi-sculpt reinforcement. Compos Struct 2017. https://doi.org/10.1016/j.compstruct.2017.08.036.

[96] Smith F. Comeld - An innovation in composite to metal joining. Weld Cut 2005.

[97] Tu W, Wen PH, Hogg PJ, Guild FJ. Optimisation of the protrusion geometry in

Comeld™ joints. Compos Sci Technol 2011. https://doi.org/10.1016/j.compscitech.2011.02.001.

[98] Bisagni C, Furfari D, Pacchione M. Experimental investigation of reinforced bonded joints for composite laminates. J Compos Mater 2018. https://doi.org/10.1177/0021998317708021.

[99] Feraboli P, Peitso E, Deleo F, Cleveland T, Stickler PB. Characterization of prepreg-based discontinuous carbon fiber/epoxy systems. J Reinf Plast Compos 2009. https://doi.org/10.1177/0731684408088883.

[100] Selezneva M, Lessard L. Characterization of mechanical properties of randomly oriented strand thermoplastic composites. J Compos Mater 2016. https://doi.org/10.1177/0021998315613129.

[101] Grasso M, Colosimo BM. Process defects and in situ monitoring methods in metal powder bed fusion: A review. Meas Sci Technol 2017. https://doi.org/10.1088/1361-6501/aa5c4f.

[102] Everton SK, Hirsch M, Stavroulakis PI, Leach RK, Clare AT. Review of in-situ process monitoring and in-situ metrology for metal additive manufacturing. Mater Des 2016. https://doi.org/10.1016/j.matdes.2016.01.099.

[103] Grasso M, Laguzza V, Semeraro Q, Colosimo BM. In-Process Monitoring of Selective Laser Melting: Spatial Detection of Defects Via Image Data Analysis. J Manuf Sci Eng Trans ASME 2017. https://doi.org/10.1115/1.4034715.

[104] Martin Schoepf RHH. Method for producing a component assembly and component assembly. DE102015226742.3A, 2017.

[105] SUCH M, WARD C, POTTER K. Aligned Discontinuous Fibre Composites: A Short History. J Multifunct Compos 2014. https://doi.org/10.12783/issn.2168-4286/2/3/4.

[106] Visweswaraiah SB, Selezneva M, Lessard L, Hubert P. Mechanical characterisation and

modelling of randomly oriented strand architecture and their hybrids – A general review. J Reinf Plast Compos 2018. https://doi.org/10.1177/0731684418754360.

[107] Du S, Guo ZS, Zhang B, Wu Z. Cure kinetics of epoxy resin used for advanced composites. Polym Int 2004. https://doi.org/10.1002/pi.1533.

[108] Wang J. PVT Properties of Polymers for Injection Molding. Some Crit. Issues Inject. Molding, 2012. https://doi.org/10.5772/35212.

[109] Wang J, Hopmann C, Schmitz M, Hohlweck T, Wipperfürth J. Modeling of pvT behavior of semi-crystalline polymer based on the two-domain Tait equation of state for injection molding. Mater Des 2019. https://doi.org/10.1016/j.matdes.2019.108149.

[110] Maconachie T, Leary M, Lozanovski B, Zhang X, Qian M, Faruque O, et al. SLM lattice structures: Properties, performance, applications and challenges. Mater Des 2019. https://doi.org/10.1016/j.matdes.2019.108137.

[111] Gibson, Lorna J and Ashby MF. Cellular solids: structure and properties. Cambridge university press; 1999.

[112] Deshpande VS, Fleck NA, Ashby MF. Effective properties of the octet-truss lattice material. J Mech Phys Solids 2001. https://doi.org/10.1016/S0022-5096(01)00010-2.

[113] Liverani E, Toschi S, Ceschini L, Fortunato A. Effect of selective laser melting (SLM) process parameters on microstructure and mechanical properties of 316L austenitic stainless steel. J Mater Process Technol 2017. https://doi.org/10.1016/j.jmatprotec.2017.05.042.

[114] Ashby MF, Bréchet YJM. Designing hybrid materials. Acta Mater 2003. https://doi.org/10.1016/S1359-6454(03)00441-5.

[115] Zhang Q, Lu T. Experimental and simulated compressive properties of work-hardened X-type lattice truss structures. Acta Mech Solida Sin 2012. https://doi.org/10.1016/S0894-9166(12)60012-3.

[116] Queheillalt DT, Carbajal G, Peterson GP, Wadley HNG. A multifunctional heat pipe sandwich panel structure. Int J Heat Mass Transf 2008. https://doi.org/10.1016/j.ijheatmasstransfer.2007.03.051.

[117] Tian J, Kim T, Lu TJ, Hodson HP, Queheillalt DT, Sypeck DJ, et al. The effects of topology upon fluid-flow and heat-transfer within cellular copper structures. Int J Heat Mass Transf 2004. https://doi.org/10.1016/j.ijheatmasstransfer.2004.02.010.

[118] Moeini Sedeh M, Khodadadi JM. Interface behavior and void formation during infiltration of liquids into porous structures. Int J Multiph Flow 2013. https://doi.org/10.1016/j.ijmultiphaseflow.2013.07.002.

[119] Gibson LJ; Ashby MF. Cellular solids: structure and properties. 2nd ed. 1997.

[120] Marsavina L. Fracture mechanics of cellular solids. CISM Int. Cent. Mech. Sci. Courses Lect., vol. 521, 2010, p. 1–46. https://doi.org/10.1007/978-3-7091-0297-8_1.

[121] Heo H, Ju J, Kim DM. Compliant cellular structures: Application to a passive morphing airfoil. Compos Struct 2013;106:560–9. https://doi.org/10.1016/j.compstruct.2013.07.013.

[122] Sairajan KK, Aglietti GS, Mani KM. A review of multifunctional structure technology for aerospace applications. Acta Astronaut 2016;120:30–42. https://doi.org/10.1016/j.actaastro.2015.11.024.

[123] Meola C, Boccardi S, Carlomagno G maria. Composite Materials in the Aeronautical Industry. Infrared Thermogr. Eval. Aerosp. Compos. Mater., 2017, p. 1–24. https://doi.org/10.1016/b978-1-78242-171-9.00001-2.

[124] Blakey-Milner B, Gradl P, Snedden G, Brooks M, Pitot J, Lopez E, et al. Metal additive manufacturing in aerospace: A review. Mater Des 2021;209. https://doi.org/10.1016/j.matdes.2021.110008.

[125] Obaid N, Kortschot MT, Sain M. Lightweight thermoset foams in automotive

applications. Light. Sustain. Mater. Automot. Appl., 2017, p. 401–22. https://doi.org/10.1201/9781315152967.

[126] Bisht A, Patel VK, Gangil B. Future of Metal Foam Materials in Automotive Industry. Energy, Environ. Sustain., 2019, p. 51–63. https://doi.org/10.1007/978-981-15-0434-1_4.

[127] Mozafari H, Khatami S, Molatefi H. Out of plane crushing and local stiffness determination of proposed foam filled sandwich panel for Korean Tilting Train eXpress - Numerical study. Mater Des 2015;66:400–11. https://doi.org/10.1016/j.matdes.2014.07.037.

[128] Su L, Liu H, Yao G, Zhang J. Experimental study on the closed-cell aluminum foam shock absorption layer of a high-speed railway tunnel. Soil Dyn Earthq Eng 2019;119:331–45. https://doi.org/10.1016/j.soildyn.2019.01.012.

[129] Yao S, Xiao X, Xu P, Qu Q, Che Q. The impact performance of honeycomb-filled structures under eccentric loading for subway vehicles. Thin-Walled Struct 2018;123:360–70. https://doi.org/10.1016/j.tws.2017.10.031.

[130] Barrios-Muriel J, Romero-Sánchez F, Alonso-Sánchez FJ, Salgado DR. Advances in orthotic and prosthetic manufacturing: A technology review. Materials (Basel) 2020;13. https://doi.org/10.3390/ma13020295.

[131] Gibson LJ. Modelling the mechanical behavior of cellular materials. Mater Sci Eng A 1989;110:1–36. https://doi.org/10.1016/0921-5093(89)90154-8.

[132] Ashby MF. The properties of foams and lattices. Philos Trans R Soc A Math Phys Eng Sci 2006;364:15–30. https://doi.org/10.1098/rsta.2005.1678.

[133] Benedetti M, du Plessis A, Ritchie RO, Dallago M, Razavi SMJ, Berto F. Architected cellular materials: A review on their mechanical properties towards fatigue-tolerant design and fabrication. Mater Sci Eng R Reports 2021;144:100606.

https://doi.org/10.1016/j.mser.2021.100606.

[134] Schaedler TA, Carter WB. Architected Cellular Materials. Annu Rev Mater Res 2016;46:187–210. https://doi.org/10.1146/annurev-matsci-070115-031624.

[135] Schaedler TA, Jacobsen AJ, Torrents A, Sorensen AE, Lian J, Greer JR, et al. Ultralight metallic microlattices. Science (80-) 2011;334:962–5. https://doi.org/10.1126/science.1211649.

[136] Han SC, Lee JW, Kang K. A New Type of Low Density Material: Shellular. Adv Mater 2015;27:5506–11. https://doi.org/10.1002/adma.201501546.

[137] Overvelde JTB, De Jong TA, Shevchenko Y, Becerra SA, Whitesides GM, Weaver JC, et al. A three-dimensional actuated origami-inspired transformable metamaterial with multiple degrees of freedom. Nat Commun 2016;7. https://doi.org/10.1038/ncomms10929.

[138] Bückmann T, Stenger N, Kadic M, Kaschke J, Frölich A, Kennerknecht T, et al. Tailored 3D mechanical metamaterials made by dip-in direct-laser-writing optical lithography. Adv Mater 2012;24:2710–4. https://doi.org/10.1002/adma.201200584.

[139] Ahsan Khalid S, Khan AM, Shah OR. Effects of the use of Auxectic Structures for structural damping in composite sandwich core panels for wind turbine blades. J Energy Resour Technol 2020:1–23. https://doi.org/10.1115/1.4048522.

[140] Khalid SA, Khan AM, Shah OR. A Numerical Study Into the Use of Auxectic Structures for Structural Damping in Composite Sandwich Core Panels for Wind Turbine Blades. J Energy Resour Technol 2022;144. https://doi.org/10.1115/1.4051303.

[141] Krödel S, Delpero T, Bergamini A, Ermanni P, Kochmann DM. 3D auxetic microlattices with independently controllable acoustic band gaps and quasi-static elastic moduli. Adv Eng Mater 2014;16:357–63. https://doi.org/10.1002/adem.201300264.

[142] Kadic M, Bückmann T, Stenger N, Thiel M, Wegener M. On the practicability of

pentamode mechanical metamaterials. Appl Phys Lett 2012;100. https://doi.org/10.1063/1.4709436.

[143] Bückmann T, Thiel M, Kadic M, Schittny R, Wegener M. An elasto-mechanical unfeelability cloak made of pentamode metamaterials. Nat Commun 2014;5. https://doi.org/10.1038/ncomms5130.

[144] Tancogne-Dejean T, Spierings AB, Mohr D. Additively-manufactured metallic micro-lattice materials for high specific energy absorption under static and dynamic loading. Acta Mater 2016;116:14–28. https://doi.org/10.1016/j.actamat.2016.05.054.

[145] Zheng X, Lee H, Weisgraber TH, Shusteff M, DeOtte J, Duoss EB, et al. Ultralight, ultrastiff mechanical metamaterials. Science (80-) 2014;344:1373–7. https://doi.org/10.1126/science.1252291.

[146] Sypeck DJ, Wadley HNG. Cellular metal truss core sandwich structures. Adv Eng Mater 2002;4:759–64. https://doi.org/10.1002/1527-2648(20021014)4:10<759::AID-ADEM759>3.0.CO;2-A.

[147] Kooistra GW, Wadley HNG. Lattice truss structures from expanded metal sheet. Mater Des 2007;28:507–14. https://doi.org/10.1016/j.matdes.2005.08.013.

[148] Chiras S, Mumm DR, Evans AG, Wicks N, Hutchinson JW, Dharmasena K, et al. The structural performance of near-optimized truss core panels. Int J Solids Struct 2002;39:4093–115. https://doi.org/10.1016/S0020-7683(02)00241-X.

[149] Wang B, Hu JQ, Li YQ, Yao YT, Wang SX, Ma L. Mechanical properties and failure behavior of the sandwich structures with carbon fiber-reinforced X-type lattice truss core. Compos Struct 2018;185:619–33. https://doi.org/10.1016/j.compstruct.2017.11.066.

[150] Wegst UGK, Bai H, Saiz E, Tomsia AP, Ritchie RO. Bioinspired structural materials. Nat Mater 2015;14:23–36. https://doi.org/10.1038/nmat4089.

[151] Tamburrino F, Graziosi S, Bordegoni M. The design process of additively manufactured mesoscale lattice structures: A review. J Comput Inf Sci Eng 2018;18. https://doi.org/10.1115/1.4040131.

[152] du Plessis A, Broeckhoven C, Yadroitsava I, Yadroitsev I, Hands CH, Kunju R, et al. Beautiful and Functional: A Review of Biomimetic Design in Additive Manufacturing. Addit Manuf 2019;27:408–27. https://doi.org/10.1016/j.addma.2019.03.033.

[153] Benedetti M, du Plessis A, Ritchie RO, Dallago M, Razavi SMJ, Berto F. Architected cellular materials: A review on their mechanical properties towards fatigue-tolerant design and fabrication. Mater Sci Eng R Reports 2021;144. https://doi.org/10.1016/j.mser.2021.100606.

[154] Fan J, Zhang L, Wei S, Zhang Z, Choi SK, Song B, et al. A review of additive manufacturing of metamaterials and developing trends. Mater Today 2021;50:303–28. https://doi.org/10.1016/j.mattod.2021.04.019.

[155] Dong G, Tang Y, Zhao YF. A survey of modeling of lattice structures fabricated by additive manufacturing. J Mech Des Trans ASME 2017;139. https://doi.org/10.1115/1.4037305.

[156] Nazir A, Abate KM, Kumar A, Jeng JY. A state-of-the-art review on types, design, optimization, and additive manufacturing of cellular structures. Int J Adv Manuf Technol 2019;104:3489–510. https://doi.org/10.1007/s00170-019-04085-3.

[157] Alomar Z, Concli F. A Review of the Selective Laser Melting Lattice Structures and Their Numerical Models. Adv Eng Mater 2020;22. https://doi.org/10.1002/adem.202000611.

[158] Gibson LJ, Ashby MF. The mechanics cellular materials of three-dimensional cellular materials. Proc R Soc L 1982;A382:43–59.

[159] Deshpande VS, Fleck NA. Collapse of truss core sandwich beams in 3-point bending. Int

J Solids Struct 2001;38:6275–305. https://doi.org/10.1016/S0020-7683(01)00103-2.

[160] Hutchinson RG, Fleck NA. The structural performance of the periodic truss. J Mech Phys Solids 2006;54:756–82. https://doi.org/10.1016/j.jmps.2005.10.008.

[161] Deshpande VS, Ashby MF, Fleck NA. Foam topology: Bending versus stretching dominated architectures. Acta Mater 2001;49:1035–40. https://doi.org/10.1016/S1359-6454(00)00379-7.

[162] Maconachie T, Leary M, Lozanovski B, Zhang X, Qian M, Faruque O, et al. SLM lattice structures: Properties, performance, applications and challenges. Mater Des 2019;183. https://doi.org/10.1016/j.matdes.2019.108137.

[163] Hanks B, Berthel J, Frecker M, Simpson TW. Mechanical properties of additively manufactured metal lattice structures: Data review and design interface. Addit Manuf 2020;35. https://doi.org/10.1016/j.addma.2020.101301.

[164] Meza LR, Phlipot GP, Portela CM, Maggi A, Montemayor LC, Comella A, et al. Reexamining the mechanical property space of three-dimensional lattice architectures. Acta Mater 2017;140:424–32. https://doi.org/10.1016/j.actamat.2017.08.052.

[165] Feng LJ, Wu LZ, Yu GC. An Hourglass truss lattice structure and its mechanical performances. Mater Des 2016;99:581–91. https://doi.org/10.1016/j.matdes.2016.03.100.

[166] Li P, Wang Z, Petrinic N, Siviour CR. Deformation behaviour of stainless steel microlattice structures by selective laser melting. Mater Sci Eng A 2014;614:116–21. https://doi.org/10.1016/j.msea.2014.07.015.

[167] Liu L, Kamm P, García-Moreno F, Banhart J, Pasini D. Elastic and failure response of imperfect three-dimensional metallic lattices: the role of geometric defects induced by Selective Laser Melting. J Mech Phys Solids 2017;107:160–84. https://doi.org/10.1016/j.jmps.2017.07.003.

[168] Feng LJ, Xiong J, Yang LH, Yu GC, Yang W, Wu LZ. Shear and bending performance

of new type enhanced lattice truss structures. Int J Mech Sci 2017;134:589–98. https://doi.org/10.1016/j.ijmecsci.2017.10.045.

[169] Raimondi L, Tomesani L, Donati L, Zucchelli A. Lattice material infiltration for hybrid metal-composite joints: Manufacturing and static strenght. Compos Struct 2021;269:114069. https://doi.org/10.1016/j.compstruct.2021.114069.

[170] Andersen MN, Wang F, Sigmund O. On the competition for ultimately stiff and strong architected materials. Mater Des 2021;198. https://doi.org/10.1016/j.matdes.2020.109356.

[171] Timoshenko SP, Gere JM, Prager W. Theory of Elastic Stability, Second Edition. J Appl Mech 1962;29:220–1. https://doi.org/10.1115/1.3636481.

[172] Totaro G, De Nicola F, Caramuta P. Local buckling modelling of anisogrid lattice structures with hexagonal cells: An experimental verification. Compos Struct 2013;106. https://doi.org/10.1016/j.compstruct.2013.07.031.

[173] Qi G, Ji B, Ma L. Mechanical response of pyramidal lattice truss core sandwich structures by additive manufacturing. Mech Adv Mater Struct 2019;26:1298–306. https://doi.org/10.1080/15376494.2018.1432805.

[174] Gu JZ, Cheng S. Shear effect on buckling of cellular columns subjected to axially compressed load. Thin-Walled Struct 2016;98:416–20. https://doi.org/10.1016/j.tws.2015.10.019.

[175] He Y, Zhou Y, Liu Z, Liew KM. Buckling and pattern transformation of modified periodic lattice structures. Extrem Mech Lett 2018;22. https://doi.org/10.1016/j.eml.2018.05.011.

[176] Nazir A, Jeng JY. Buckling behavior of additively manufactured cellular columns: Experimental and simulation validation. Mater Des 2020;186. https://doi.org/10.1016/j.matdes.2019.108349.

[177] Shitanaka A, Aoki T, Yokozeki T. Comparison of buckling loads of hyperboloidal and cylindrical lattice structures. Compos Struct 2019;207:877–88. https://doi.org/10.1016/j.compstruct.2018.09.052.

[178] Tang H, Li L, Hu Y. Buckling analysis of two-directionally porous beam. Aerosp Sci Technol 2018;78:471–9. https://doi.org/10.1016/j.ast.2018.04.045.

[179] Vigliotti A, Pasini D. Stiffness and strength of tridimensional periodic lattices. Comput Methods Appl Mech Eng 2012;229–232:27–43. https://doi.org/10.1016/j.cma.2012.03.018.

[180] Anderson MS. Buckling of periodic lattice structures. AIAA J 1981;19:782–8. https://doi.org/10.2514/3.51003.

[181] J.S.Przemieniecki. Theory of matrix structural analysis. Dover Publications Inc.; 1968.

[182] Wu Y, Yang L. The effect of unit cell size and topology on tensile failure behavior of 2D lattice structures. Int J Mech Sci 2020;170. https://doi.org/10.1016/j.ijmecsci.2019.105342.

[183] Argyris JH, Hilpert O, Malejannakis GA, Scharpf DW. On the geometrical stiffness of a beam in space-a consistent V.W. approach. Comput Methods Appl Mech Eng 1979;20:105–31. https://doi.org/10.1016/0045-7825(79)90061-6.

[184] McGuire William, Gallagher Richard H. ZRD. Matrix Structural Analisys - 2nd Edition. 2nd ed. Faculty Books; 200AD.

[185] ANSYS. ANSYS Mechanical APDL. © ANSYS, Inc 2011:www.ansys.com.

[186] Roark RJ, Young WC, Plunkett R. Formulas for Stress and Strain. J Appl Mech 1976;43:522–522. https://doi.org/10.1115/1.3423917.